STRUCTURAL FACTORS AFFECTING LITHIUM TRANSPORT IN LITHIUM-EXCESS LAYERED CATHODE MATERIALS

By

CHRISTOPHER R. FELL

A DISSERTATION PRESENTED TO THE GRADUATE SCHOOL
OF THE UNIVERSITY OF FLORIDA IN PARTIAL FULFILLMENT
OF THE REQUIREMENTS FOR THE DEGREE OF
DOCTOR OF PHILOSOPHY

UNIVERSITY OF FLORIDA

2012

This work is dedicated to my wonderful family.

ACKNOWLEDGMENTS

First of all, I would like to thank my thesis advisor Dr. Ying Shirley Meng and co-advisor Dr. Jacob L. Jones for providing me all the opportunities for completing this work. Their knowledge, care, and inspiration for this work pushed me to expand my knowledge and research potential. I would like to express the deepest gratitude to my other committee members: Dr. Mark Orazem, Dr. Juan Nino, and Dr. Amelia Dempere for their time and guidance.

I am lucky to have met many excellent scientists for collaboration while completing my work, where I had many useful and stimulating discussions. The researchers in Dr. Meng's group: Bo Xu, Ming-Che Yang, Dr. Kyler Carroll, Danna Qian, Dae-Hoe Lee, Thomas McGilvray and Michael Verde have helped and inspired me in many ways. The time spent in Dr. Jacob L. Jones' group also led to many helpful and inspirational conversations with Krishna Nittala, Elena Aksel, Dr. Jennifer Forrester, Dr. Abhijit Pramanick, and Anderson D. Prewitt. I express special thanks to Dr. Maria Elena Arroyo-Dompablo from Spain for our collaboration work.

During this work, I had the excellent opportunity to spend time at other facilities as part of my research and education. I express special thanks to the scientists in the SHaRE program at Oak Ridge National Laboratory (ORNL), especially Dr. Miaofang Chi whose generosity in sharing knowledge, time and expertise in TEM research at a critical stage of my research is greatly appreciated. I am glad to have had the opportunity to meet and collaborate with Dr. Gabriel Veith and Dr. Nancy Dudney at ORNL. Their insight and helpful discussions contributed to a significant portion of this work. I would like to thank the Dr. Matthew Suchomel and Dr. Lynn Ribaud at the Advanced Photon Source at Argonne National Laboratory beamline 11-BM for their diligence helping me collect and recollect high resolution XRD patterns. The work by Clarina R. Dela Cruz and Ovidiu Garlea at HB-2A of the High Flux Isotope Reactor at Oak Ridge National Laboratory is appreciated for their help on neutron diffraction data collection and analysis. I also would like to thank Ke An and Lu Cai at BL-7 Vulcan beamline of the Spallation Neutron Source at ORNL for their help on *in situ* neutron diffraction data collection. I would also like to thank the organizers of the 10th National School on Neutron and X-ray Scattering, in which I had a chance to participate.

I would like to acknowledge the Florida Energy Systems Consortium for their financial support.

I am deeply indebted to my parents for their continuous support. Their love has encouraged and uplifted me through the difficult times. Their encouragement, support and guidance have been instrumental throughout my life.

My deepest gratitude goes to my wife, Meredith. Her devotion, motivation and patience helped make this work possible.

TABLE OF CONTENTS

LIST OF TABLES

LIST OF FIGURES

LIST OF ABBREVIATIONS

a-TEM	(Aberration corrected) transmission electron microscopy
a-STEM	(Aberration corrected) scanning transmission electron microscopy
ANL	Argonne National Laboratory
APS	Advanced photon source
CPS	Curved position sensitive detector
DFT	Density functional theory
DMC	Dimethyl carbonate
EC	Ethylene carbonate
EELS	Electron energy loss spectroscopy
EIS	Electrochemical impedance spectroscopy
EV	Electric vehicle
FWHM	Full width at half maximum
GGA	generalized gradient approximation
HAADF	High angle annular dark field
HEV	Hybrid electric vehicle
HPHT(HP/HT)	High pressure high temperature
ICP	Inductively coupled plasma spectroscopy
LiB	Lithium ion rechargeable battery
NMP	N-methyl pyrrolidone
NEB	Nudged Elastic Band
OCV	Open circuit voltage
ORNL	Oak Ridge National Laboratory
P-HEV	Plug-in hybrid electric vehicle
PITT	Potentiostatic intermittent titration technique

PVDF	Poly-vinylidene fluoride
SEM	Scanning electron microscopy
TM	Transition metal
UHV	Ultra high vacuum
VASP	Vienna ab initio simulation package
XRD	X-ray diffraction
XPS	X-ray photoelectron spectroscopy

Abstract of Dissertation Presented to the Graduate School
of the University of Florida in Partial Fulfillment of the
Requirements for the Degree of Doctor of Philosophy

STRUCTURAL FACTORS AFFECTING LITHIUM TRANSPORT IN LITHIUM-EXCESS LAYERED CATHODE MATERIALS

By

Christopher R. Fell

May 2012

Chair: Ying Shirley Meng
Co-chair: Jacob L. Jones
Major: Materials Science and Engineering

Lithium ion batteries have drawn significant attention as the principle energy storage device powering today's mobile electronic equipment. Despite the increased usage, the performance of current lithium ion battery technology falls short of the requirements needed for large format applications such as electric vehicles. The layered lithium-excess oxide compounds $Li[Ni_xLi_{1/3-2x/3}Mn_{2/3-x/3}]O_2$ are of interest as a new generation of cathode materials for high energy density lithium ion batteries. Efforts to achieve a better understanding of the electrochemistry of lithium-excess materials require the connection of crystal structure to electrochemical properties.

In this dissertation, a combination of advanced characterization techniques was used as a tool to understand the intercalation mechanism of the layered lithium-excess transition metal oxide $Li[Ni_xLi_{1/3-2x/3}Mn_{2/3-x/3}]O_2$. The research identified that synthesis influences the structure of the material specifically the surface of the particles. The formation of a hydroxide rich surface film decreases the electrochemical performance. Post synthesis modifications including high pressure and high temperature leads to the formation of a second layered phase in the bulk; however, the treated samples display

good electrochemical properties. This result underlines the flexibility of the structure of $Li[Ni_xLi_{1/3-2x/3}Mn_{2/3-x/3}]O_2$, a feature uncommon to other layered transition metal oxides. Surface characterization of the layered lithium-excess cathodes following electrochemical cycling revealed the formation of a new surface phase 1 to 5 nm thick as well as insight to the complex cation rearrangement process and phase transformation. This part of the research identified that significant changes occurred during electrochemical cycling; however did not identify when the transformations occurred. Investigation using *in situ* techniques during the first electrochemical cycle shows that the structure undergoes irreversible changes in lattice parameters and microstrain. Microstrain analysis shows that the material undergoes large increases in microstrain during the voltage plateau region. During the charging cycle, charge compensation mechanisms such as oxygen removal and cation migration accommodates the microstrain; however during discharge, these compensation mechanisms do not exist; therefore, causing the microstrain to increase. The analysis of structural changes before, during and following electrochemical property testing has led to an increased understanding of the lithium transport mechanisms in the lithium-excess series of materials.

CHAPTER 1
INTRODUCTION

The growth of the lithium ion battery market has been fueled by the ever increasing demand for energy storage. Rechargeable lithium ion batteries are the key components powering today's mobile electronic equipment. The introduction of the non-aqueous rechargeable lithium ion battery in the 1990s marked the beginning of replacing polluting fossil fuels with alternative clean renewable energy sources.[1] A brief description of the fundamentals components of lithium ion batteries is provided in this chapter along with an overview of characterization techniques. This chapter is intended as a background for the concepts developed later in the dissertation.

1.1 Lithium Ion Batteries

In the most basic sense, an electrochemical cell is a device that converts chemical energy into electrical energy. The chemical energy originates through an oxidation-reduction (redox) reaction which supplies electrons that can be used as electrical energy. Electrochemical cells are classified as primary or secondary based on their ability to be recharged. Secondary batteries include nickel-cadmium (Ni-Cd), nickel-metal hydride (Ni-MH) and lithium ion batteries which are able to be reversibly cycled. Lithium ion batteries have a higher gravimetric and volumetric energy density compared to other battery technologies as shown in Figure 1-1.[2]

All battery cells consist of three parts: a positive electrode (cathode), a negative electrode (anode) and an electrolyte. The electrolyte is an organic solvent typically consisting of alkyl carbonates and dissociated $LiPF_6$ salts. These electrolytes have a voltage operating window between 0.8 V and 4.5 V.[3] The electrolyte serves as an ion conductor to provide a medium to transport electroactive Li^+ ions. Therefore the electrolyte must possess high ionic conductivity, high melting points, and maintain stability within the battery operating voltage. During discharge, the negative electrode is oxidized and supplies electrons to the circuit. Li^+ ions are incorporated from the negative electrode into the host structure of the positive electrode while transition metal ions in the material are reduced by accepting electrons from the external circuit to maintain charge balance. In the charge cycle, energy is supplied through an external source and the electroactive lithium ions are transported from a low chemical energy state in the positive electrode to a high chemical energy state in the negative electrode in Figure 1-2. The device is considered a rechargeable battery since the chemical energy can be restored by supplying electric power to reverse the process.

The performance of a battery is related to the intrinsic properties of the materials that comprise the electrodes. Improvements to the following electrode parameters are needed to continue rechargeable battery expansion into advanced technologies include:[2, 4-6]

- High free energy of reaction (High voltage),
- Gravimetric and Volumetric capacity (Ah/g and Ah/cm^3),
- Rate Capability (power density)
- Cycleability (stability)
- Lifetime
- Cost
- Toxicity (safety)

The Department of Energy has set targets through the FreedomCAR mission has established goals for 2015 to establish electric vehicles with a 15-year battery life that maintains 80% capacity with an energy density of 300Wh/L and costs lower than $20/kW.[7]

The performance of a battery material can be measured by the operating voltage in combination with the specific capacity produced upon charge and discharge. The energy of the material is equal to the cell voltage multiplied by the specific capacity giving rise to gravimetric or volumetric energy density (Wh/kg or Wh/L). The cell voltage is determined by the Gibbs free energy of the electrochemical reaction. The electrochemical potential of one component is the sum of the electrical potential and chemical potential.

$$\Phi = \mu_i + z_i F \varepsilon \tag{1-1}$$

where $\mu_i$is the chemical potential of species I, z_i is the effective charge on lithium, F is Faraday's constant (96,500 C/mol) and ε is the electrical potential. The chemical potential of the cathode is calculated as seen in Equation 1-2 where the partial derivative of Gibbs free energy, G_f, with respect to the concentration, x, of intercalated Li is calculated assuming constant temperature, pressure and moles.

$$\mu_{Li}^{cathode} = \left(\frac{\partial G_f}{\partial x}\right)_{T,P,N} \tag{1-2}$$

The relationship between Gibbs free energy and the cell voltage versus Lithium concentration is seen in Figure 1-3 The voltage profile versus concentration x for $Li_{1-x}CoO_2$ is shown in Figure 1-4 which has a similar shape to the theoretical voltage calculation seen in Figure 1-3. If no external current is applied, the cathode and anode should reach equilibrium states and under the equilibrium conditions, the cell voltage is derived from the Nernst equation [8] and seen below:

$$\Delta\varepsilon = -\frac{(\mu_{Li}^{cathode} - \mu_{Li}^{anode})}{zF} \tag{1-3}$$

The cell voltage is equivalent to the Li^+ chemical potential difference in both electrodes. The theoretical capacity of a cell is the amount of charge able to be generated based on the number of Li^+ ions involved in the electrochemical process defined in terms of ampere-hours. It is given by

$$C = \frac{F \times \Delta x}{3600 \times M} \tag{1-4}$$

where Δx is the number of moles of Li^+ that participate in the reversible electrochemical reaction and M is the molecular weight of the electrode compound.

1.2 Positive Electrode Materials In Lithium Ion Batteries

1.2.1 Intercalation Compounds

The positive electrode electrode is a compound that is capable of being reduced during cell discharge and accepts electrons from the external circuit during the electrochemical reaction. The most popular positive electrodes are based on transition metal oxides which form closed packed planes of oxygen ions with transition metal ions occupying octahedral or tetrahedral interstitial sites. The lithium ions can intercalate and deintercalate between the close packed transition metal–oxygen layers without causing significant changes to the host lattice.

A typical layered structure is seen in Figure 1-5A. It consists of closed–packed oxygen arrangement in ABCABC stacking sequence. Table 1-1 shows the Wyckoff positions, the symmetry and the coordinates for a lithium transition metal oxide with the space group $R\bar{3}m$. The lithium and transition metal ions are octahedrally coordinated with oxygen ions forming alternating layers. Lithium diffusion is available in the two dimensional (sheet) plane perpendicular to the layered stacking. The lithium ions are octahedrally coordinated with oxygen, but diffuse to adjacent octahedral sites by hopping through intermediate tetrahedral sites.[9] The diffusion path is seen in Figure 1-6.[10] This structure belongs to the $R\bar{3}m$ space group. If 1/3 of the transition metal ions are substituted for lithium ions in the transition metal layer and the oxygen framework shifts to ABAB stacking, the structure transforms to a monoclinic crystal structure with a C2/m space group as shown in Figure 1-5B. [11, 12] Furthermore a spinel crystal structure can form if 1/4 of the transition metal ions are redistributed in the octahedral sites in adjacent layers where all lithium ions occupy the tetrahedral sites as shown in Figure 1-5C.[13]

The first lithium ion cathode material commercialized is still largely in use is $LiCoO_2$. This layered material can deliver a theoretical capacity of 280 mAh/g with average kinetics, but there is a serious reversibility problem when the majority of Li^+ ions are extracted from Li_xCoO_2 (x<0.5) thus limiting the achievable capacity to 140 mAh/g.[14] Furthermore cobalt based oxides are expensive and result in explosive reactions, limiting their widespread application.

1.2.2 Layered Nickel Manganese Oxides

Due to the high cost of cobalt at $0.044 per gram and the structural stability, researchers are developing new multi-cation layered oxides. Substitutions for cobalt with nickel and manganese have attracted interest as possible alternatives to $LiCoO_2$ because they are lower in cost ($0.019/gram and $0.0068/gram respectively)[15], safer and more structurally resistant to change when lithium is removed from their structure.[16, 17] In multi-cation layered system compounds, each transition metal ion can tune the specific properties of the cell such as the capacity, the structural and thermal stability and the rate capability. The $Li[Li_{1/3-2x/3}Ni_xMn_{2/3-x/3}]O_2$ ($0 \leq x \leq 1/2$) series of compounds were first reported by Lu and Dahn in 2001. [18, 19] This series of materials is called the lithium-excess series of materials. All compositions adopt the $R\bar{3}m$ space group and have a similar structure to $LiCoO_2$. This material family can be viewed as a solid solution between the two end members, Li_2MnO_3 (x=0) and $Li[Ni_{1/2}Mn_{1/2}]O_2$ (x=0.5), though alternatively it can be expressed as a composite $xLi[Li_{1/3}Mn_{2/3}]O_2$●(1-x)$LiNi_{1/2}Mn_{1/2}O_2$. [20] The structure of these compounds differs from conventional layered oxides such as $LiCoO_2$ because additional Li is present in the transition metal (TM) layer inducing cation ordering in the TM layers. [21, 22] The Li^+ ions form an ordered pattern with Mn^{4+} in the transition metal layer, with most Li surrounded by 5 or 6 Mn ions. Figure 1-7 shows the crystal structure of the lithium-excess material. The crystal structure and layered ordering is identical to that in Figure 1-5A; however, the excess lithium orders in the transition metal layer which is shown in Figure 1-7B.

It is confirmed both by X-ray absorption spectroscopy experiments and first-principles calculations that in the as prepared $Li[Li_{1/3-2x/3}Ni_xMn_{2/3-x/3}]O_2$ ($0 \leq x \leq 1/2$) only Ni^{2+} and Mn^{4+} ions are present. [22-24] Due to the similarities of the ionic radii of lithium and nickel and high temperature synthesis of these materials, experimental studies show that interlayer mixing occurs.[25] The nickel is assumed to occupy the lithium site in the lithium layer and equivalent amount of lithium is assumed to occupy the nickel site in the transition metal layer when refined using Rietveld refinement. [19, 26]

During electrochemical cycling, capacity values that are much higher than those expected theoretically from the Ni^{2+}/Ni^{4+} redox reaction are obtained when the lithium-excess cathode material is cycled. The redox capacities from the lithium-excess materials, with compositions $Li[Li_{1/3-2x/3}Ni_xMn_{2/3-x/3}]O_2$ ($1/5 \leq x \leq 1/3$), range between 126 mAh/g to 199 mAh/g. The material can achieve capacities exceeding 300 mAh/g on the first charge and stable discharge capacities exceeding 200 mAh/g for 50 cycles with upwards of 80% efficiency seen in Figure 1-8 [18, 26-28]

This leads to an irreversible capacity loss on the first cycle between 10 and 30% equaling 40-100 mAh/g.[26, 29-31] Much research has been devoted to explain the anomalous electrochemical capacities observed. It is well understood that the capacity up to 4.4 V originates from the Ni^{2+}/Ni^{4+} redox couple. The largest source of debate originates from a voltage plateau region starting from 4.4 V only observed during the first charge cycle. The reaction mechanisms associated with the 4.5 V plateau region have been extensively studied. Dahn *et al*. originally proposed an oxygen loss mechanism to compensate the extra charge capacities observed.[26] This work has been supported by Armstrong *et al*. who observed the evolution of oxygen gas using *in situ* electrochemical mass spectroscopy measurements. [32] Other researchers similarly support this mechanism and have proposed additional structural changes including migration of surface and bulk cations to explain the materials ability to reversibly cycle without structure deterioration. [33, 34] Unfortunately this research did not quantify the amount of oxygen gas produced, so the explanation by oxygen gas evolution may not be the only acting mechanism. In fact, research from Robertson *et al*. and Jiang *et al.* suggests that a portion of the anomalous capacity from the 4.5 V plateau region originates from the electrode/electrolyte reduction generating H^+ insertion into the material and/or initiating complex Li^+, Ni^{4+} and Mn^{4+} ion migration. The structural changes in the bulk are believed to happen mainly during the first charge since the 4.5 V plateau region does not re-appear in the subsequent cycles. Nevertheless, the large first cycle irreversible capacity and low rate capability still remains a major issue in the lithium-excess series of materials.

Much research efforts have been devoted to address these issues. The most promising approach for reducing the irreversible capacity loss and low rate capability involve surface coating of the cathode surface with either oxides or fluorides like $LiNiPO_4$, Al_2O_3, $AlPO_4$ and AlF_3 [35-38] The exact mechanisms for the improvements are still not well understood. Manthiram *et al.* proposed that the reduction in irreversible capacity loss by surface coating was attributed to the retention of part of the oxygen ion vacancies in the lattice upon cycling through the high voltage plateau region on first charge.[37] However, direct observation of these changes as well as the interaction of the coating with the material during electrochemical cycling is not well documented.

These proposed mechanisms and solutions have raised many questions and issues still needed to be addressed, thus hindering the commercial application of these materials.

1.3 Objectives And Overview

As described throughout Chapter 1, the current state of lithium ion batteries needs to be improved to meet the energy demands of high energy and power density applications such as power tools, hybrid electric vehicles, and electric vehicles. Lithium-excess layered transition metal oxides have received large amounts of attention because they can theoretically meet the requirements of high energy and power applications; however, the large first cycle irreversible capacity and inferior rate capability are hindering the commercial application of these materials. Efforts to achieve a better understanding of the electrochemistry of lithium-excess materials involve the connection of crystal structure to electrochemical properties. Understanding the structure and first cycle charge compensation mechanism in these materials will enable modification of the lithium-excess materials system to overcome the obstacles preventing widespread usage.

The goal of this research is to combine advanced characterization techniques such as TEM, XRD, XPS and EELS to identify structural changes leading to a holistic understanding of the lithium transport mechanisms. The specific objectives are:

- Explore synthesis, structure and electrochemical property relations in layered lithium transition metal intercalation oxides.
- Identify the structural interface changes following electrochemical cycling. The characterization techniques link the analysis of the electrolyte, the surface and the bulk of the cathode to gain a complete understanding of the delithiation mechanism.
- Identify when and how fast the changes occur during the first electrochemical cycle using *in situ* techniques. The previous objectives are conducted *ex situ* and identified significant structural changes *after* electrochemical processes.

By obtaining the above information, the analysis of structural changes before, during and following electrochemical property testing will lead to an increased the understanding of the lithium transport mechanisms in the lithium-excess series of materials. The findings from this research will not only help to understand and eventually improve the lithium-excess series of materials, but also can be expanded to other material systems to understand complex intricacies such as surface coatings, lithium diffusion and oxygen loss mechanism, as well as phase transformation induced by ion migration.

Table 1-1 Rhombohedral structure data with space group of $R\bar{3}m$ [39]

Atom	Wyckoff Position	Site Symmetry	Site Coordinates		
Transition Metal	3a	-3m	0	0	0
Li	3b	-3m	0	0	1/2
O	6c	3m	0	0	z

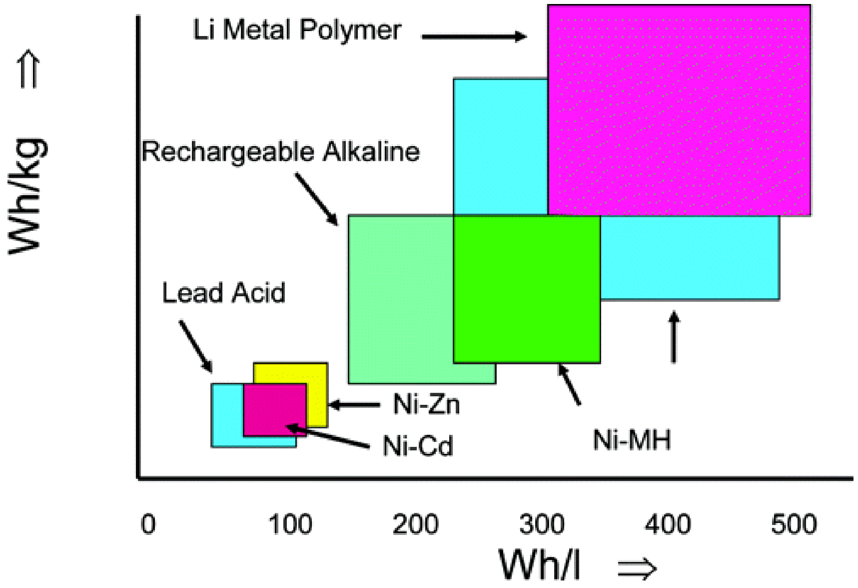

Figure 1-1. Comparison of the different battery technologies in terms of volumetric and gravimetric energy density.[40]

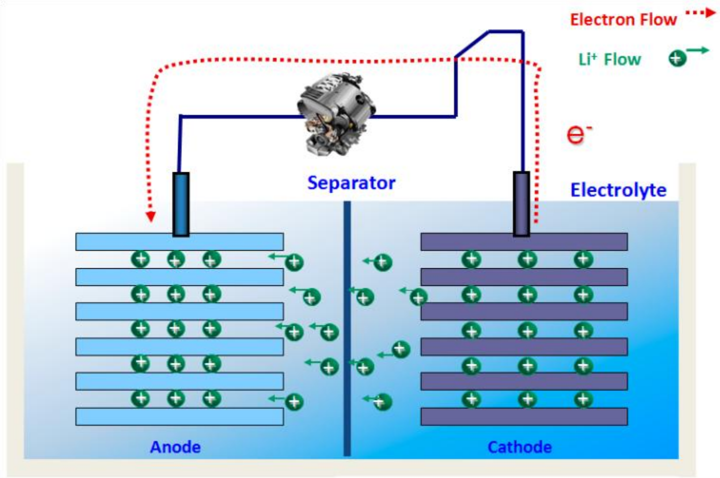

Figure 1-2. Schematic diagram of a lithium ion cell. The cell is composed of a cathode, anode, separator and electrolyte.

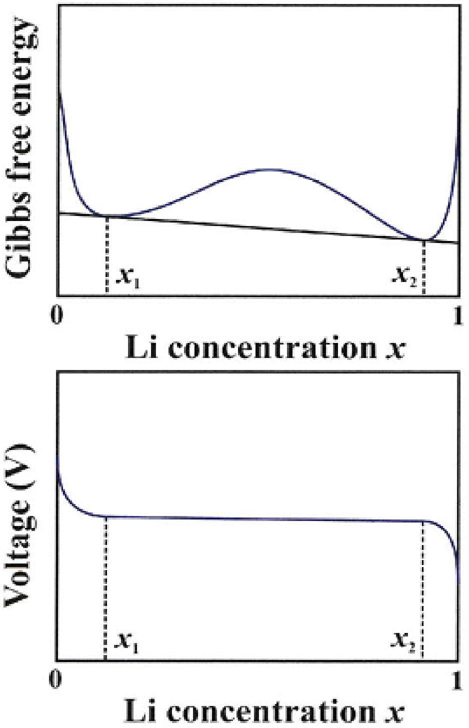

Figure 1-3. Relationship of Gibbs free energy to voltage versus Li concentration x[41]

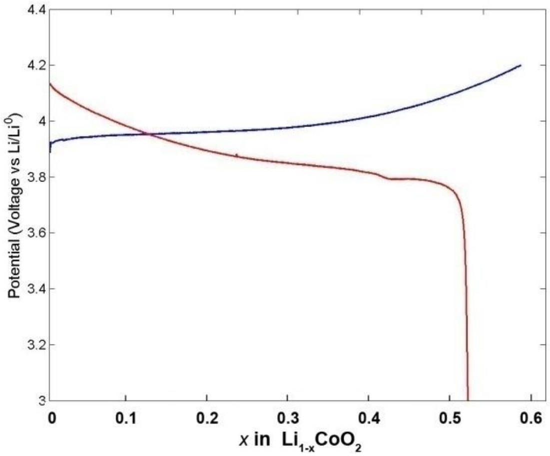

Figure 1-4. Voltage versus composition for $Li_{1-x}CoO_2$ plotted

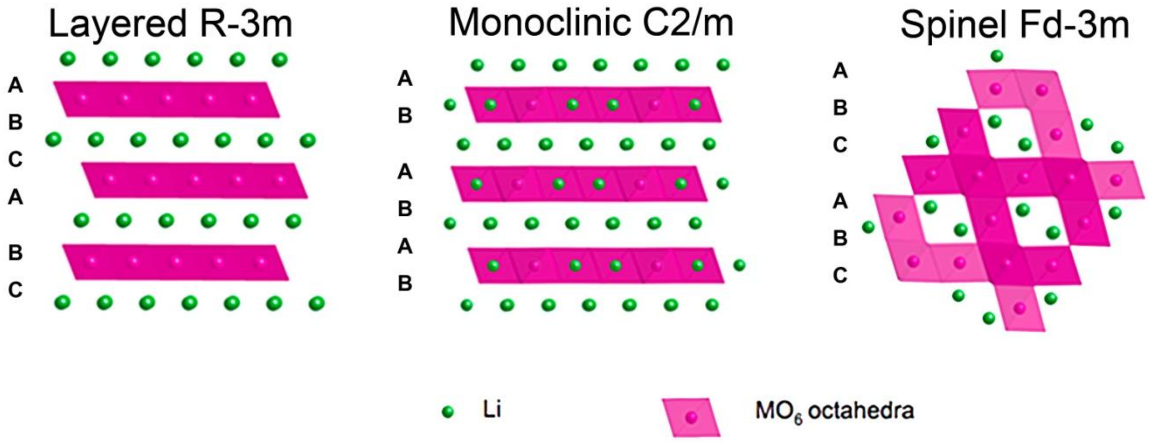

Figure 1-5. Schematic of lithium ion battery cathode structures showing A) the layered structure based on α-$NaFeO_2$ structure. B) the monoclinic *C2/m* structure and C) the spinel $Fd\bar{3}m$ structure. Li^+ ions shown in green and transition metal- oxygen octahedrals in pink.

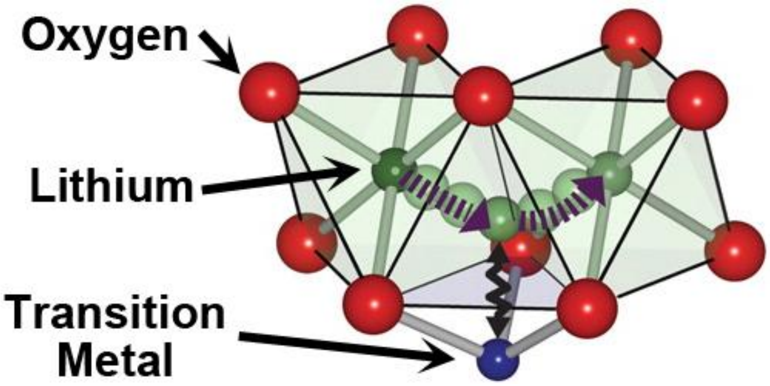

Figure 1-6. Lithium diffusion path from octahedral site to another by passing through a tetrahedral site[10]

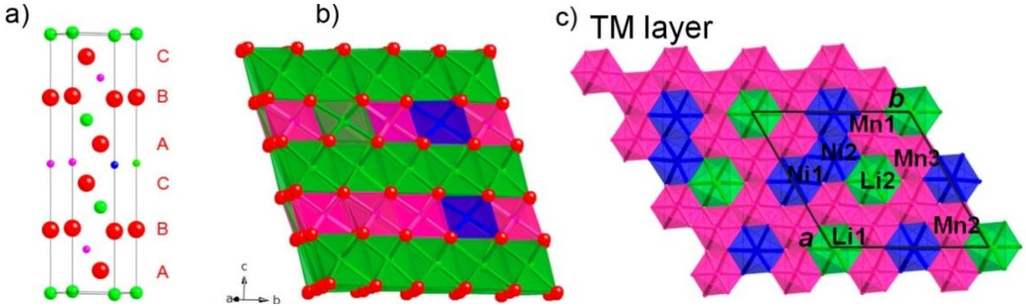

Figure 1-7. Crystal structure of the lithium excess layered oxide under investigation showing A) the oxygen stacking, B) the layered ordering and C) the ordering in the TM layer. Color code: Li green, Mn pink, Ni blue and O red.

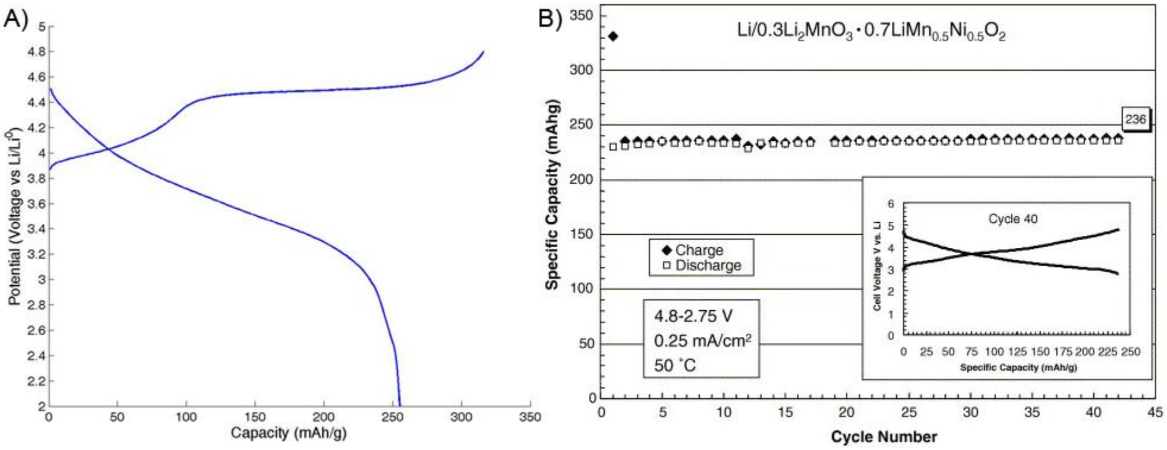

Figure 1-8. Electrochemical data for $Li[Li_{1/5}Ni_{1/5}Mn_{3/5}]O_2$ showing A) the first electrochemical cycle showing potential versus specific capacity (mAh/g) and B) specific capacity versus cycle with an inset showing the voltage profile of the 40th cycle.[28]

CHAPTER 2
CHARACTERIZATION AND SYNTHESIS

Analytical characterization techniques are used to probe the structure-property relationships, which are critical for future advancements in materials science, chemistry, physics and natural sciences. Understanding the arrangement of atoms within a crystal structure provides insight into the understanding of the synthesis, microstructure and properties of materials. The application of analytical characterization techniques to analyze crystal structures is a new, yet vastly expanding aspect of scientific research. The commonly utilized sources of radiation these experiments include X-rays, neutrons and electrons. Diffraction is one of the most powerful analytical tools used to characterize the structure of a crystalline material and is a primary focus of this work. The focus of this chapter is to provide an introduction to the theory behind the diffraction technique and explain the practical applications for analytical techniques that use X-rays, neutrons and electrons to characterize materials. The advantages and limitations of each technique will be explained to illustrate how individual techniques should not be used in isolation to fully explain crystal structures. In this work, we will explain how each technique is applied in combination to characterize the atomic arrangement within the lithium nickel manganese oxide materials. A thorough explanation of the relationship between the crystal structure and the electrochemical properties is essential to optimize the materials’ performance.

2.1 Theory Of Diffraction

2.1.1 Reciprocal Space

In physics, the scattering amplitudes can be expressed by the Fourier transform of the spatial function of the real original lattice that gives rise to what is known as the reciprocal lattice. In crystallography, the reciprocal lattice of a Bravais lattice is the set of all vectors **K** such that

$$e^{i\boldsymbol{K}\cdot\boldsymbol{R}} = 1 \tag{2-1}$$

for all lattice point position vectors **R**. For a three dimensional lattice defined by its primitive vectors **a, b, c**, the reciprocal lattice can be determined by generating its three reciprocal primitive vectors through the formulas:

$$\boldsymbol{a}^* = \frac{\boldsymbol{b}\times\boldsymbol{c}}{\boldsymbol{a}\cdot(\boldsymbol{b}\times\boldsymbol{c})}, \quad \boldsymbol{b}^* = \frac{\boldsymbol{a}\times\boldsymbol{c}}{\boldsymbol{b}\cdot(\boldsymbol{a}\times\boldsymbol{c})}, \quad \boldsymbol{c}^* = \frac{\boldsymbol{a}\times\boldsymbol{b}}{\boldsymbol{c}\cdot(\boldsymbol{a}\times\boldsymbol{b})} \tag{2-2}$$

In the case of orthogonal lattices, **a*** = 1/a, **b*** = 1/b**,** and **c*** = 1/c. The lattices of individual crystallites are oriented randomly and points are found using the position vector in reciprocal space given by:

$$\boldsymbol{d}^* = h\boldsymbol{a}^* + k\boldsymbol{b}^* + l\boldsymbol{c}^* \tag{2-3}$$

where **a*, b*,** and **c*** are vectors defining the reciprocal unit-cell and *h, k,* and *l* are the Miller indices. These are proportional to the to the directional cosines of the planes yielding:

$$\boldsymbol{d}^* = 2\lambda^{-1}\sin\theta \tag{2-4}$$

Figure 2-1 depicts the relationship between the direct lattice and the reciprocal lattice using general oblique two dimensional lattice with basis vectors **a** and **b**.

2.1.2 Bragg's Law And The Laue Condition

Bragg diffraction occurs when radiation waves incident upon a crystalline sample are scattered by the atoms in the system. The scattered radiation wave undergoes constructive interference in accordance with Bragg's law:

$$n\lambda = 2d\sin\theta \tag{2-5}$$

where *n* is the order of reflection, λ is the wavelength of the incident radiation, *d* is the spacing of particular set of lattice planes and θ is the scattering angle between the incident radiation and the lattice planes as shown in Figure 2-2.

The incident radiation denoted by 1 and 2 in Figure 2-2 and the diffracted radiation is denoted by 1' and 2'. When the wavelengths of the scattered waves interfere constructively, intense wave reflections are produced. Diffraction is a wave interference phenomenom Max Von Laue proposed an alternative theorem to the Bragg law for diffraction that does not require the assumptions that reflection is specular and involves parallel planes. The result is valid for any scattered ray. He proposed that a pair of coherent wave vector $\overrightarrow{k_i}$ are absorbed by atoms in a crystal and are re-emmitted as an outgoing wave vector $\overrightarrow{k_d}$ with elastic scattering as seen in Figure 2-3.

The magnitude of the incident radiation vector $\overrightarrow{k_i}$ is equal to

$$|\overrightarrow{k_i}| = 2\pi/\lambda \tag{2-6}$$

where λ is the wavelength. The wave transfer vector described as $\vec{q}$ is equal to the difference of the incident vector and the diffracted vector given by

$$\vec{q} = \overrightarrow{k_f} - \overrightarrow{k_i} = \frac{2\pi}{d} = \boldsymbol{d}^* \tag{2-7}$$

For a general scattering experiment the magnitude of $\vec{q}$ is given by

$$|\vec{q}| = 2|\vec{k}|\sin\theta \tag{2-8}$$

because the scattering event is elastic the incident and scattered wave vectors are equivalent to $|\overrightarrow{k_i}|$ which can be substituted into equation to give Bragg's law (2-4)

The Ewald sphere is a geometric construct that demonstrates the Laue condition for diffraction. [42] The Ewald sphere can be constructed by imagining a crystal sitting at the center of a sphere. The incident wave vector $\mathbf{k_i}$ is placed at a point on the reciprocal lattice (000). The elastically scattered wave vector $\mathbf{k_d}$ is shown intercepting a reciprocal lattice point in Figure 2-4. The radius of the Ewald Sphere is equivalent to the length of $\mathbf{k}$ since in elastic scattering the length of the incident wave $\mathbf{k_i}$ equals that of the scattered wave $\mathbf{k_d}$. The length of $\mathbf{k}$ is on the order of 1/λ. If the scattered wave $\mathbf{k_d}$ touches a reciprocal lattice point, the Laue diffraction condition occurs.

2.2 Sources Of Radiation

2.2.1 X-Ray

X-rays are used as an analytical technique to explain crystal structure, chemical composition and physical properties of materials. X-rays are generated when energetic electrons lose energy. The two major sources that create X-rays include synchrotron radiation and cathode ray tubes. Cathode ray tubes typically use a biased filament to generate electrons which are thermionically emitted into a metallic anode. The characteristic wavelengths of these metallic anodes range from 2.28 Å for chromium to 0.71 Å for molybdenum. The most common used anode is copper with a characteristic wavelength of 1.54 Å. Synchrotron radiation sources consist of a large cyclic particle accelerator with magnetic fields guide electrons and electric fields accelerate the electrons that are synchronized with the travelling particle beam. Beamlines originate at bending magnets and insertion devices which create the X-rays by shifting the energy or path of the electrons. The brilliance of a synchrotron source is about 10 orders of magnitude greater than laboratory X-ray diffractometers. Furthermore, synchrotron radiation uses photon energies that are two orders of magnitude greater than laboratory sources. The higher photon energies produce increased resolution as well as larger material penetration depth leading to increased structural detail. Techniques using X-ray scattering use both elastic and inelastic scattering of the X-ray waves to characterize the crystallographic and electronic structure.

2.2.1.1 Elastic scattering – diffraction

As previously described, X-ray diffraction is based on the elastic scattering of X-rays from the electron clouds of the individual atoms in the material. X-rays are excellent for analyzing crystals because the wavelengths range between 0.1 Å – 100 Å which is on the order of the spacing d between planes in a crystalline material. X-ray diffraction contracts the three-dimensional crystal structure into a one-dimensional diffraction pattern as seen in Figure 2-5.

This dimensional reduction loses the 3-dimensional location of each reciprocal lattice point causing the loss of structural information including preferred orientation and texturing. Furthermore, the number of overlapping reflections increases as $\boldsymbol{d^*}$ increases and intrinsic line broadening from structural imperfections resulting in further problems for structural identification. These examples indicate why x-ray powder diffraction alone is unable to identify all structural information from a material. Additional limitations to X-ray diffraction include characterization of light elements, hydrogen through oxygen. The low electron density of these elements has weak interaction with the incident x-rays leading to difficulty directly identifying the atomic positions. However X-ray diffraction is still a powerful and useful technique based on the simplicity of sample preparation, the ease or time of measurements and the ability of *in situ* structure determination. The high flux of X-rays enables rapid collection times that can capture chemical and physical phenomena on a short time-scale including reaction processes, microstructure changes and phase transformations. [43]

X-ray diffraction is widely used to characterize lithium ion battery component bulk structures. Researchers have used it to identify phase transformations, [21, 44, 45] imperfections in the lattice [46, 47] as well as the effects of dopant materials into the bulk structure. [48, 49] The major disadvantage of x-ray diffraction is that the technique is limited to bulk structure characterization. Significant changes in battery materials occur at the surface due to the interaction with the electrolyte in addition to the bulk during electrochemical cycling. Therefore, x-ray diffraction needs to be linked with surface characterization techniques to develop a holistic understanding of the delithiation mechanisms during electrochemical cycling.

2.2.1.2 Inelastic scattering – photoelectric effect

When photons interact with the atomic electrons the photoelectric process is a direct signature of the interaction with the atom. When the X-ray photons irradiate a material, the kinetic energy and number of electrons that escape the top 1 to 10 nm of the material are analyzed. The process of photoemission is shown schematically in Figure 2-6.

The kinetic energy of the spectrum reveals insight into the elemental composition, empirical formula, chemical state and electronic state of the atoms within the material. The X-ray photon has a known energy of hv which interacts with the material releasing electrons with known electron binding energies (E_B) and experimentally measured electron kinetic energies (E_K). The spectrometer has a specific work function (Φ_{spec}) Equation 2-9 shows the relationship between the parameters involved in the X-ray photoelectron spectroscopy (XPS) experiment:

$$E_B = hv - E_K - \Phi_{\text{spec}} \tag{2-9}$$

Since all elements on the right hand side it is easy to calculate the binding energy of electron. All electrons with binding energies less than the photon energy contribute to characteristic peaks in an XPS spectra as seen in for nickel in Figure 2-7. [50-52]

A distinct advantage of XPS as an analytical technique includes the ability to identify chemical states of atoms. For example the spectra of Ni^0 differs from Ni^{2+} or Ni^{4+} and can reveal insights into surface changes of a material. This information is available as a result of the spatial redistribution of valence electron charges of an atom creating a different potential as seen by a core electron which are measured in an XPS spectra. However, this information is obtained at the expense of spatial resolution. Furthermore, XPS is limited to surface analysis 1 to 10 nm governed by the Beer-Lambert law.

XPS is a powerful characterization tool used to probe and analyze the surface structure of lithium ion battery components. X-ray photoelectron spectra show chemical composition and chemical states of atoms can be used to identify the reversibility of redox reactions[53, 54], formation of surface films. [55-57] However, this technique is limited by the penetration depth to the surface; therefore, must be linked with a technique that can probe bulk changes.

2.2.2 Neutron

The use of neutrons to characterize a material is technique developed in the 1940's by Shull and Brockhouse. Neutrons are uncharged particles that are released from the atomic nucleus through two common mechanisms. The first being nuclear decay from a nuclear reactor and the second is the interaction of a high energy pulsed proton beam with a heavy metal target producing bunches of neutrons called "spallation" reactions. The latter source produces neutron fluxes several orders of magnitude larger than a nuclear reactor source giving increased intensities making *in* *situ* diffraction studies with similar capabilities to x-rays. The neutrons interact with a sample both elastically in the form of diffraction and inelastically to form phonons and magnons. The focus of this work involves the elastic scattering of neutrons. Regardless of the interaction with the material, neutrons have similar wave-like behavior to x-rays with characteristic wavelengths on the order of 1 Å making them suitable for diffraction experiments governed by Bragg's law. The major advantage of neutrons in diffraction experiments is that the scattering cross-section of elements is not dependent on the electron density of the element enabling identification of the positions of the low atomic weight elements between hydrogen and oxygen. Furthermore, the scattering cross section among adjacent elements on the periodic table usually provides sufficient contrast leading to specific elemental identification such as that of Mn (-3.73 fm), Co (2.49 fm) and Ni (10.3 fm) which are commonly used in lithium ion batteries.

2.2.3 Electron

The electron is a negatively charged particle with low mass. When electrons pass close to atoms, they are easily deflected by other electrons or the positive nucleus of an atom. An electron beam can be created using thermionic or field-emission sources. The thermionic sources use either a tungsten filament or lanthanum hexaboride crystal. Cold field emission guns provide high enormous current density and brightness. The beam diameters are small in diameter and are highly monochromatic. Field emission guns require ultra high vacuum systems in order to suppress the damage by ions generated at the tungsten tip. Recent advances in transmission electron microscopy (TEM) have improved the resolution of the electron beam to measure the nanoscale properties of a material down to 0.5 Å. However, the resolution of the microscope is not limited by the electron wavelength (λ= 3.7 – 2.0 pm) but by the electron lenses causing spherical and chromatic aberrations. The spherical aberration is the largest defect limiting the resolution of most TEMs. It causes the lens to inhomogeneously guide the electrons from a single focal point to a range of focal points producing blurry images. Chromatic aberrations increase the electron energy divergence from a monochromatic source.

2.2.3.1 Elastic scattering

When electrons are elastically scattered there are two primary interactions. One interaction is the electrostatic interactions with the atomic nucleus causing electron scattering. Electrons also have a wave-like interaction with the electron cloud that gives rise to diffraction effects or an angular distribution. Electron images and diffraction patterns are different two-dimensional electron-intensity distributions formed by possible scattering from the same object. This makes the TEM a powerful instrument for both characterizing a materials crystal structure as well as detailing information about the chemical composition of a sample. However, the requirements of specimen thickness, lack of depth sensitivity and lack of sampling area limits the ability of TEM as a single tool for complete material characterization.

The TEM has led to important breakthrough in analyzing both the surface and bulk of lithium ion battery components. With electron diffraction, the presence of long-range ordering can be identified that is nearly undetectable with X-ray diffraction and neutron diffraction.[47, 58] Electron microscopy also is valuable for identify particle morphology and detailed crystallographic data.[59-61]

2.2.3.2 Inelastic scattering

Electrons are an ionizing radiation which is capable of removing tightly bound inner-shell electrons from the attractive field of the nucleus. The ionizing radiation produces a wide range of secondary signals from the specimen. One techniques used to analyze the energy distribution of inelastically scattered electrons from the specimen is electron energy-loss spectrometry (EELS) The technique reveals detail about the nature of the atom, the bonding, the nearest neighbor interactions and the dielectric response. Figure 2-8 shows an EELS spectrum which is customarily divided into two parts, the low-loss and high-energy loss regions.[62]

The low-loss spectrum refers to the transmitted electrons that can undergo three types of interactions. These interactions include no changes in energy or momentum, changes in momentum but no energy loss or have undergone small energy losses from the incident electron to the outer shell electron. This spectrum is dominated by interband transitions and excitations of valence electrons generating plasmons, which gives rise to prominent peaks in the range of 5 eV to 35 eV. From this region, electronic transitions and chemical fingerprinting can be quantitatively and qualitatively extracted. Interpretation of this region is complicated to the overlap of signals as well as surface effects.

The high-loss spectrum corresponds to electrons that have suffered energy losses equivalent to energies to promote an electron from the core energy states of the atom to empty states in the valence band. Inner-shell excitations give rise to ionization edges at energies specific to the elemental composition of a specimen. The edge intensities can be related to the amount of the element present. [63] Ionization edges contain small fluctuations of intensity just above the corresponding edge designated as energy-loss near-edge structure (ELNES). This fluctuation provides information about bonding such as coordination, valence and type of bonding. The most distinctive ELNES feature of transition metal atoms are known as “white lines” which sit at the onsets of L_2 and L_3

absorption edges. These features arise from spin-orbit coupling meaning that the electron spin can couple in two ways with the angular momentum. A change in valence of an atom affects the ELNES in two distinct ways. First, a change in effective charge on an atom leads to shifts in the binding energies in the core level and final state in the ELNES. The second influence of valence on the L_2 and L_3 edges is their intensity distribution that arises from transitions from two 2p spin-orbital splits to unoccupied d levels in 3d transition metal elements. The relative intensities of the L_3 and L_2 peaks contain information about the occupancy of the final 3d orbitals which can be applied to determine the oxidation states of transition metal elements in some compounds. [63-67] Detection of light elements is a key advantage of EELS over EDS. In EEL spectra, the ionization edges in the high energy-loss region show relative low intensity (Fig 2-8), have an extended energy range above the ionization energy and have a high rapidly varying background. Furthermore as the energy-loss increases, the intensity of the ionization peaks dramatically decreases limiting the energy loss to approximately 1 keV. [62]

EELS spectrometry can provide a relationship between lithium ion battery materials composition and local atomic structure, which in turn dictate the performance of lithium ion batteries. EELS can reveal details about the electronic structure of the specimen which describes the nature of the atoms[68, 69], their bonding and nearest neighbor distributions[66, 70, 71].

2.2.3.3 Advanced analytical electron microscopy techniques

Probing materials to obtain information about the local atomic structure, chemical composition and bonding is necessary to understand the complexities of bulk materials and interfaces. This analysis will further develop the structure-property relationship. In

TEM mode, a broad beam interacts with the specimen and electrons are transmitted through the sample. Diffraction contrast dominates in low and medium magnification images; therefore, characterization of crystal defects is the main application of TEM. High resolution TEM (HRTEM) images are based on phase contrast, which form from the interference of the transmitted and refracted beams making interpretation complex. The image contrast in HRTEM can not be directly related to atomic columns. Moreover, in TEM mode, magnification is determined by the imaging lenses which are not ideal and have aberrations that reduce image quality. In scanning transmission electron microscopy (STEM), a sharply focused beam is used to illuminate the sample giving rise to high spatial resolution. A STEM image is formed by scanning the beam on the sample parallel to the optic axis. The key to this instrument is the formation of an electron probe of atomic dimensions. The STEM uses the same detectors as a traditional TEM including a bright field detector and an annular dark field detector that collects scattered electrons. As the angle of the annular dark field detector is increased away from the transmitted beam, the atomic number dependence of the image contrast is increased. This configuration is often referred to as a Z-contrast or high-angle annular dark field (HAADF) image. The scattered intensity by neighboring atomic columns are effectively averaged allowing each atom to be considered as an independent scatterer making image interpretation simpler than HRTEM. With these assumptions, the scattering factors of individual atoms may be replaced by cross sections that now have a $Z^{1.5} – Z^{1.7}$ dependence on atomic number.[72, 73] When the interatomic spacing of a major zone axis is larger than the full width at half maximum (FWHM) of the beam, the atomic columns are illuminated individually and atomic resolution can be directly achieved. [74] The magnification of the STEM image is not controlled by the lenses, but the scan dimensions on the specimen. The electron probe size can be minimized with a birght electron source and lens with small aberrations to focus the beam to the sub Angstrom level. The annular detector used in Z-contrast image does not interfere with low angle scattering used for EELS. Therefore, EELS and Z-contrast image can be used in conjunction to position the electron probe over specific structural features for analysis. [63, 75-77] The combination of HAADF and EELS enables the STEM to characterize complex interface problems using analytical and imaging techniques with atomic resolution.

2.3 Using Diffraction For Structural Determination

Regardless of the source of radiation, the wave-like interaction of the incident beam and the sample generate diffracted beams. The periodic arrangement of atoms within a crystal cause distinct patterns of constructive and destructive interference to form. When constructive interference forms, a Bragg reflection is observed. These reflections can be characterized by parameters defining the position, maximum intensity, area, shape and asymmetry. The number of peaks or spots observed in a diffraction pattern depends primarily on the symmetry, size of the unit cell and arrangement of atoms within the unit cell. The integrated intensity or area under a diffraction peak (*I*) for a random sample is given by

$$I = F_{hkl}^2 \lambda^3 V^{-2} PL \tag{2-10}$$

where F_{hkl}^2 is the structure factor, λ is the wavelength, *V* is the volume of the unit cell, P is the polarization factor and *L* is the Lorentz factor. The structure factor F_{hkl} is a mathematical description of how a crystal scatters incident radiation. It is shown by:

$$F_{hkl} = \sum_j f_j e^{-i\Delta \boldsymbol{k}\cdot\boldsymbol{r}_j} \tag{2-11}$$

where $\mathbf{r}_\mathrm{j}$ is the position of an atom j in the unit cell. F_j is the atomic form factor which is a measure of the scattering amplitude of a wave by an isolated atom. To compute the structure for a hexagonal structure is given by the following derivation:

$$|F|^2 = f^2 \exp(2\pi i(0) + f \exp(2\pi i(h/3 + 2k/3 + l/2)$$

$$|F|^2 = f[1 + \exp(2\pi i(h+2k)/3 + l/2]$$

$$|F|^2 = f^2(2 + 2\cos(2\pi g)$$

$$|F|^2 = f^2[2 + 2(2\cos^2 \pi g - 1)]$$

$$|F|^2 = f^2(4\cos^2 \pi g$$

$$|F|^2 = 4f^2 \cos^2 \pi\left(\frac{h+2k}{3} + \frac{l}{2}\right) \tag{2-12}$$

The rules of diffraction for a hexagonal structure are

- If ($h+2k$) is a multiple of 3 and is l odd ➔No reflection
- If ($h+2k$) is a multiple of 3 and l is even ➔ Reflection
- If ($h+2k$) is not a multiple of 3 ➔ Reflection

For analysis of powder diffraction, the method of total pattern fitting introduced by Rietveld has been widely adopted by crystallographers. Through the use the Rietveld refinement process the 3-D crystallographic information can be interpreted from diffraction patterns. [78] Rietveld refinement is a refinement process; therefore, an initial approximation of the crystal structure is required. Prior knowledge of the structure and chemistry must be gathered from additional techniques including synthesis, first principles techniques and chemical composition analysis.

The method uses a total pattern fitting with a least squares approach to match a theoretical line profile with the measured profile. The method implements two models that approximate atomic positions and the reflections in terms of instrumental functions. The calculated at a given position θ_i is given by:

$$y_i(calc) = \sum_{j=1}^{Nphases} \frac{f_j}{V_j^2} \sum_{k=1}^{Npeaks} |F_{k,j}|^2 L_k P_{k,j} S_j\left(2\theta_i - 2\theta_{k,j}\right) A_j + yb_i(obs) \qquad (2\text{-}13)$$

The summation over all reflections and phases contribute to the intensity at θ_i. In Equation (2-12) yb_i, S_j, $P_{k,j}$, L_k, A_j are parameters associated with background, scale factor, polarization, Lorentz factor, and absorption respectively. The parameters f_j and V_j are the atomic form factor and volume for the respective phase. The *profile* of each reflection is determined by the profile function ($2\theta_i$-$2\theta_{k,j}$). In powder diffraction, if the breadths of the line profiles vary smoothly with ***d****, the variation of the full width at half maximum (FWHM) is expressed as a quadratic in tanθ. This was introduced by Caglioti, Paoletti and Ricci [79] to describe peak broadening as given by:

$$(FWHM)^2 = U\tan^2\theta + V\tan\theta + W \qquad (2\text{-}14)$$

where *U,V*, and *W* are refinable peak shape parameters. In powder diffraction, a many peak shape function are used to fit the diffraction peaks. Common functions include Gaussian, Lorentzian and Pearson VII or pseudo-Voigt. The pseudo-Voigt profile function is a convolution of Gaussian and Lorentzian functions. [80-83] At low scattering angle, there is evidence of peak asymmetry resulting from the measurement geometry that can be refined or calibrated. [80] Moreover, broadening of peak reflections are related to crystallite size and microstrains forming in a material. The crystallite size contributions are independent of ***d**** and are modeled according to the Debye-Scherrer equation [84]:

$$L = \frac{K\lambda}{\beta \cos \theta} \tag{2-15}$$

where β is integral breadth of a of a given *hkl* reflection, λ is the wavelength, K is Scherrer's constant and L is the crystallite size in the perpendicular direction to the reflecting planes. The microstrain contributions to peak broadening are dependent on ***d**** and were first modeled by Stokes and Wilson given by [85]:

$$\varepsilon_{strain} = \frac{\beta}{4 \tan \theta} \tag{2-16}$$

where ε_{strain} is the weighted average strain and β is the integral breadth of a of a given *hkl* reflection. Williamson and Hall proposed a method for deconvoluting the size and strain broadening by looking at peak width as a function of peak position. The analysis considers the contributions of crystallite size and microstrain in X-ray line broadening to be additive where:

$$\beta_{total} = \beta_{particle\ \ size} + \beta_{strain} \tag{2-17}$$

substituting the integral breadths from the Scherrer equation and Stokes and Wilson's observations, the final Williamson-Hall equation is obtained when both sides of the equation are multiplied through by cosθ giving:

$$\beta_{total} \cos \theta = \frac{K\lambda}{L} + 4 \sin \theta \ (\varepsilon_{strain}) \tag{2-18}$$

The strain is extracted from the slope and the crystallite size can be extracted from the y-intercept of the plot of βcosθ versus 4sinθ. The broadening from Williamson-Hall type microstrain can be explained by non-uniform strain effects originating from systematic shifts of atoms from their theoretical positions. Figure 2-9 shows the plot of βcosθ versus 4sinθ for $Li[Ni_xLi_{1/3-2x/3}Mn_{2/3-x/3}]O_2$ materials before and following electrochemical cycling. The conventional Williamson-Hall plot analysis does not recognize when strain broadening from the material is caused by dislocations.[86]

Recently large amounts of work has shown that strain broadening caused by dislocations can be described in terms of a logarithmic series expansion.[86, 87] The use of a modified Williamson-Hall plot can be used to improve the explanation of line broadening when significant amounts of strain is caused by dislocations in the material. Figure 2-10 shows the conventional Williamson-Hall plot (Fig 2-10A) for a ultra fine grained copper with large amounts of dislocations. The modified Williamson-Hall equation developed by Ungar *et. al.* uses a scaling factor of the integral breadths that is dependent on $4\bar{C}^{1/2}\sin\theta$ instead of merely $4\sin\theta$ which shows an improved fit in Figure 2-10B where $\bar{C}$ corresponds to the average contrast factor of dislocations. $\bar{C}$ is calculated from the slip systems and edge and screw dislocations.[86, 88]

2.3 Synthesis

2.3.1 Coprecipitation

Materials used in this thesis were prepared by the coprecipitation method. The techniques uses the salt compounds of two precursors dissolved in aqueous solutions and precipitated by pH adjustment. Typically oxalates, citrates, carbonates or hydroxides are the resulting precipitate because of low aqueous solubility. This particle synthesis technique requires minimal experimental setup and is easily scalable making it advantageous for commercial applications. The standard operating procedure for the coprecipitation synthesis technique can be found in Appendix A.

2.3.2 Electrochemistry

All cathodes used in this work were prepared by mixing the active layered lithium transition metal oxide with 10 wt% Super P carbon (TIMCAL) and 10 wt% poly-vinylidene fluoride (PVDF) in N-methyl pyrrolidone (NMP) solution. The slurry was cast onto an Al foil using a doctor blade and dried in a vacuum oven at 80°C. The electrode discs were punched and dried again at 80°C for 6 hrs before storing them in an argon filled glove box (H_2O level < 2ppm). The active material loading of the cathode disks is approximately 5 – 10 mg/cm^2. An argon filled glovebox is necessary to reduce exposure to moisture which is harmful to both the lithium foil anode and electrolyte. All electrochemical property tests were performed using a 2016 type coin cell. Lithium metal ribbon and 1M $LiPF_6$ in a 1:1 ethylene carbonate: dimethyl carbonate (EC:DMC) solution (Novolyte) were used as the counter electrode and electrolyte, respectively. Celgard model C480 separator (Celgard Inc, USA) was used as the separator. The coin cells were tested on an Arbin battery cycler in galvanostatic mode.

2.3.3 Cathode Preparation

Samples that were characterized following electrochemical cycling were recovered by disassembling the coin cell in an argon filled glovebox. The cathode was washed by submerging in Acetonitrile (H_2O<10ppm) 3 times. The cathode was allowed to dry in Argon atmosphere overnight. The powder was removed from the aluminum current collector and exposure to the ambient atmosphere minimized.

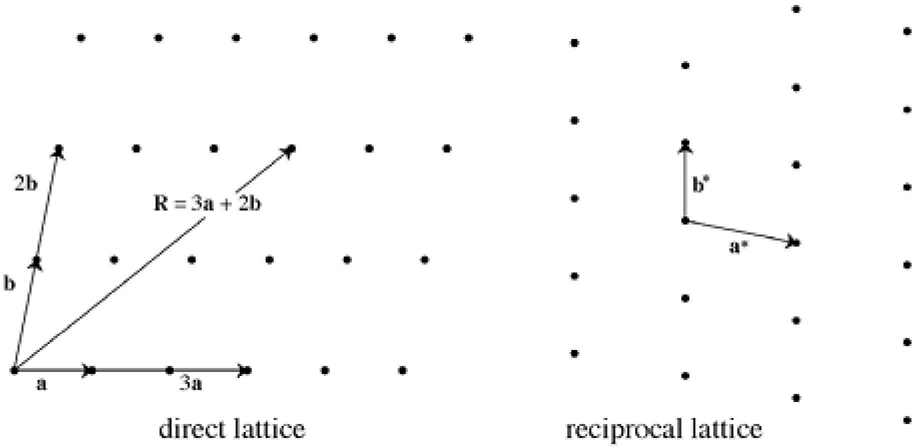

Figure 2-1. Relationship between a direct lattice and a reciprocal lattice.

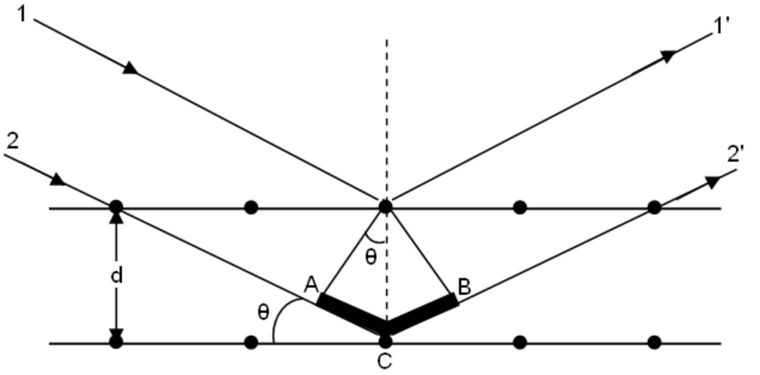

Figure 2-2. Schematics of Braggs law by planes of atoms

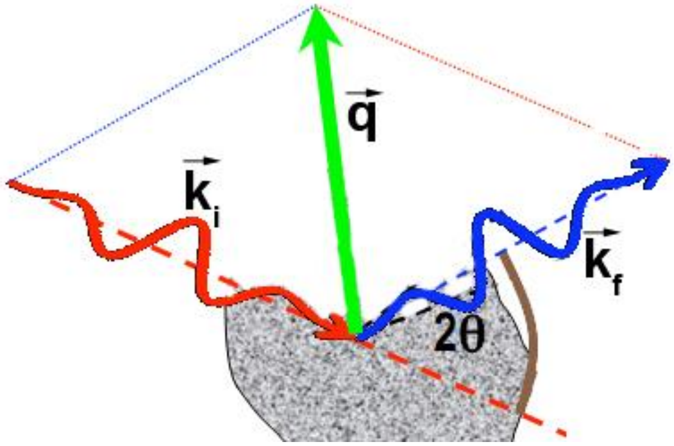

Figure 2-3. Relationship between $\overrightarrow{k_i}$ and 2θ for elastic scattering

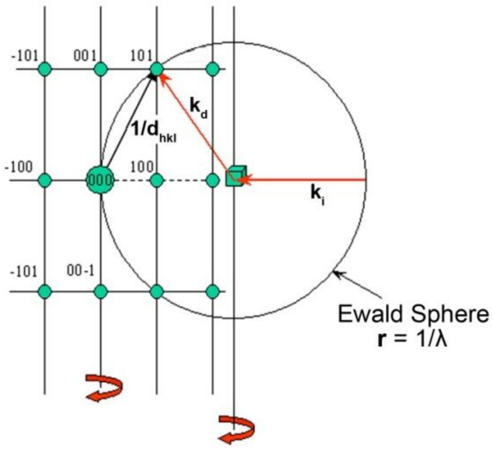

Figure 2-4. Ewald Sphere construction

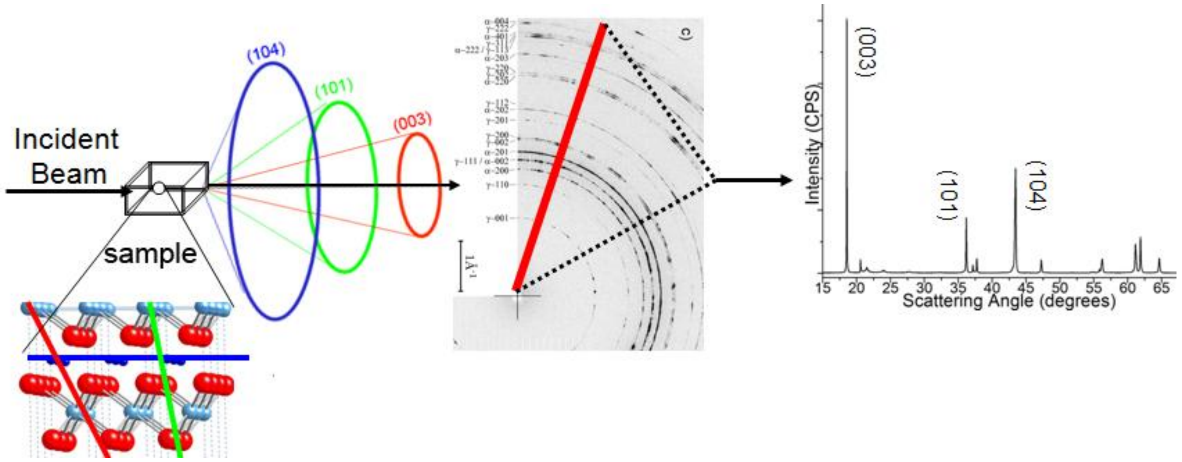

Figure 2-5. Radiation incident upon a 3-dimensional structure interacts with 3 planes, (003) in blue, (101) in green and the (104) plane, are scattered in 2-dimensional Debye-Scherrer rings which are reduced by typical X-ray diffraction detectors into a 1-D line diffraction pattern.

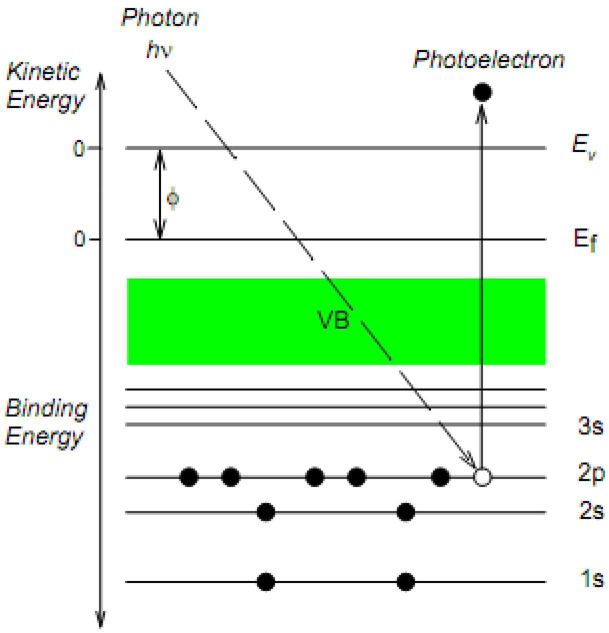

Figure 2-6. Schematic diagram of the XPS process including photoionization of an atom by the ejection of a 2p electron.

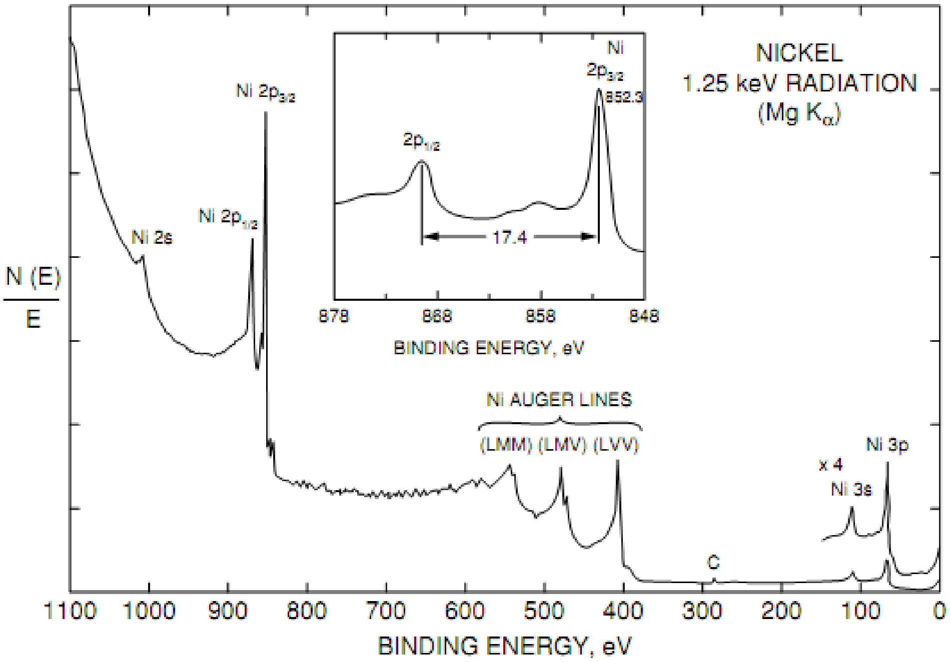

Figure 2-7. The XPS survey energy spectrum from Ni acquired using Mg K_α radiation. The energy axis is expressed in terms of binding energy ($hv - E_K$).[50]

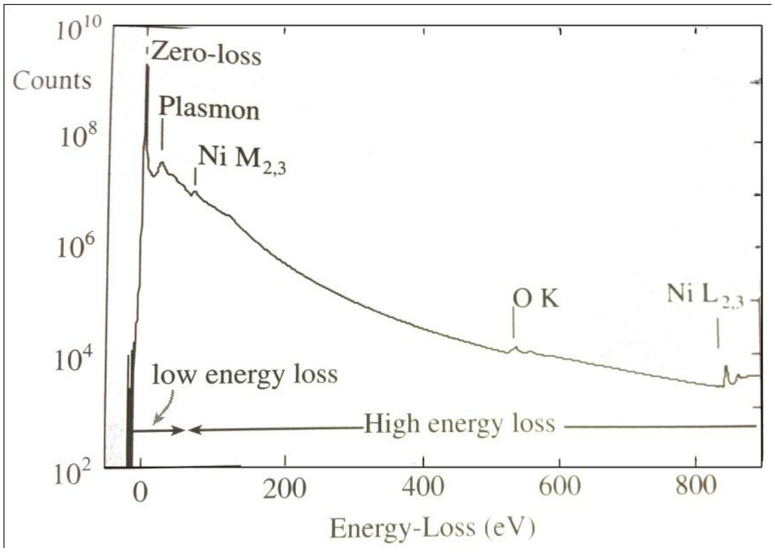

Figure 2-8. An EELS spectrum displayed in logarithmic intensity showing the zero-loss, low energy-loss and high energy-loss regions. [62]

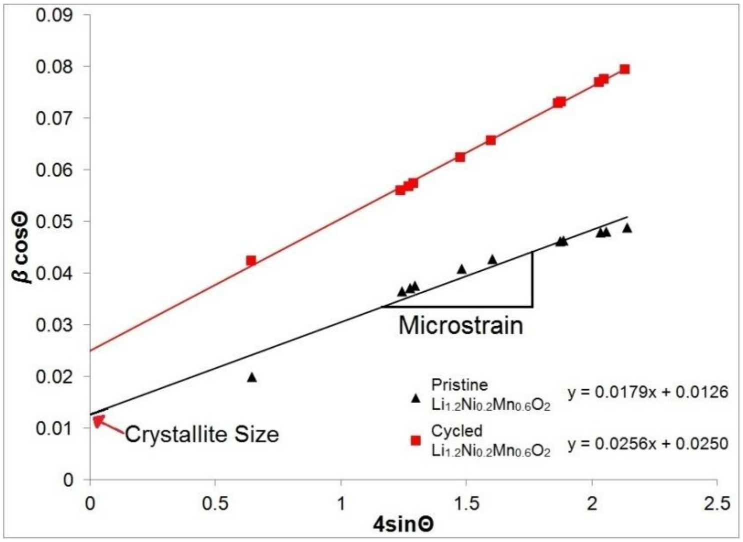

Figure 2-9. Williamson-Hall plot of $\beta\cos\theta$ versus $4\sin\theta$ for $Li[Li_{1/3-2x/3}Ni_xMn_{2/3-x/3}]O_2$ before and following electrochemical cycling.

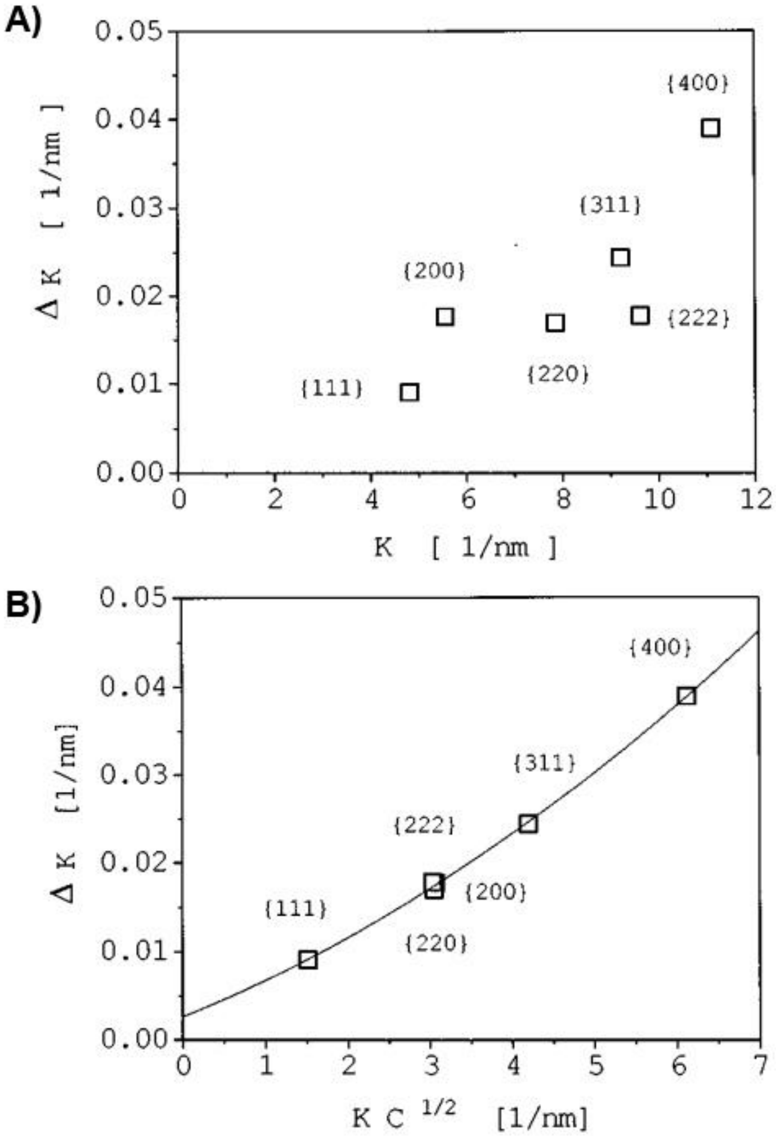

Figure 2-10. Williamson-Hall plots from ultra fine grain copper using the A) conventional equation and the B) modified equation[86]

CHAPTER 3

STRUCTURAL ANALYSIS OF LAYERED LITHIUM-EXCESS OXIDE ELECTRODE MATERIALS: IDENTIFYING THE SYNTHESIS—STRUCTURE—PROPERTY RELATIONSHIP

The core of this chapter is based on the paper "Synthesis – Structure – Property Relations in Layered, Lithium-Excess" Oxides Electrode Materials $Li[Li_{1/3-2x/3}Ni_xMn_{2/3-x/3}]O_2$ (x=1/3, 1/4 and 1/5)" by Christopher R. Fell., Kyler J. Carroll, Miaofang Chi, and Ying Shirley Meng, Journal of the Electrochemical Society, volume 157, issue 11, 2010 page A1202.[89] *Reproduced by permission of ECS – The Electrochemical Society.* a-STEM and EELS was operated by Miaofang Chi and the XPS was operated by Kyler J. Carroll.

The background in Chapter 1 identified that the lithium-excess layered oxide compounds $Li[Ni_xLi_{1/3-2x/3}Mn_{2/3-x/3}]O_2$ ($0 \leq x \leq 1/2$) are of great interests as a new generation of positive electrode materials for high energy density lithium ion batteries. This material family can be viewed as a solid solution between the two end members, Li_2MnO_3 and $Li[Ni_{1/2}Mn_{1/2}]O_2$ [18], though alternatively it can be expressed as a composite $xLi[Li_{1/3}Mn_{2/3}]O_2$ $(1-x)LiNi_{1/2}Mn_{1/2}O_2$ [20] Efforts to improve the performance of layered $LiMO_2$ cathode materials involve a deep understanding of the connection between synthesis, crystal structure and electrochemical properties. Previous research has identified multiple charge compensation mechanisms that account for the anomalous capacities observed during the first electrochemical charge cycle. Significant efforts have been devoted to reduce the first cycle irreversible capacity with ionic substitutions, preconditioning the material with acidic substitutions and surface modifications. All of these techniques have shown improvements on cycling. However, the reasons for the improvement through the use of substitutions and acid conditioning are complex and not well understood.[90] Surface modifications also improve cell polarization and rate capabilities as shown by previous work as explained in Chapter 1. Not only are the electrochemical properties of the lithium-excess layered compounds influenced from structural modifications, but the synthesis route plays a significant role. Layered transition metal oxides can be synthesized through a wide variety of chemical synthesis routes. $LiCoO_2$ It was reported that as the synthesis sintering temperature increases from 800 to 1000°C, the lattice parameters and the *c/a* ratio increase and the amount of cation disorder decreases resulting in an improved reversible discharge capacity.[91]

In order to systematically study the remarkable synthesis-structure-property relations of $Li[Ni_xLi_{1/3-2x/3}Mn_{2/3-x/3}]O_2$, this chapter investigates the compounds synthesized with different precursor stoichiometry, nickel content (x=1/3, 1/4, and 1/5), synthesis temperature, atmosphere and cooling rates. X-ray diffraction, X-ray photoelectron spectroscopy (XPS), transmission electron microscopy (TEM) and Electron Energy-Loss Spectrometry (EELS), combined with electrochemical property measurements including potentiostatic intermittent titration technique (PITT) were carried out to study the structural differences associated with various synthesis conditions before, during and after electrochemical processes.

3.1 Experiments

3.1.1 Sample Preparation

$Li[Ni_xLi_{1/3-2x/3}Mn_{2/3-x/3}]O_2$ materials were prepared by the coprecipitation method using a carbonate based and hydroxide based double transition metal precursor.

3.1.1.1 Hydroxide based coprecipitation

Transition metal nitrates, $Ni(NO_3)_2$ $6H_2O$(Fischer) and $Mn(NO_3)_2$ $4H_2O$ (Fisher), were dissolved into 50 mL of deionized water then titrated into a 400 mL $LiOH{\cdot}H_2O$

solution for a duration of two hours. Both stoichiometric and excess amounts of $LiOH \cdot H_2O$ solution were used for the coprecipitation step. The reason for the excess amount of $LiOH \cdot H_2O$ solution was used to ensure complete precipitation of the transition metal (TM) double hydroxide, $(Ni_xMn_{2/3-x/3})(OH_2)$. These materials will be referred to as being prepared via the hydroxide route. The co-precipitated transition metal hydroxides were then filtered using a vacuum filter and washed three times with deionized water. The collected transition metal hydroxides were dried in an oven at 180 °C for 10 hours in air. The dried transition metal precursors were mixed with a stoichiometric amount of $LiOH \cdot H_2O$ corresponding to the amount of $M(OH)_2$ from the coprecipitation step. This mixture was ground for 30 minutes to ensure adequate mixing and then placed into a furnace at 480 °C for 12 hours. The pre-calcinated powders were prepared as a pellet or in powder form for high temperature sintering. These samples were then calcinated at 900 or 1000°C for 12 hours in air or in oxygen. Samples were brought back to room temperature by quenching with metal plates or furnace cooling.

3.1.1.2 Carbonate based coprecipitation

Two independent solutions were initially prepared, a 2M acidic solution of transition metal sulfates, $Ni(SO_4)$ $6H_2O$ (Sigma-Aldrich) and $Mn(SO_4)$ H_2O (Sigma Aldrich) and 2M basic solution of Na_2CO_3 (Sigma-Aldrich). A chelating agent with 0.3M NH_4OH was added to the basic solution. The coprecipitation temperature was set at 50°C and the pH value was fixed to 8.0. The acidic and basic solutions were pumped into a continuously stirred tank reactor. The particles were collected following continuous stirring at 1000 rpm for 8 hr. The particles were filtered from the aqueous medium, washed several times after filtration and dried inside a vacuum oven at 110°C overnight. The collected transition metal carbonates $Ni_xMn_yCO_3$ were well mixed with a stoichiometric amount of Li_2CO_3 (Aldrich). These materials will be referred to as being prepared via the carbonate route. The mixture was ground for 30 minutes to ensure adequate mixing. The mixture was heat treated in air in two steps: calcinations t 500°C for 12 hr to decompose the carbonate precursors and a final sintering at 900°C for 12 hr to obtain the lithiated compounds. Powder samples were also obtained from Deng *et al*. for comparison. [92]

3.1.2 X-Ray Diffraction

Powder diffractions of all samples were taken using a laboratory x-ray diffractometer equipped with a curved position sensitive detector (CPS120, Inel, detection range 0-120˚), a Cu X-ray tube source and a Göbel mirror on the incident beam. XRD data analysis was carried out by Rietveld refinement method using FullProf software. [93] Special Notes: Mn fluorescence radiation from the sample is believed to be the reason for the poor R_B factor (even though R_{wp} is excellent).

3.1.3 ICP-OES

The lithium, nickel and manganese contents in the pristine samples were determined using atomic absorption spectroscopy using a Perkin-Elmer Plasma 3200 Inductively Coupled Plasma Spectroscopy (ICP-OES) system. The instrument is equipped with two monochromators covering the spectral range of 165-785 nm with a grated ruling of 3600 lines/mm. The system is capable of analyzing materials in both organic and aqueous matrices with a detection limit range of less than 1 part per million. The instrument was initially calibrated using commercial $LiCoO_2$ and $LiFePO_4$ powders.

3.1.4 SEM

The particle morphology and size of the powders were determined using a JEOL 6320FV Field Emission High-resolution Scanning Electron Microscope (SEM). Images were collected with an accelerating voltage of 15 kV.

3.1.5 TEM

TEM images were collected from both the pristine sample powders and the powders discharged to 2.0 V after being charged to 4.8 V. To minimize the exposure to air for the electrochemically charged/discharged samples, the samples were prepared in an argon environment. The powders were suspended on a copper grid with lacey carbon and investigated by using a JEOL 2010F microscope with an accelerating voltage of 200 kV and a field emission gun. The samples were briefly exposed to air (< 1 minute) when loaded on to the TEM grid, before transferred into the microscope UHV column.

3.1.6 EELS

EELS spectra presented in this work is carried out in an aberration corrected Titan 80/30 microscope equipped with a Gatan Imaging Filter 2002F. Each spectrum was acquired from a square area of ~1*1 nm with an acquisition time of 2 seconds and a collection angle of ~10 mrad. To minimize possible electron beam irradiation effects on EELS fine structures, all EELS spectra presented here are acquired from areas without pre-beam irradiation.

3.1.7 XPS

The powdered samples were pressed onto a strip of indium foil and mounted onto a sample holder using double-sided adhesive tape. X-ray photoelectron spectroscopy (XPS) was performed on a Thermo Scientific ESCALAB 250 microprobe with a focused monochromatic Al Kα X-ray (1486.6 eV) source. A 180° hemispherical analyzer with a 16-element multichannel detector was used. The incident X-ray beam was 45° off normal to the sample while the X-ray photoelectron detector was normal to the sample. Charge compensation was employed during data collection by using an internal flood gun (1 eV, 20 uA electrons) and a low energy Ar+ external flood gun. Binding energies of the photoelectron are correlated to the aliphatic hydrocarbon C 1s peak at 284.6 eV. A Large area XL magnetic lens with a 500 μm spot size in constant analyzer energy (CAE) mode was utilized with a pass energy of 20 eV. 30 scans per region were taking with a step size of 0.100 eV.

3.1.8 Electrochemistry

Cathodes were prepared as discussed in Chapter 2. The potentiostatic intermittent titration technique (PITT) experiment was carried out by applying potential steps of 10 mV and measuring the current as a function of time. The potential step was stepped to the next level when the measured current fell below the threshold limit of 10 μA, corresponding to a C/200 rate. The voltage window was set at 4.8 – 3.0 V.

3.2 Results

3.2.1 Composition Analysis

Table 3-1 lists the atomic compositions of $Li[Ni_xLi_{1/3-2x/3}Mn_{2/3-x/3}]O_2$ electrode materials synthesized with the hydroxide route for this study obtained from ICP-OES analysis. For LiOH excess samples, the Ni/Mn ratios for x=1/3, 1/4 and 1/5 are in agreement with the target stoichiometry; however, the lithium values were, on average, approximately 5-10% higher than anticipated values based on ICP-OES analysis. For the stoichiometric samples, where no excess LiOH was used, the experimental Li/Ni/Mn ratios are in good agreement with the target stoichiometry.

3.2.2 X-Ray Diffraction

X-ray diffraction spectra for the LiOH-excess Li[Ni$_x$Li$_{1/3-2x/3}$Mn$_{2/3-x/3}$]O$_2$ samples synthesized at 1000°C are depicted in Figure 3-1. Table 3-2 lists the results of the Rietveld refinement for the XRD spectra shown in Figure 3-1. Major diffraction peaks of the Li[Ni$_x$Li$_{1/3-2x/3}$Mn$_{2/3-x/3}$]O$_2$ material are indexed according to the parent hexagonal structure with space group $R\bar{3}m$. The patterns indicate that although excess lithium is present, the sample adopts a well layered structure with little Li/Ni interlayer mixing evidenced by the existence of doublets at (006)/(102) and (108)/(110). The superlattice peaks between 20-30° 2Θ can be clearly seen and their intensity increases with increasing amount of Li in the TM layers. Such superstructure peaks are associated with a honeycomb ordering of Li, Ni and Mn in the TM layers. [21, 94]

X-ray diffraction data for stoichiometric hydroxide based Li[Ni$_x$Li$_{1/3-2x/3}$Mn$_{2/3-x/3}$]O$_2$ samples where x=1/5, 1/4 and 1/3 are seen in Figures 3-2A, 3-2B and 3-2C respectively. The XRD pattern for carbonate synthesis based Li[Ni$_x$Li$_{1/3-2x/3}$Mn$_{2/3-x/3}$]O$_2$ sample where x=1/5 is seen in Figure 3-3. For both synthesis techniques, the superlattice peaks at 20-30° 2Θ are distinct. Table 3-2 lists the results of the Rietveld refinement for the XRD spectra shown in Figure 3-2 and Figure 3-3. It is clear that the synthesis technique does not have a significant effect on the lattice parameters nor the amount of interlayer Li/Ni mixing. Consistent with what is observed in LiOH-excess samples, the lattice parameters and the amount of interlayer Li/Ni mixing increases as the value of x increases in Li[Ni$_x$Li$_{1/3-2x/3}$Mn$_{2/3-x/3}$]O$_2$. In addition, the *c/a* ratio decreases for increasing values of x, which supports the work of Lu et al who similarly found that as the value of x increases, the c/a ratio decreases and the amount of Li/Ni mixing increases. [91] Stoichiometric hydroxide route Ni1/5 samples were also synthesized under a range of conditions to determine the effect of sintering temperature, cooling rate, and synthesis atmosphere. X-ray diffraction patterns of pellet samples synthesized at differing temperatures and cooling rates can be seen in Figure 3-4A-D. As shown in Figures 3-4A and 3-4B, heating the stoichiometric Ni1/5 samples at 900°C requires a fast cooling rate to obtain phase pure compound. If furnace cooled, the stoichiometric Ni1/5 sample consists of a second phase indicated by shoulders next to the (003), (101) and (104) peaks. For stoichiometric samples sintered at 1000˚C, however, samples that were furnace cooed, as illustrated in Figure 3-4C, showed a lower Li/Ni interlayer mixing on the 3a sites versus that of quenched samples (Figure 3-4D), seen in Table 3-3.

For LiOH excess samples, we found that the sample synthesized at 1000°C shows increased c/a ratio and decreased interlayer Li/Ni mixing, compared to that synthesized at 900°C. Figure 3-5A compares the LiOH excess samples synthesized at 900°C and 1000°C. The results in Figure 3-5A show more distinct superlattice peaks evident in the sample synthesized at 1000°C and only a broad peak is observed in 20-30° range for the 900°C sample. The effect of cooling rate was also studied for LiOH excess samples. Our results illustrated that quenching or furnace cooling does not have a critical effect on the XRD pattern of LiOH-excess samples. Changing the atmospheric condition from air to oxygen imposed no changes to the XRD patterns. Table 3-4 shows Rietveld refinement results from varying temperature and cooling rate during synthesis. These different synthesis conditions have statistically negligible effects showing nearly identical lattice parameters and Li/Ni mixing within experimental error. Comparison of XRD spectra from electrochemically cycled stoichiometric hydroxide route and carbonate route $Li[Ni_{1/5}Li_{1/5}Mn_{3/5}]O_2$ (x=1/5) samples are depicted in Figure 3-6. The hydroxide (Figure 3-6B) and carbonate (Figure 3-6D) route samples that were electrochemically charged and discharged (between 4.8 V-2.0 V) for ten cycles remain phase pure without XRD peaks from secondary phases. The inserts in Figure 3-6 show that the superstructure peaks weaken their intensities following the first cycle and become undetectable after ten cycles, consistent with what has been previously observed for Ni1/3 compound. [95] Rietveld refinement (Table 3-5) of the XRD spectra of the cycled samples reveals an overall lattice expansion and a significantly increased c/a ratio compared with the pristine materials, assuming a single phase layered structure.

The XRD patterns of cycled LiOH excess $Li[Ni_{1/5}Li_{1/5}Mn_{3/5}]O_2$ samples are compared in Figure 3-7. Similar to the stoichiometric compounds, the intensity of the superlattice peaks of the sample significantly decreased after the first cycle and disappeared after 10 cycles. Different from the stoichiometric compounds, the intensity ratio of (003)/(104) becomes much less than unity and the (110) peak intensity increases dramatically in the sample after ten cycles (Figure 3-7A), indicating the loss of layeredness in the material. The Rietveld refinement results of the cycled LiOH excess materials can be seen in Table 3-5 and the results show that the amount of Li/Ni mixing increases slightly after the first cycle. The c/a ratio increases after the first and 10th cycles indicating an expanded structure.

3.2.3 SEM

Scanning electron microscopy (SEM) was performed to study the morphology and particle size of $Li[Ni_xLi_{1/3-2x/3}Mn_{2/3-x/3}]O_2$ obtained under different synthesis conditions. Figure 3-8 compares Ni1/5 samples synthesized using the hydroxide and carbonate routes during the coprecipitation stage. Figures 3-8A and 3-8B illustrate stoichiometric hydroxide route samples after 1000°C firing with average particle sizes of

100-300nm. Samples synthesized using the carbonate route in Figures 3-8C and 3-8D show a distinctly different in particle shape. The carbonate based synthesis produced uniformly sized, dense spherical particles where as the hydroxide method produced random shapes with a wide distribution of secondary particle. The secondary particle size distribution for the carbonate based synthesis ranges from 1-5μm.

3.2.4 TEM/EELS

Figures 3-9 and 3-10 are TEM micrographs and EELS spectra of the Oxygen K-edge of the hydroxide route stoichiometric and LiOH excess $Li[Ni_{1/5}Li_{1/5}Mn_{3/5}]O_2$ samples, respectively. The data from various grains were very similar; therefore, only representative data is presented. Figure 3-8A is a TEM bright field image showing that the stoichiometric particles have a clean and well defined surface with excellent crystallinity. On the contrary, the LiOH excess sample shows poor crystallinity at the surface. Preliminary EELS data we collected confirm that the bulk vs. surface uniformity is excellent in the stoichiometry sample, as depicted in Figure 3-9A. The O-EELS spectra of the surface and the bulk are identical. On the contrary, the O-EELS spectra from the LiOH excess sample (Figure 3-9B) show significant difference in the local environment of the oxygen: the pre-edge peak intensity decreases considerably at the surface and the profile of the EELS spectra changes at the surface. TEM micrographs of the carbonate route $Li[Ni_{1/5}Li_{1/5}Mn_{3/5}]O_2$ samples are seen in Figure 3-11. Comparison of the TEM images of the hydroxide route and carbonate route samples reveal excellent crystallinity in the bulk and at the surface. Quantitative analysis of TEM and EELS results will be reported in Chapter 5.

3.2.5 XPS

XPS measurements were taken on as-synthesized stoichiometric and LiOH excess $Li[Ni_{1/5}Li_{1/5}Mn_{3/5}]O_2$ samples. The multiplet data of the Mn, Ni $2p_{3/2}$ and Oxygen 1s peaks can be seen in Figure 3-12A, 3-12B, and 3-12C respectively. The binding energies from the XPS measurements are found in Table 3-6. The $Mn2p_{3/2}$ binding energies observed for the stoichiometric and LiOH excess materials were 642.45 and 642.29eV respectively, and the binding energy values agree with the standard for Mn^{4+} [96], though trace amount of Mn^{3+} indicated by the broadening of the peaks. The fraction of Mn^{3+} is higher in LiOH excess sample than stoichiometric sample as the average Mn 2p3/2 binding energy for LiOH excess sample is slightly lower than that of the stoichiometric sample. This implies the presence of trace amount of Ni^{3+} on the surfaces and the fraction of Ni^{3+} is higher in the LiOH excess sample. A $Ni2p_{3/2}$ satellite peak at 861eV was observed for both samples indicating splitting in the energy levels. [97] The Ni 2p spectra in Figure 3-12B show a mixed valence state material with Ni^{2+} and Ni^{3+}. A slight shift in the binding energies for both materials can be seen which equates to different fractions of Ni^{2+} and Ni^{3+}. The Ni $2p_{3/2}$ peak for the LiOH excess sample shows a larger high binding energy shoulder with respect to the stoichiometric sample indicating increased presence of Ni^{3+} at the surface. The O 1s XPS spectra in Figure 3-12C show two peaks located at ~532 and ~529 eV that correlates to OH^- and O^{2-} environments, respectively. An increase in the 532 eV peak for the LiOH excess sample indicates OH- ions are possibly adsorbed onto the surface of the sample.

3.2.6 Electrochemistry

Electrochemical measurements of $Li[Ni_xLi_{1/3-2x/3}Mn_{2/3-x/3}]O_2$ electrodes were performed in lithium half-cells cycled between 2.0 to 4.8 V. Figure 3-13 shows charge-discharge electrochemical data from stoichiometric samples of hydroxide route $Li[Ni_xLi_{1/3-2x/3}Mn_{2/3-x/3}]O_2$ where x=1/3, 1/4 and 1/5. During the first charge cycle, the voltage increases monotonically until ~4.4 V, which can be attributed to the redox reaction of Ni^{2+} to Ni^{4+}. [95] A plateau-like region can be observed between 4.4 V and 4.6 V upon first charge. The electrochemical voltage profile for the carbonate route $Li[Ni_{1/5}Li_{1/5}Mn_{3/5}]O_2$ (x=1/5) sample is identical to that of the hydroxide route x=1/5 sample. The charge and discharge capacities are 310 mAh/g and 255 mAh/g respectively. It can be noted as the amount of Nickel increases, the discharge capacity and length of the plateau region decreases, consistent with the previous reports on this family of materials. A summary of the theoretical capacity based on the Ni redox, the theoretical capacity based on total amount of Li and the actual discharge capacity is depicted in Table 3-7. The Mn oxidation state was considered 4+ for capacity calculations. The comparison clearly shows that when $x<1/3$, much more discharge capacity than Ni-redox capacity can be obtained. Figure 3-14 compares the charge-discharge curves from a LiOH excess Ni1/5 (x=1/5) sample to a stoichiometric Ni1/5 sample. During the first charge cycle, the voltage in both cells increase monotonically until 4.4 V and reach a plateau region between 4.4 and 4.6 V. However, for the LiOH excess sample, a second plateau appears at the end of charging, and the discharge capacity is 20% less than that of the stoichiometric sample. We observe this phenomenon consistently for all cells we made and also in Ni1/4 (x=1/4) cells.

Capacity versus cycle number of $Li[Ni_{1/5}Li_{1/5}Mn_{3/5}]O_2$ electrodes cycled between 2.0 and 4.8 V are compared in Figure 3-15 for stoichiometric and LiOH excess samples. The data suggests the cycling stability is not affected by the presence of excess lithium in LiOH excess samples. For the LiOH excess Ni1/5 sample, the reversible capacity decreases from about 185 to 155 mAh/g at C/50 and C/20 respectively. For the stoichiometric sample, the reversible discharge capacity exceeds 200 mAh/g at C/20. The differences in the stoichiometric and LiOH excess samples will be discussed in details in a later section.

A comparison of the discharge rate capability between stoichiometric hydroxide route and carbonate route $Li[Ni_{1/5}Li_{1/5}Mn_{3/5}]O_2$ (x=1/5) can be seen in Figure 3-16. The carbonate route synthesis resulted in higher capacities at all discharge rates. The effect becomes increasingly significant at 1C and 2C rates where the capacities are 20 and 60% larger, respectively.

The effects of temperature and cooling rate on the electrochemistry properties of the stoichiometric hydroxide route sample, where x=1/5, were also investigated. Quenched samples synthesized at 900°C and 1000°C were tested and the results are illustrated in Figure 3-17. The charging capacities of the materials are similar for both quenched samples; however, the discharging capacity for the 900°C material decreased to 210 mAh/g and the discharge voltage is lower and unstable compared to that of 1000°C sample. A comparison of a pellet sample furnace cooled versus quenched from 1000°C (shown in Figure 3-17) suggests that furnace cooling leads to better overall electrochemical properties of the $Li[Ni_xLi_{1/3-2x/3}Mn_{2/3-x/3}]O_2$ when $x < 1/2$.

3.2.7 Potentiostatic Intermittent Titration Technique (PITT)

3.2.7.1 Background

Electrochemical techniques are used for the study of transport within solids. Electrochemical methods are attractive because the thermodynamic and transport quantities can be converted into easily measurable electrical quantities such as voltages and currents. The techniques typically displace the electrode system from equilibrium or steady state by the application of a potential or current and measure the other variable as a function of time. Potentiostatic intermittent titration technique involves the application of a sudden step in the potential across the cell. The concentration of the mobile Li^+ species changes within the host $Li[Ni_{1/5}Li_{1/5}Mn_{3/5}]O_2$ material. Chemical diffusion will occur due to the concentration gradient imposed on the cathode material. Therefore, the electroactive Li^+ species must continuously be supplied by transport through the electrolyte to maintain uniform concentration at the surface. The dependent variable, the transient current provides a measure of the chemical diffusion flux as a function of time. This process is described by Fick's second law

$$\frac{\partial C_{Li}}{\partial t} = D\frac{\partial^2 C_{Li}}{\partial x^2} \tag{3-1}$$

where *x* is the distance into the solid from the electrolyte/electrode interface, C_{Li} is the local concentration and D is the chemical diffusion coefficient. The initial and boundary conditions for potentiostatic experiments are:

$$C_{Li} = C_0 \; 0 \le x \le L, t = 0 \tag{3-2}$$

$$C_{Li} = C_s \; x = 0, t > 0 \tag{3-3}$$

$$\frac{\partial C_{Li}}{\partial x} = 0 \; x = L, t \ge 0 \tag{3-4}$$

where C_s is the concentration at the electrode electrolyte interface and C_0 is the uniform concentration in the bulk electrode. Based on the boundary conditions the active Li^+ species can only enter the solid at *x*=0 and a phase boundary exists at *x*=*L*. The time dependent electric current *I(t)* is related to the concentration gradient at the electrode electrolyte interface by

$$I(t) = -z\boldsymbol{F}SD\left(\frac{\partial C_{Li}}{\partial x}\right)_{x=0} \tag{3-5}$$

where *S* is the cross-sectional area of the electrode. The expression of current as a function of time is found to be

$I(t) = z_{Li}\boldsymbol{F}S(C_s - C_0)(\frac{D}{\pi t})^{1/2}$ if $t<<L^2/D$ (3-6)

and

$I(t) = \frac{2z_{Li}\boldsymbol{F}S(C_s - C_0)D}{L}\exp(-\frac{\pi^2 Dt}{4L^2})$ if $t>>L^2/D$ (3-7)

Using the short time approximation when $t<<L^2/D$, the chemical diffusion coefficient *D* can be determined from the linear plot of I *vs*. $1/\sqrt{t}$ where the current exhibits Cottrellian-like behavior. Equation 3-7 uses the long time approximation when $t>>L^2/D$. Using this approximation the chemical diffusion coefficient is calculated from the slope of the linear plot of ln(*I*) *vs t.* Knowledge of the concentration difference ($C_s - C_0$) is not necessary when calculating the chemical diffusion coefficient. The use of the PITT method to identify the chemical diffusion coefficient avoids the introduction of side reaction such as new phase nucleation.

3.2.7.2 PITT results

Potentiostatic intermittent titration technique experiments were performed to identify the lithium diffusion coefficient associated with the high voltage plateau observed in the first charging cycle of the electrochemical curve (Figure 3-13). Figure 3-18A shows the PITT profile for the stoichiometric hydroxide route $Li[Ni_{1/5}Li_{1/5}Mn_{3/5}]O_2$ sample between 3.85 and 4.40 V. Within this region the current exhibits cottrellian ($1/t^{1/2}$) dependence. This is indicative of a solid-solution insertion reaction. [98] The PITT profile between 4.45 and 4.63 V, in Figure 3-18B, shows a change in behavior consistent with the plateau region observed in the electrochemical curve. Within this region, the current decays very quickly then takes a long time to reach the limit value. If we wait for the current to reach the limit value 10μA (takes more than 96hours), the current strays from logarithmic decay and behaves erratically in the range of 4.50 to 4.60 V. Therefore we chose this set of data where the linearity of ln(*I*) vs.*t* is good enough for the analysis shown below. A semi-logarithmic plot of the current versus time was extracted based on the long time dependence $\tau \gg L^2\tilde{D}_{Li}$. The Li diffusion can be solved using Fick's law for a semi-infinite system with a perturbation of the surface concentration in Equation 3-7. [99, 100]

The lithium chemical diffusion coefficient was obtained from the slope of the ln(*I)* versus *t* in Equation 3-8.

$$\tilde{D} = -\frac{\mathrm{d}\ln(I)}{\mathrm{d}t}\frac{4L^2}{\pi^2} \qquad (3\text{-}8)$$

Figure 3-18C plots the lithium chemical diffusion coefficient, $\tilde{D}_{Li}$, versus the state of charge. The values range from 5.6x10^{-14} to 2.5x10^{-13} cm^2s^{-1} between 3.85 V to 4.80 V. Starting at 4.45 V, the lithium chemical diffusion coefficient begins to rapidly decrease until 4.60 V. The PITT results obtained for stoichiometric x=1/4 and 1/3 samples show similar trends.

3.3 Discussion

3.3.1 Effect Of Precursor Composition

Based on our results, it is optimal to synthesize the $Li[Ni_xLi_{1/3-2x/3}Mn_{2/3-x/3}]O_2$ material using a carbonate based precursor during the coprecipitation step. The XRD refinement and TEM results did not show significant changes in the surface and the bulk of either sample. Both synthesis techniques show excellent crystallinity at the surface and similar atomic arrangements with little Li/Ni interlayer mixing. The major source of changes originated from the particle morphology. The particle morphology is significantly altered from random particle shapes and sizes to uniform spherical agglomerated particles with 1-5 µm diameters when using the carbonate route synthesis. These spherical particles are highly porous that have primary particles with 100-300 nm dimensions. The primary particles of both synthesis routes are approximately the same size.

The results show that the rate capabilities of the carbonate based materials are superior to that of the hydroxide route synthesis. Previous research has shown that often during the hydroxide coprecipitation stem, Mn^{2+} is oxidized to Mn^{3+} or Mn^{4+} in aqueous solutions.[101] This result can be evidenced through some indication of Mn^{3+} in the XPS patterns. This result alters the electrochemical performance by creating unstable octahedral and perhaps introducing some Jahn-Teller distortions. The carbonate base coprecipitation method results in uniform spherical particles. The larger uniformly sized particles show less reactivity at highly oxidized states as well as show increased tap-densities.[102, 103] Both of these properties are desirable for optimal electrochemical performance including increased energy density.

3.3.2 Effect Of LiOH In The Coprecipitation Precursor

The results obtained from XRD refinement, XPS, SEM, TEM and electrochemical testing show that the electrochemical properties of $Li[Ni_xLi_{1/3-2x/3}Mn_{2/3-x/3}]O_2$ are significantly influenced by synthesis conditions, particularly the amount of LiOH in the precursor. During the coprecipitation, an excess amount of $LiOH{\cdot}H_2O$ solution was used to ensure complete precipitation of the transition metal (TM) double hydroxide, $(Ni_xMn_{2/3-x/3})(OH_2)$. In principle, all excess LiOH will be washed away with deionized water as shown in the experimental section. Nevertheless, several major differences are observed compared to the stoichiometric samples:

The ICP-OES data (Table 3-1) shows a significant amount of excess Li (5-10%) deviation from the designated lithium concentration in the materials. The XRD refinement shows little evidence of the excess Li in terms of structural characteristics (Table 3-2).

The XRD results indicate that a pure layered phase can be obtained at 900°C and 1000°C by furnace cooling or quenching with excess LiOH. However, phase separation is seen if the stoichiometric Ni1/5 sample is synthesized at 900°C without quenching (Figure 3-4).

The average particle size of LiOH excess materials is larger than that of the stoichiometric materials.

The LiOH excess materials exhibit consistently inferior electrochemical properties compared with stoichiometric samples. A stable capacity less than 200 mAh/g is usually obtained when cycled at C/50 between 2.0-4.8 V. The capacity drops to about 150 mAh/g when the rate is increased to C/20.

After electrochemical cycling, the stoichiometric Ni1/5 sample retains the $R\bar{3}m$ parent layer structure, while the LiOH excess sample has significant structural changes, indicated by the disappearance of (006) peak intensity and increasing peak intensity of (104) and (110).

Our high-resolution TEM, EELS and XPS studies reveal that the difference lies in the surface layer characteristics that are most probably caused by the presence of excess LiOH during coprecipitation. The excess LiOH might have led to the formation of a Nickel-rich compound with increased Ni^{3+} concentration at the surface of the particles due to the increased alkalinity in the precipitating solution. Subsequent washing and high temperature synthesis cannot completely remove the surface layer, which resulted in larger polarization and more irreversible first cycle capacity due to side reaction with the electrolyte. It has been shown by previous work that intentional surface modifications of $xLi_2MnO_3\cdot(1-x)LiMO_2$ (M=Mn, Ni and/or Co) can significantly improve the electrochemical performance compared to bare-surface materials. [35, 38, 104, 105] The stoichiometric materials had well defined clean crystalline surfaces as shown in Figure 3-8A, while the LiOH excess materials showed different surface characteristics from the bulk, seen in Figure 3-8B. EELS data reveals that the local environments of oxygen are identical at the surface and in the bulk for stochiometric sample, and different for LiOH excess sample. This distinct surface layer in LiOH excess material is believed to be the contributing factor for the observed secondary plateau around 4.60-4.70 V and the inferior reversible capacity.

3.3.3 Effect Of Synthesis Temperature And Cooling Rate

Based on our results, it is optimal to synthesize the $Li[Ni_xLi_{1/3-2x/3}Mn_{2/3-x/3}]O_2$ material with a stoichiometric amount of LiOH precursor during the coprecipitation step, fire at 1000°C and allow the sample to furnace cool. Previous work by Lu et al. determined that increasing sintering temperature improved the layered structure as well as the electrochemical performance of $Li[Ni_xLi_{1/3-2x/3}Mn_{2/3-x/3}]O_2$ ($0 \leq x \leq 0.5$). [91] The XRD patterns (Figure 3-3) of the samples sintered at 1000°C have increased superlattice peak intensity as well as decreased amounts of Li/Ni 3a site mixing compared to that sintered at 900°C, indicating improved cation ordering for samples made at high temperature. The electrochemical performance of the material sintered at 1000°C shows consistently better reversible capacity compared to that synthesized at 900°C.

Samples sintered at 1000°C show increased *c* and *a* lattice parameters, and less Li/Ni interlayer mixing. The lattice expansion and improved cation ordering may improve Li mobility leading to the improved electrochemical performance.

For samples synthesized at 1000˚C, cooling rate plays a role in the electrochemical performance. Opposite as what is previously observed in $LiNi_{1/2}Mn_{1/2}O_2$ [10], quenching leads to higher first cycle irreversible capacity and less discharge capacity in lithium-excess layered oxides. The furnace cooled sample shows less first cycle irreversible capacity and better reversible discharge capacity exceeding 250 mAh/g. This could be attributed to the fact that the furnace cooled sample exhibits improved layeredness, less Li/Ni mixing and better crystallinity at the surface.

3.3.4 Effect Of Cation Migration On Lithium Chemical Diffusivity

Rietveld refinement of the XRD patterns following electrochemical cycling indicates that although the stoichiometric material remains layered after electrochemical cycling between 2.0-4.8 V, significant cation re-arrangement has occurred. The major changes in the XRD patterns of the cycled stoichiometric samples are the disappearance of the superlattice peaks and expanding *c* and *a* lattice parameters. Previous experiments that examined the structure of $Li[Ni_{1/3}Li_{1/9}Mn_{5/9}]O_2$ (x=1/3) following one, five and ten cycles reported similar trends and concluded the transition metal ordering disappears following ten cycles; in addition, a second phase following the first cycle was observed with synchrotron XRD. [95] The disappearance of the superlattice peaks is consistent with this work and our preliminary synchrotron data also suggests the formation of a second phase. The details will be reported in a separate publication. The Ni content in Li layers decreased after the first cycle, and increased to a higher value after 10 cycles. Such trend is somewhat consistent with work by Jiang *et* *al.* on Ni1/3 material. It suggests that not only the Li ions but also the transition metal ions are dynamically moving during electrochemical charging/discharging process. The exact mechanisms of such cation migration is unclear at the moment, however, our PITT data (Figure.3-14C) clearly show that the lithium chemical diffusion coefficient drops significantly in the voltage range 4.45 to 4.65 V. We believe that this is the voltage range where transition metal ion migration occurs and impedes the lithium ion transport.

The relations between synthesis conditions, detailed crystal structures and electrochemical properties of lithium-excess layered oxides have been studied. The data provides evidence that optimal synthesis conditions of the lithium-excess layered oxide $Li[Ni_xLi_{1/3-2x/3}Mn_{2/3-x/3}]O_2$ ($0 \leq x \leq 1/2$) are obtained for stoichiometric samples sintered at 1000°C in air followed by furnace cooling.

X-ray diffraction data of electrochemically cycled electrode materials show an expanded c/a lattice ratio and changing Li/Ni interlayer mixing indicating peculiar cation migration. Potentiostatic intermittent titration (PITT) measurements indicate a decrease in the Li chemical diffusion coefficient during the initial charging process from 4.45 V to 4.65 V suggesting that during this region not only the Li ions but the transition metal ions are dynamically migrating during electrochemical processes.

Samples synthesized with stoichiometric and excess amounts of LiOH show obvious differences in surface characteristics. The electrochemical results obtained from these materials favor the well defined clean crystalline surfaces of the stoichiometric materials. Results indicated the formation of a compound with increased Ni^{3+} concentrations accumulated at the surface of the LiOH excess particles due to the increased alkalinity in the precipitating solution.

Our data illustrates that the synthetic history of these lithium-excess materials imposes a serious fingerprint in the electrochemical behavior. The first cycle irreversible capacity is affected by the both the bulk and surface characteristics of the pristine materials, which is strongly influenced by precursor chemistry. Efforts to improve the performance of layered $LiMO_2$ cathode materials involve a deep understanding of the connection between crystal structure and electrochemical properties.

Table 3-1. Li/[Mn + Ni] and Mn:Ni ratios of pristine $Li[Ni_xLi_{1/3-2x/3}Mn_{2/3-x/3}]O_2$ materials where x= 1/5, 1/4 and 1/3 with excess amounts of LiOH from ICP-OES

Sample	Ni:Mn Ratio Experimental (ICP-OES)	Theoretical	Li:(Ni+Mn) Experimental (ICP-OES)	Theoretical
Ni1/3	1.59	1.66	1.30	1.25
Ni1/4	2.27	2.33	1.56	1.40
Ni1/5	2.89	3.00	1.62	1.50

Table 3-2. Li/[Mn + Ni] and Mn:Ni ratios of pristine $Li[Ni_xLi_{1/3-2x/3}Mn_{2/3-x/3}]O_2$ materials where x= 1/5, 1/4 and 1/3 with stoichiometric amounts of LiOH from ICP-OES

Sample	Ni:Mn Ratio Experimental (ICP-OES)	Theoretical	Li:(Ni+Mn) Experimental (ICP-OES)	Theoretical
Ni1/3	1.58	1.66	1.27	1.25
Ni1/4	2.28	2.33	1.43	1.40
Ni1/5	2.85	3.00	1.54	1.50

Table 3-3. Rietveld results of hydroxide and carbonate route pristine $Li[Ni_xLi_{1/3-2x/3}Mn_{2/3-x/3}]O_2$ where x= 1/5, 1/4 and 1/3 synthesized at 1000°C with excess and stoichiometric amounts of LiOH precursor. n_Ni is Ni in Li layer *a* and *c* lattice parameters given in Angstroms (Å)

Sample	Stoichiometric Hydroxide	LiOH Excess Hydroxide	Carbonate
Ni1/3	a=2.8748 ± 0.001 c=14.2988 ±0.005 c/a=4.974 z(O)=0.2528±0.0004 n_Ni=0.081±0.002 R_{wp}=1.53% R_B=15.5%	a=2.8766 ± 0.001 c=14.2995 ±0.006 c/a=4.971 z(O)=0.2545±0.0004 n_Ni =0.063±0.002 R_{wp}=1.78% R_B=13.8%	
Ni1/4	a=2.8667 ± 0.001 c=14.2772 ±0.005 c/a=4.98 z(O)=0.258±0.0004 n_Ni=0.039±0.002 R_{wp}=14.5% R_B=7.6%	a=2.8699 ± 0.001 c=14.2967 ±0.005 c/a=4.982 z(O)=0.2548±0.0004 n_Ni =0.045±0.002 R_{wp}=1.71% R_B=15.3%	
Ni1/5	a=2.8618 ± 0.001 c=14.2598 ±0.005 c/a=4.986 z(O)=0.2528±0.0004 n_Ni=0.081±0.002 R_{wp}=14.5% R_B=8.94%	a=2.8664 ± 0.001 c=14.2927 ±0.005 c/a=4.986 z(O)=0.2559±0.0004 n_Ni =0.028±0.002 R_{wp}=1.75% R_B=16.5%	a=2.8608 ± 0.001 c=14.2584 ±0.005 c/a=4.984 z(O)=0.257±0.0004 n_Ni (in Li layer)=0.033±0.002 R_{wp}=11.2% R_B=6.4%

Table 3-4. Rietveld fitting results of stoichiometric hydroxide route pristine $Li[Ni_xLi_{1/3-2x/3}Mn_{2/3-x/3}]O_2$ where x= 1/5, synthesized at 900°C and 1000°C with different cooling rates. *a* and *c* lattice parameters given in Angstroms (Å)

Sample	Rietveld Results
900C Quenched (b)	a=2.8664± 0.001 c=14.2806 ± 0.005 c/a=4.982 z(O)=.2545± 0.0004 n_Ni (in Li layer)=.068 ± 0.002 R_{wp}= 1.74% R_B= 18.7%
1000C Furnace Cooled (c)	a= 2.8668 ± 0.001 c= 14.2873 ± 0.006 c/a=4.984 z(O)= 0.2531 ± 0.0004 n_Ni (in Li layer)= 0.041 ± 0.003 R_{wp}=1.73% R_B=15.4%
1000C Quenched (d)	a=2.8689± 0.001 c=14.2938 ± 0.005 c/a=4.982 z(O)=.2538± 0.0004 n_Ni (in Li layer)=.053 ± 0.002 R_{wp}= 1.53% R_B= 18.4%

Table 3-5. Rietveld fitting results of LiOH excess hydroxide route pristine $Li[Ni_xLi_{1/3-2x/3}Mn_{2/3-x/3}]O_2$ where x= 1/5, synthesized at 900°C and 1000°C with different cooling rates. *a* and *c* lattice parameters given in Angstroms (Å)

Sample	Rietveld Results
900C Furnace Cooled (b)	a=2.8668± 0.001 c=14.2799 ± 0.005 c/a=4.981 z(O)=.2557± 0.0004 n_Ni (in Li layer)=.034 ± 0.002 R_{wp}= 1.84% R_B= 17.1%
1000C Furnace Cooled (c)	a= 2.8605 ± 0.001 c= 14.2726 ± 0.006 c/a=4.990 z(O)= 0.2562 ± 0.0004 n_Ni (in Li layer)= 0.030 ± 0.003 R_{wp}=1.73% R_B=15.4%
1000C Quenched (d)	a=2.8649± 0.001 c=14.2824 ± 0.005 c/a=4.985 z(O)=.2551± 0.0004 n_Ni (in Li layer)=0.042 ± 0.002 R_{wp}= 1.82% R_B= 17.1%

Table 3-6. Comparision of Rietveld fitting result for stoichiometric and LiOH excess hydroxide route and carbonate route $Li[Ni_xLi_{1/3-2x/3}Mn_{2/3-x/3}]O_2$ where x= 1/5 samples following 10 electrochemical cycles. *a* and *c* lattice parameters given in Angstroms (Å)

	Stoichiometric Hydroxide	LiOH Excess	Carbonate
Pristine	a= 2.8668 ± 0.001	a= 2.8664 ± 0.001	a= 2.8766
	c= 14.2873 ± 0.006	c= 14.2927 ± 0.006	c= 14.3164 ± 0.006
	c/a=4.984	c/a=4.986	c/a=4.977
	z(O)= 0.253 ± 0.0004	z(O)= 0.2559 ± 0.0003	z(O)= 0.254 ± 0.0003
	n_Ni (in Li layer)= 0.041	n_Ni (in Li layer)= 0.028	n_Ni (in Li layer)= 0.047
	R_{wp} =1.73% R_B =15.4%	Rwp=1.75% R_B =16.5%	R_{wp}=1.08% R_B =12.8%
10 Cycles	a= 2.8873 ± 0.002	a=2.8736 ± 0.001	a=2.8990 ± 0.001
	c= 14.4073 ± 0.011	c=14.3807 ± 0.006	c=14.4149 ± 0.005
	c/a=4.990	c/a=5.005	c/a=4.972
	z(O)= 0.2526 ± 0.0004	z(O) = 0.260 ± 0.0005	z(O) = 0.260 ± 0.0005
	n_Ni (in Li layer)= 0.069	n_Ni (in Li layer) = 0.040	n_Ni (in Li layer) = 0.043
	R_{wp} =1.61% R_B =15.0%	R_{wp} = 1.54% R_B =16.7%	R_{wp} = 1.65% R_B=11.5%

Table 3-7. XPS binding energies for Mn $2p_{3/2}$, Ni $2p_{3/2}$ and O 1s for as-synthesized samples of stoichiometric and LiOH excess $Li[Ni_{1/5}Li_{1/5}Mn_{3/5}]O_2$**.**

Material	Mn $2p_{3/2}$ Binding Energy	Ni $2p_{3/2}$ Binding Energy	O 1s Binding Energy
$Li[Ni_{1/5}Li_{1/5}Mn_{3/5}]O_2$	642.45 eV	854.72 eV (Ni^{2+})	531.73 eV
Stoichiometric		855.48 eV (Ni^{3+})	529.90 eV
$Li[Ni_{1/5}Li_{1/5}Mn_{3/5}]O_2$	642.29 eV	854.51 eV (Ni^{2+})	531.91 eV
LiOH excess		855.75 eV (Ni^{3+})	529.68 eV

Table 3-8. Comparison of the theoretical capacities of $Li[Ni_xLi_{1/3-2x/3}Mn_{2/3-x/3}]O_2$ based on the Ni^{2+}/Ni^{4+} redox couple and full Li extraction versus the observed first cycle discharge capacity.

Material	Nickel Redox Capacity	Theoretical Li Capacity	First Cycle Actual Discharge Capacity
$Li[Ni_{1/5}Li_{1/5}Mn_{3/5}]O_2$ X=1/5	126mAh/g	378 mAh/g	255 mAh/g
$Li[Ni_{1/4}Li_{2/12}Mn_{7/12}]O_2$ X=1/4	154mAh/g	360 mAh/g	237 mAh/g
$Li[Ni_{1/3}Li_{1/9}Mn_{5/9}]O_2$ X=1/3	199mAh/g	331 mAh/g	197 mAh/g

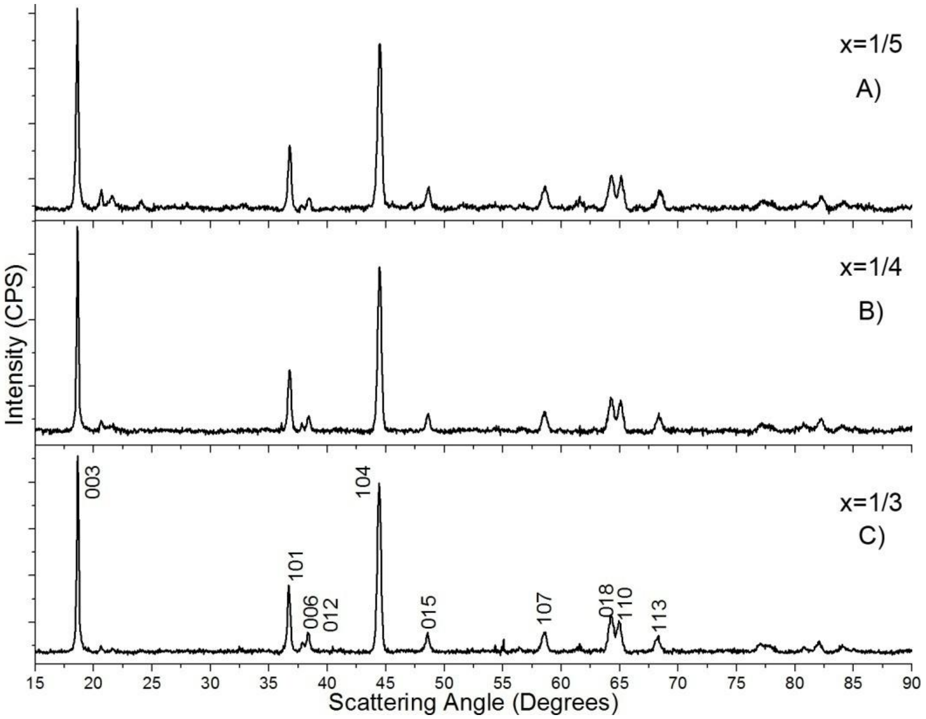

Figure 3-1. X-ray diffraction patterns of hydroxide route $Li[Ni_xLi_{1/3-2x/3}Mn_{2/3-x/3}]O_2$ synthesized with an excess amount of LiOH precursor at 1000°C with furnace cooling to room temperature where x= A) 1/5, B) 1/4 and C) 1/3.

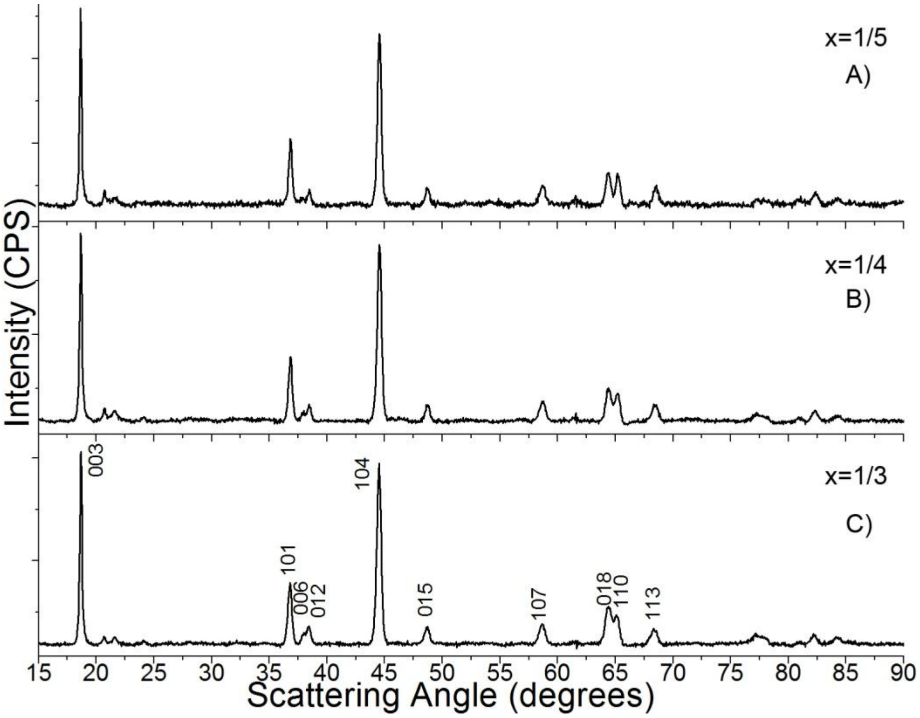

Figure 3-2. X-ray diffraction patterns of hydroxide route $Li[Ni_xLi_{1/3-2x/3}Mn_{2/3-x/3}]O_2$ synthesized with a stoichiometric amount of LiOH precursor at 1000°C with furnace cooling to room temperature where x= A) 1/5, B) 1/4 and C) 1/3

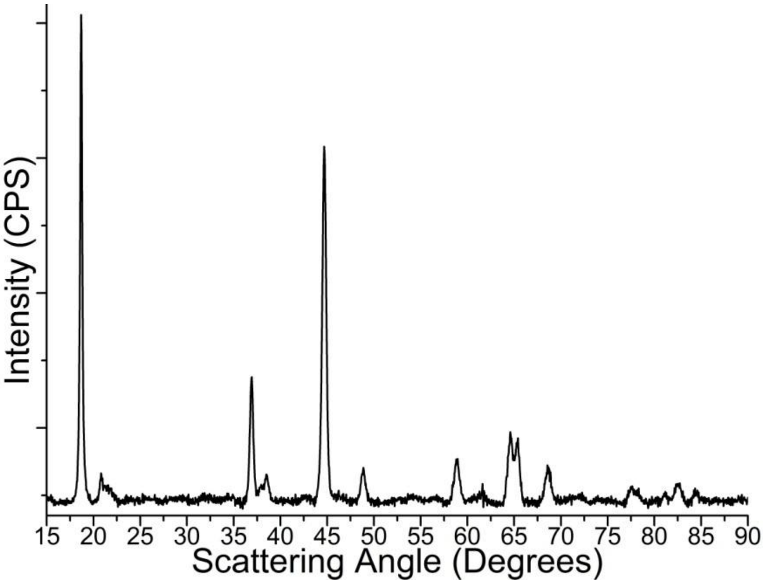

Figure 3-3. X-ray diffraction patterns of carbonate route $Li[Ni_xLi_{1/3-2x/3}Mn_{2/3-x/3}]O_2$ where x=1/5.

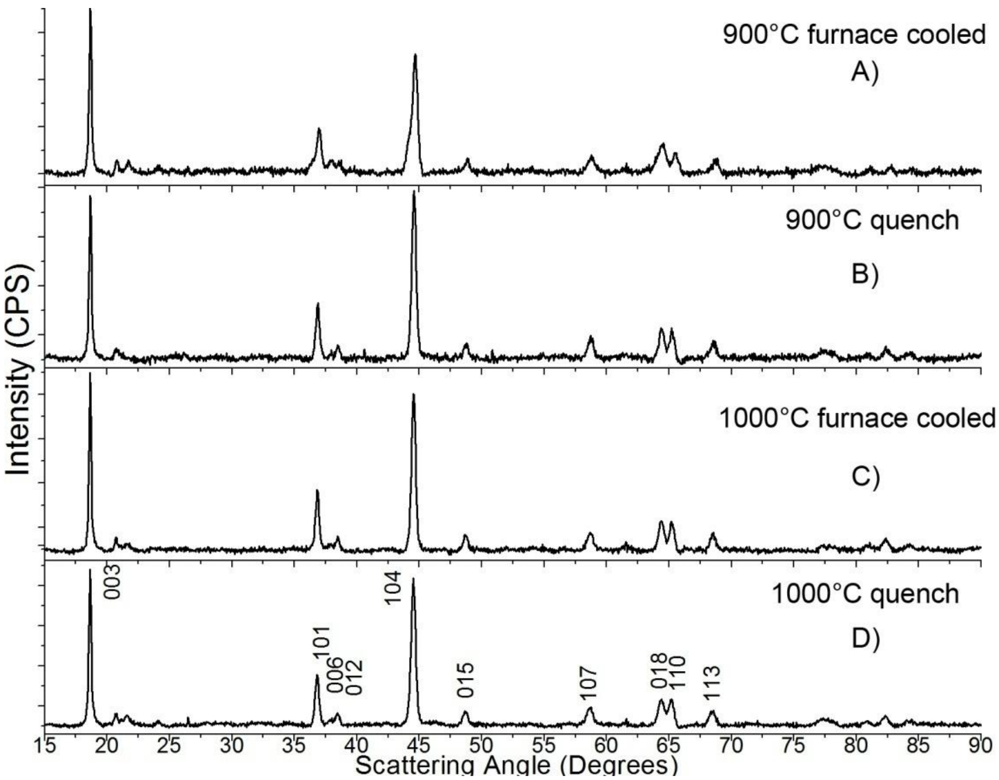

Figure 3-4. Comparison of XRD patterns of pristine $Li[Ni_{1/5}Li_{1/5}Mn_{3/5}]O_2$ with a stoichiometric amount of LiOH precursor synthesized at A) and B) 900°C or C) and D) 1000°C

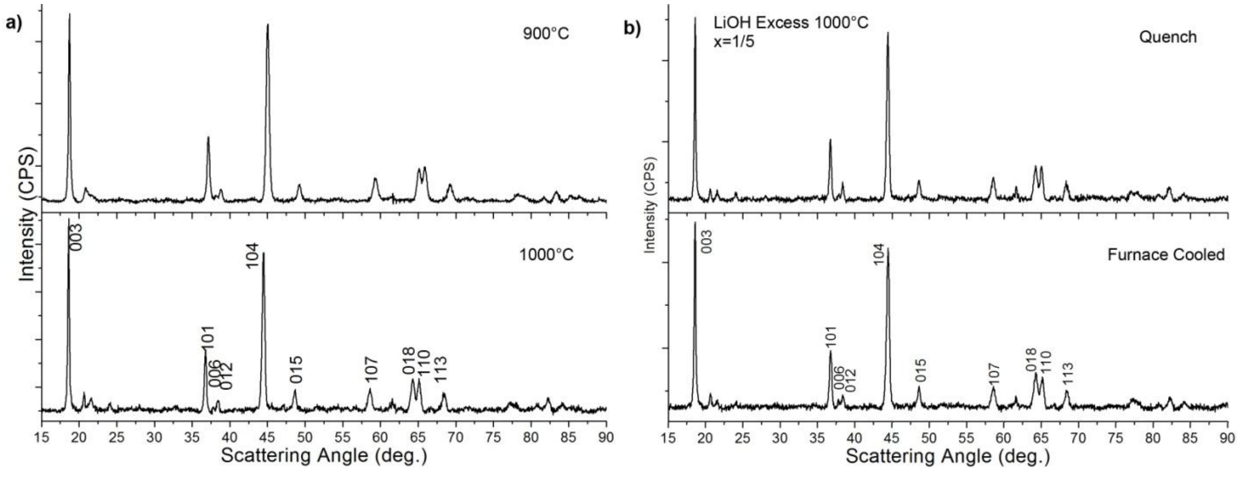

Figure 3-5. Comparison of XRD patterns of the LiOH excess $Li[Ni_xLi_{1/3-2x/3}Mn_{2/3-x/3}]O_2$ where x=1/5 synthesized at A) 900°C or 1000°C and B) furnace cooled or quenched between stainless steel plates to room temperature.

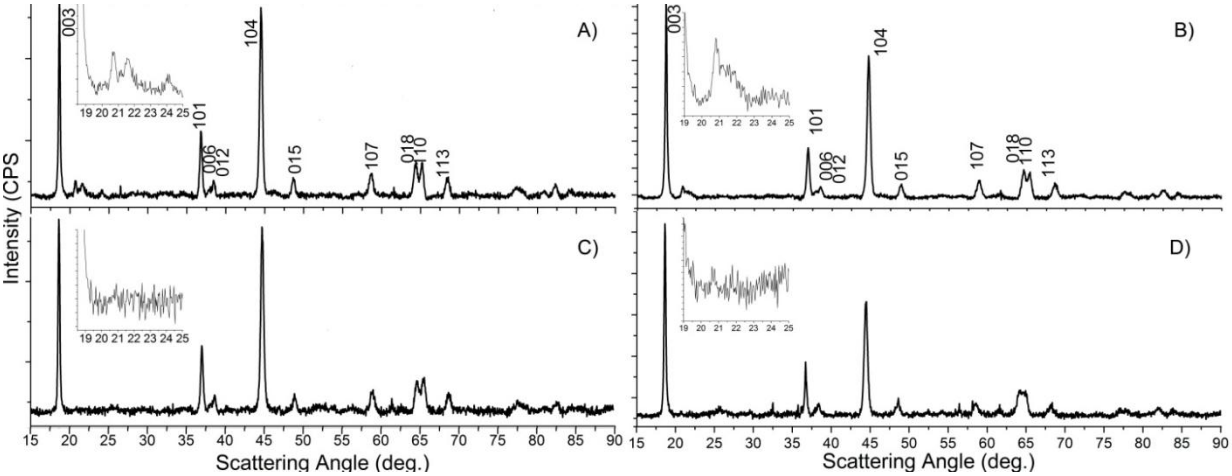

Figure 3-6. XRD patterns of comparing Li[$Ni_xLi_{1/3-2x/3}Mn_{2/3-x/3}$]$O_2$ where x=1/5 synthesized at 1000°C using A) the pristine hydroxide route and C) following 10 electrochemical cycles and of the B) pristine carbonate route and D) following 10 electrochemical cycles

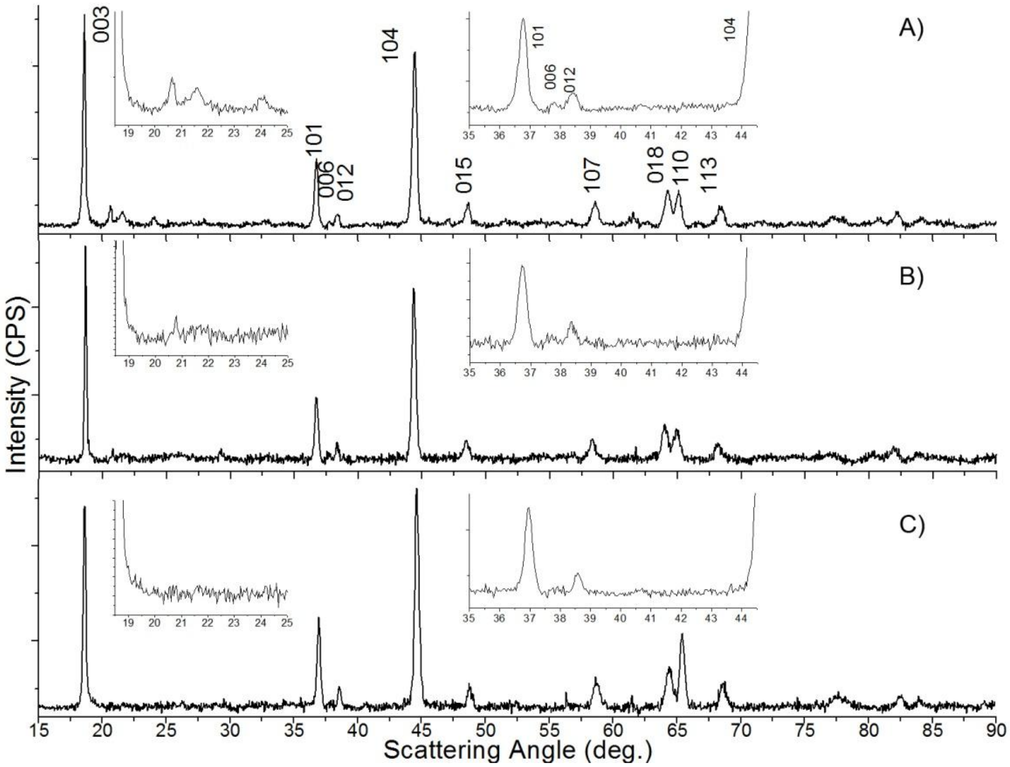

Figure 3-7. Comparison of the XRD patterns of LiOH excess where x=1/5 synthesized at 1000°C showing the A) Pristine, B) following 1 electrochemical cycle and C) following 10 electrochemical cycles

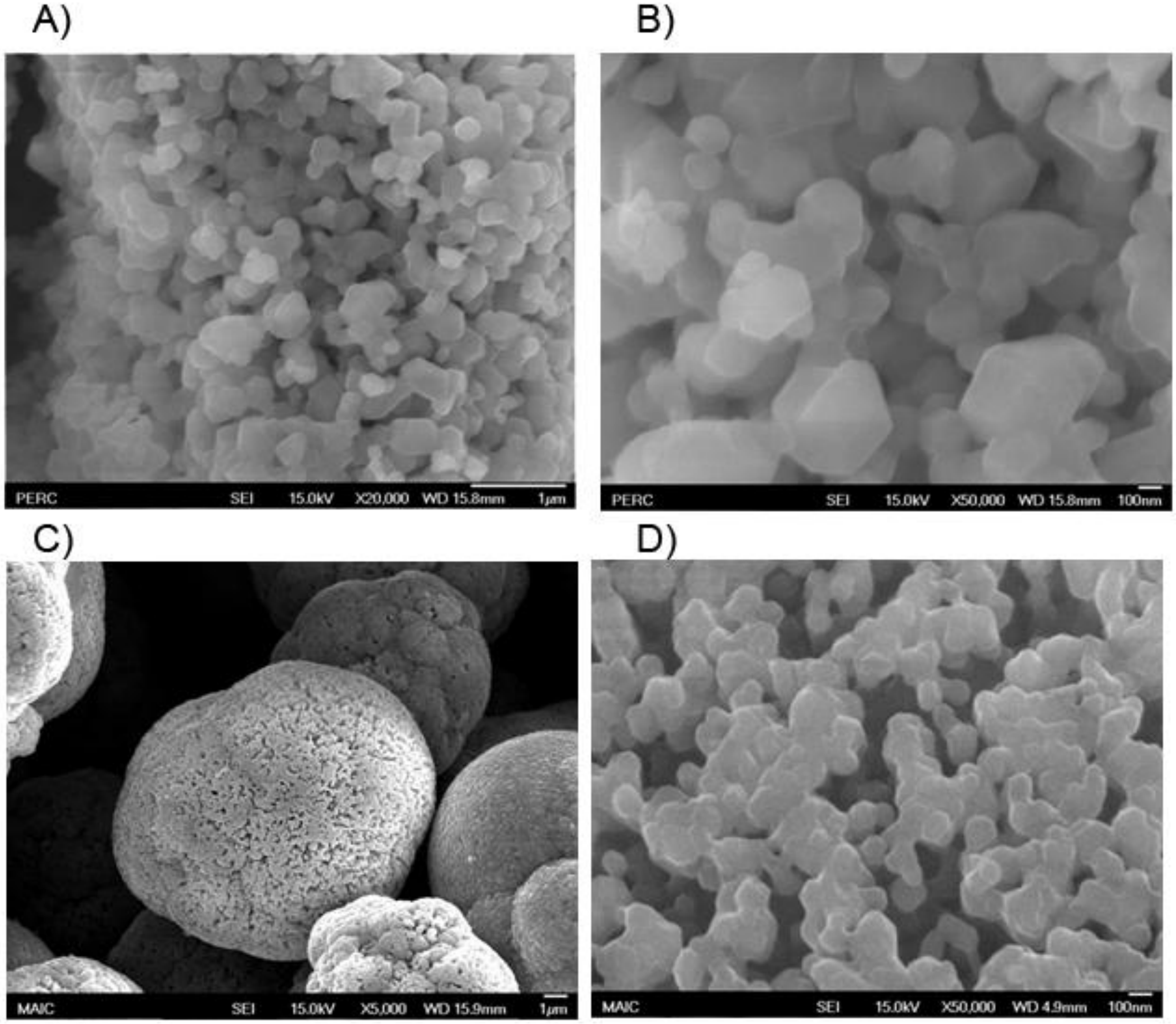

Figure 3-8. SEM pictures of sintered $Li[Ni_{1/5}Li_{1/5}Mn_{3/5}]O_2$ powders synthesized using the A) and B) hydroxide route and C) and D) carbonate route.

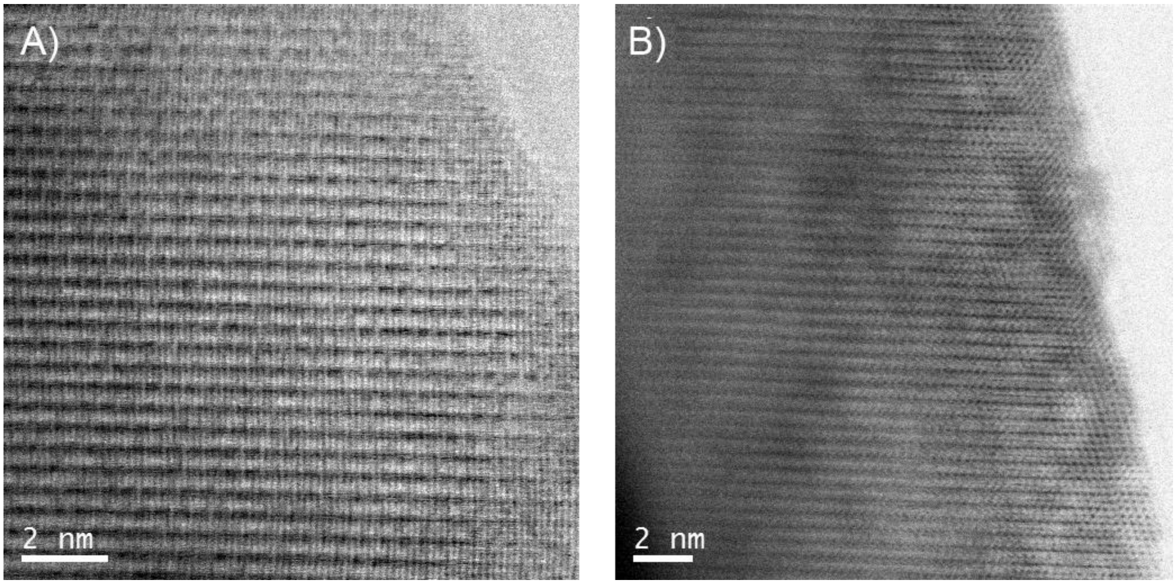

Figure 3-9. TEM images of $Li[Ni_{1/5}Li_{1/5}Mn_{3/5}]O_2$ using A) stoichiometric and B)LiOH excess synthesis at 1000°C with furnace cooling.

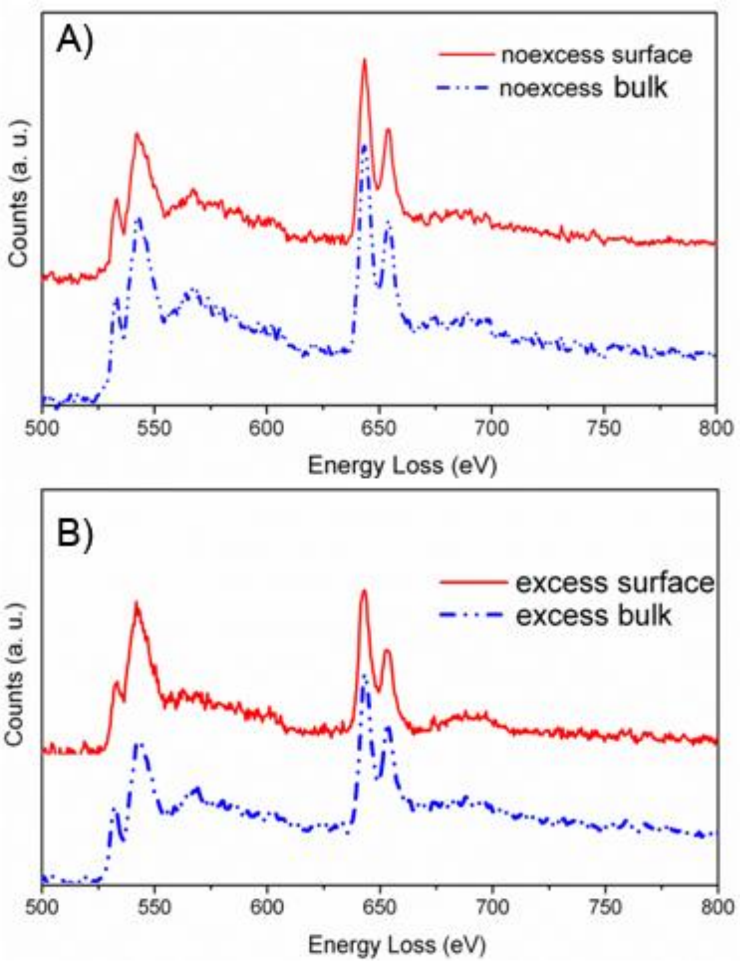

Figure 3-10. EELS spectra of hydroxide route Li[$Ni_{1/5}Li_{1/5}Mn_{3/5}$]O_2 synthesized at 1000°C with furnace cooling using A) stoichiometric and B)LiOH excess.

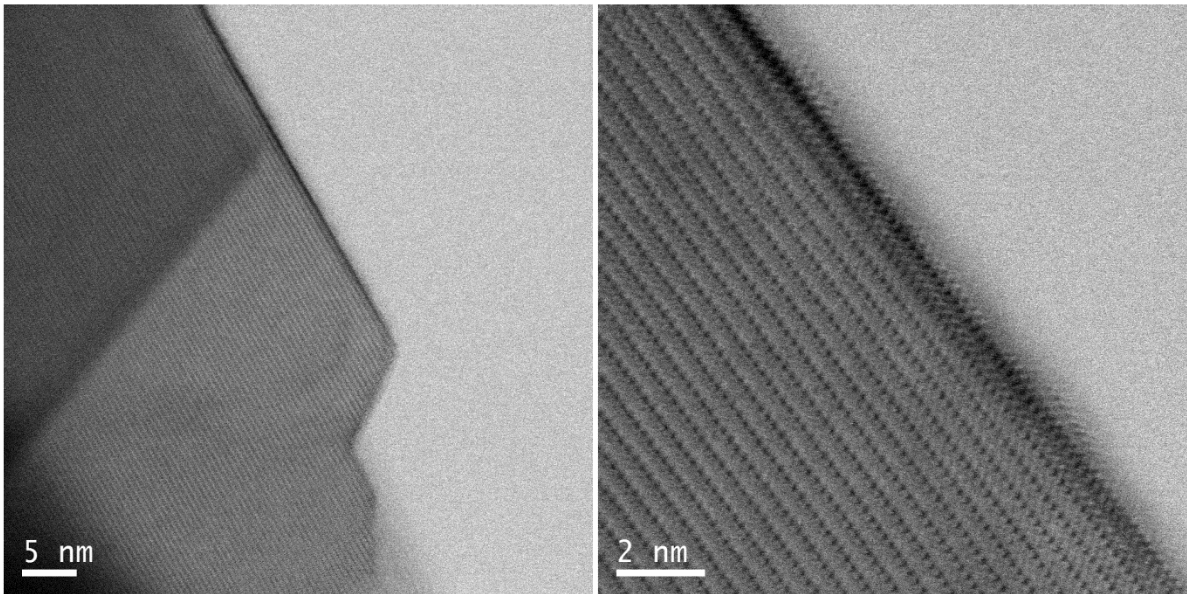

Figure 3-11. TEM images of the carbonate route Li[$Ni_{1/5}Li_{1/5}Mn_{3/5}$]O_2 synthesized at 1000°C with furnace cooling.

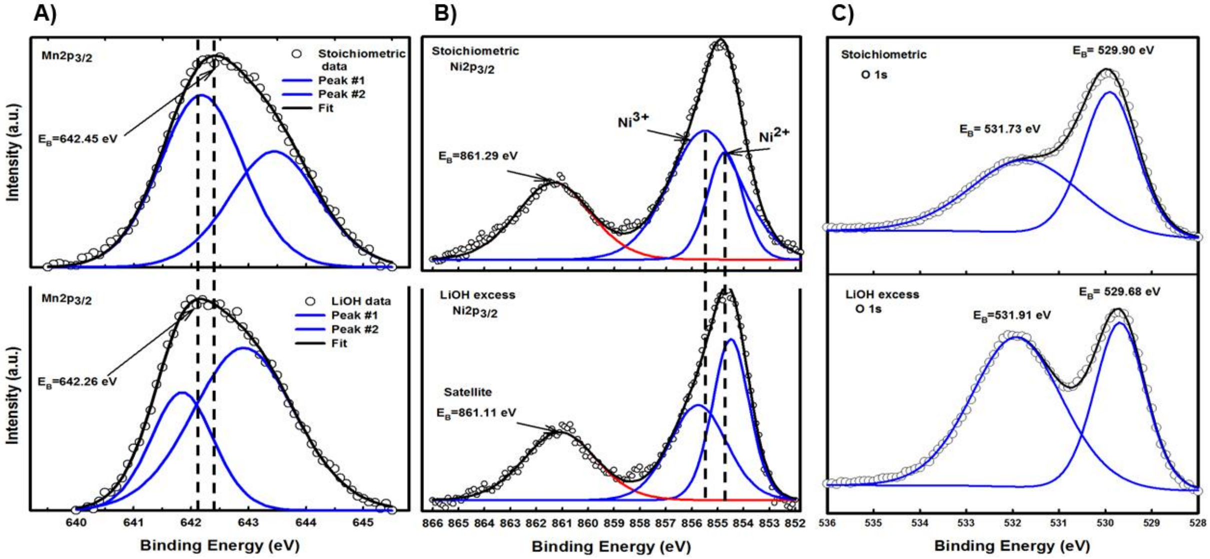

Figure 3-12. X-ray photoelectron spectroscopy data from stoichiometric and LiOH excess samples of Li[$Ni_xLi_{1/3-2x/3}Mn_{2/3-x/3}$]$O_2$ where x=1/5 showing A) the Mn $2p_{3/2}$ spectrum, B) the Ni $2p_{3/2}$ spectrum and C) the O 1s spectrum.

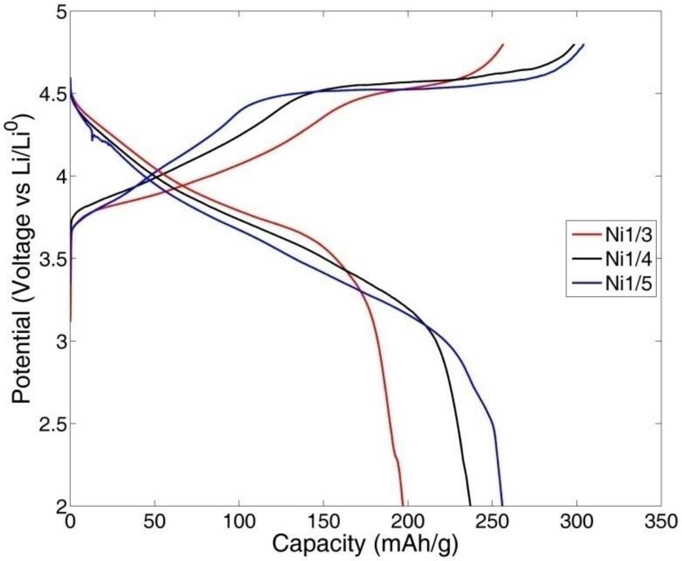

Figure 3-13. Electrochemical profiles of hydroxide route $Li[Ni_xLi_{1/3-2x/3}Mn_{2/3-x/3}]O_2$ where x=1/5, 1/4 and 1/3 synthesized at 1000°C with a C/50 rate (0.016mA/cm^2). Voltage windows of 4.8-2.0 V were used.

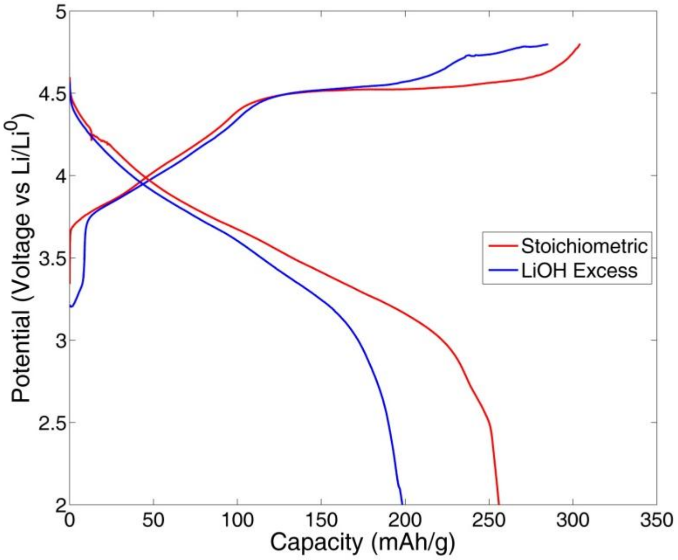

Figure 3-14. Comparison of the electrochemical profiles of hydroxide route $Li[Ni_{1/5}Li_{1/5}Mn_{3/5}]O_2$ for stoichiometric and excess LiOH samples synthesized at 1000°C with furnace cooling to room temperature. Voltage windows of 4.8-2.0 V were used.

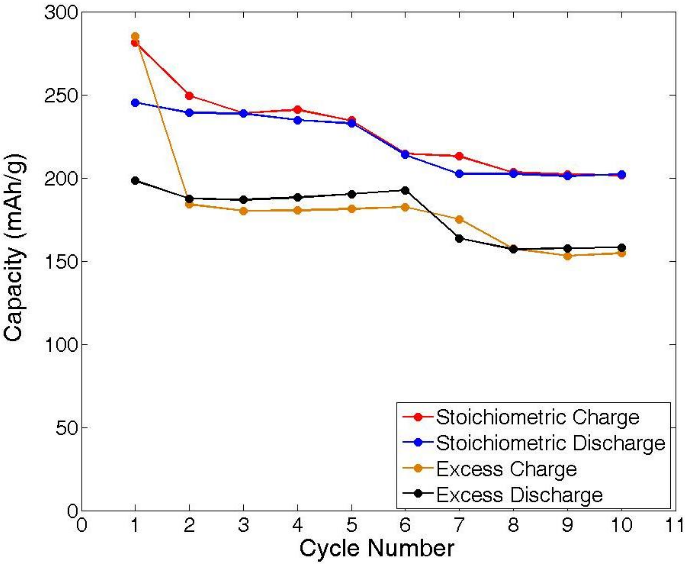

Figure 3-15. Comparison of the cyclability of hydroxide route Li[$Ni_{1/5}Li_{1/5}Mn_{3/5}$]O_2 with stoichiometric and excess amounts of LiOH. The first 5 cycles correspond to a C/50 rate (0.016mA/cm^2) and cycles 6-10 correspond to a C/20 rate (0.04mA/cm^2).

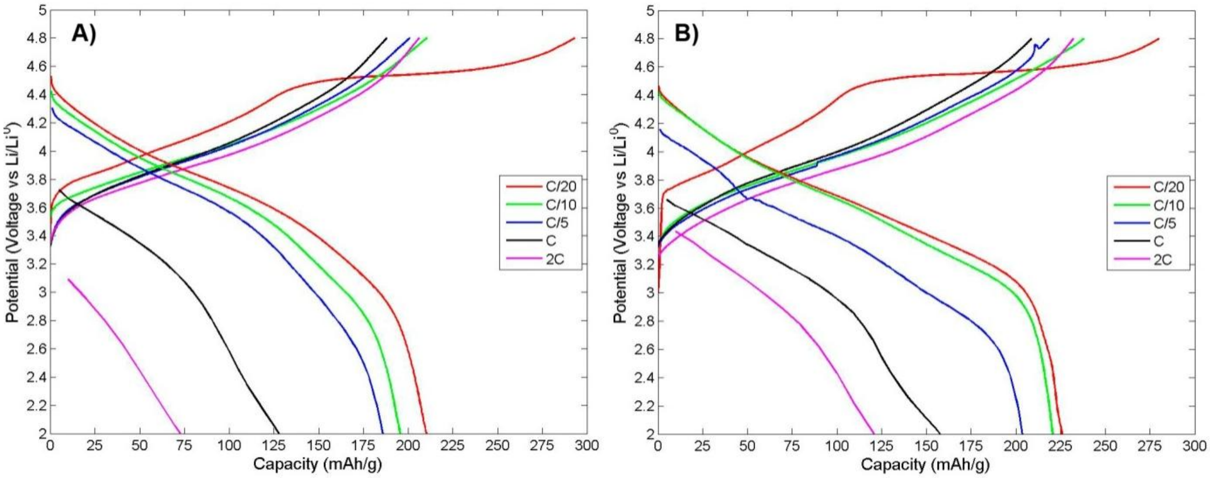

Figure 3-16. Rate capability of Li[$Ni_{1/5}Li_{1/5}Mn_{3/5}$]O_2 comparing A) the hydroxide route with stoichiometric LiOH and B) the carbonate synthesis methods

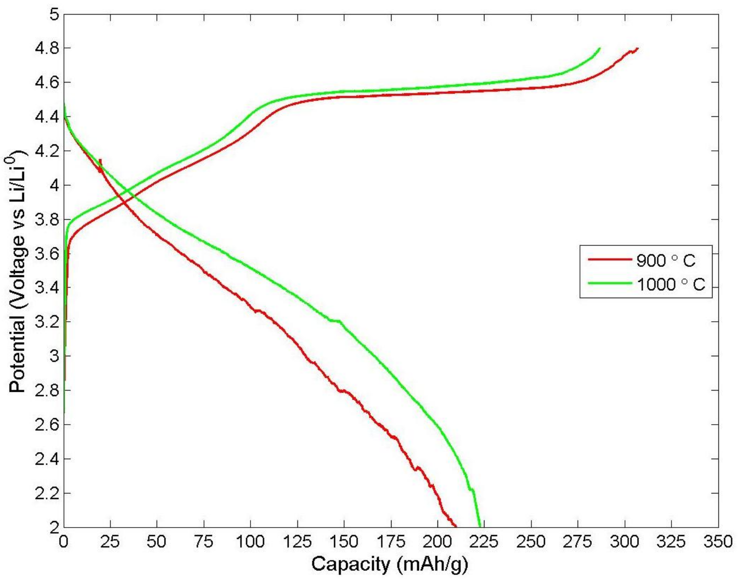

Figure 3-17. Comparison of the electrochemical profiles of hydroxide route $Li[Ni_{1/5}Li_{1/5}Mn_{3/5}]O_2$ for samples with stoichiometric amounts of LiOH synthesized at 900°C and 1000°C.

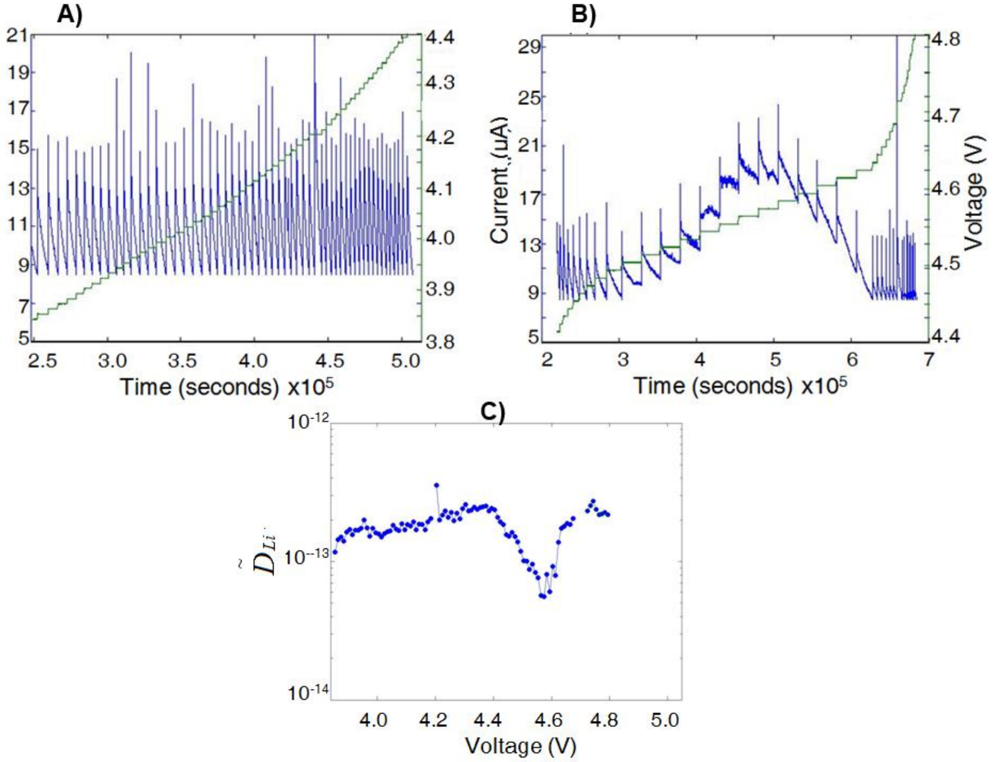

Figure 3-18. Potentiostatic intermittent titration technique (PITT) for hydroxide route $Li[Ni_{1/5}Li_{1/5}Mn_{3/5}]O_2$ with voltage windows A) 3.85−4.40 V and B) 4.40−4.80 V for the first charge cycle. C) Plot of the calculated Li chemical diffusion coefficient versus voltage on the first charging cycle.

CHAPTER 4
HIGH PRESSURE DRIVEN STRUCTURAL AND ELECTROCHEMICAL MODIFICATIONS IN LAYERED LITHIUM TRANSITION METAL INTERCALATION OXIDES

This chapter is part of the paper: “High Pressure Driven Structural and Electrochemical Modifications in Layered Lithium Transition Metal Intercalation Oxides” by Christopher R. Fell, D.H. Lee, J.M. Gallardo-Amores, E. Moran, M.E. Arroyo-de Dompablo and Ying Shirley Meng.; Energy and Environmental Sciences, 2012 (http://dx.doi.org/10.1039/C2EE02818B) *Reproduced by permission of The Royal Society of Chemistry* The high pressure work was highly collaborative with J.M. Gallardo-Amores, E. Moran and M.E. Arroyo-de Dompablo.

The high pressure and high temperature methods are utilized to introduce structural modifications in the layered lithium transition metal oxides $LiCoO_2$ and $Li[Ni_xLi_{1/3-2x/3}Mn_{2/3-x/3}]O_2$ where x=0.25 and 0.5. It is well documented that the synthesis conditions play a critical role to determine the microstructure, morphology and surface characteristics, thereby influencing the electrochemical response of a layered transition metal intercalation oxide. Layered oxide positive electrode materials that can be charged to higher potentials (more than 4 V) with higher specific capacities are possible candidates for onboard energy storage for vehicles. $LiCoO_2$ has been commercialized for two decades. The crystal structure is composed of alternating layers of lithium and cobalt ions in a close packed oxygen array. The lithium ions are reversibly intercalated between the Transition Metal-Oxygen (MO) layers. Replacing Co by Ni and Mn leads to $LiNi_{0.5}Mn_{0.5}O_2$, a typical multi-electron redox system showing a synergetic combination of Mn^{4+} and $Ni^{2+.}$ In this material, Mn^{4+} remains unchanged and stabilizes the structure when Li is extracted. Ni^{2+} can be fully oxidized to Ni^{4+}, thereby compensating the fact that Mn^{4+} cannot be oxidized. [106, 107] This material delivers 200 mAh/g reversible capacity between 3 to 4.5 V. [108] The layered "lithium-excess" transition metal oxides, $Li[Ni_xLi_{1/3-2x/3}Mn_{2/3-x/3}]O_2$ ($0 \leq x \leq 1/2$), are of great interest as a new generation of positive electrode materials since they deliver higher reversible capacity exceeding 250 mAh/g at a lower cost compared with both $LiCoO_2$ and $LiNi_{0.5}Mn_{0.5}O_2$. During the initial charging region, the capacity originates from the oxidation of Ni^{2+} to Ni^{4+} up to 4.4 V. At 4.45 V, a high voltage plateau region appears associated to an irreversible capacity of 50 to 100 mAh/g. The anomalous high capacities have been attributed to an irreversible loss of oxygen from the lattice during the first charge accompanied by Li removal and/or surface reaction through electrode/electrolyte reduction.[20, 29, 109-112] Though a clear explanation of the source of the additional capacity is still under debate, previous work has consistently shown changes in the cation arrangement and crystal structure upon electrochemical cycling to 4.8 V. Previous research has identified the disappearance of the cation ordering in the transition metal layer following electrochemical cycling.[109, 113] Our previous research has also observed the expansion of the *c/a* lattice ratio and increased Li/Ni interlayer mixing following ten electrochemical cycles.[113] Moreover, during electrochemical cycling the material undergoes large changes in lattice parameters as well as increases in strain.[110] However, the material is able to reversibly cycle with large capacities and little capacity fade although undergoing serious structural modifications during the first electrochemical cycle.

Chapter 3 detailed the relation between the synthesis conditions and the reversible discharge capacity. The first cycle irreversible capacity could be significantly reduced by controlling the precursor chemistry to prevent the formation of the surface –

OH group. Efforts to achieve a better understanding of the electrochemistry of lithium-excess materials involve the connection of crystal structure to electrochemical properties. High pressure-high temperature (HP/HT) techniques are a useful tool to induce structural modifications of materials. It has been previously reported that treatment of complex ceramic materials under increased pressures results in cation arrangements that are not typically possible at atmospheric pressure.[114-116] The high pressure treatment changes both the crystal structure as well as the electronic characteristics of the material. High pressure driven transformations of several electrode materials have been studied and reported, for example Li_xMPO_4 (M = Fe, Co),[115, 117] V_2O_5[118], Ga doped-$LiNiO_2$,[119] and $Li[Li_xNi_{1-x}]O_2$,[120] It is proven that after exposure to high pressure/high temperature conditions, the electrochemical properties varied compared to the ambient pressure materials.

So far little is known about the effect of high pressure on the structure of the layered $LiMO_2$ materials. Work by Wang *et al.* compare experimental (*in situ*) high pressure structural and vibrational properties to *ab initio* calculations for $LiCoO_2$. They found that the structure remains layered up to at least 26 GPa at room temperature,[121] though an important compression of the structure is observed (the *c/a* ratio decreases about 5%). The electrochemistry of the post-treated materials where not explored. Recent work focused on the synthesis under uniaxial pressure of $Li_{1+x}(Ni_{1/2}Mn_{1/2})_{1-x}O_2$ (x=0 and 0.2). [122] In this approach a mixture of reactants is subjected to high pressure/high temperature conditions. The authors found that the increased pressure of synthesis created different cation distributions and varying oxidation states in the Ni ions. The high pressure synthesis resulted in a mixture of phases displaying poor reversible electrochemical properties compared to pristine materials.

The aim of this chapter is to investigate the effect of HP/HT treatment on the structure and electrochemical properties of $Li[Ni_xLi_{1/3-2x/3}Mn_{2/3-x/3}]O_2$ where x=0.25 and 0.5 (i.e. $Li[Li_{1/6}Ni_{1/4}Mn_{7/12}]O_2$ and $LiNi_{0.5}Mn_{0.5}O_2$) in comparison to those of $LiCoO_2$. With this objective, we have combined HP/HT synthesis techniques, X-ray diffraction, electrochemical testing and first principles computation with Density Functional Theory (DFT). We will show how the structural modifications introduced by the HP/HT treatment influence the electrochemical response of the layered materials to demonstrate the superior ability of the Li excess materials to accommodate structural modifications while retaining excellent electrode characteristics.

4.1 Methodologies

4.1.1 Computational

Total energies of the lithium-excess material $Li[Li_{0.16}Ni_{0.25}Mn_{0.583}]O_2$ (or $Li[Li_{1/6}Ni_{1/4}Mn_{7/12}]O_2$) and stoichiometric $LiNi_{0.5}Mn_{0.5}O_2$ were calculated within the DFT+U framework as implemented in the VASP package. [123-125] In the simulated cell of $LiNi_{0.5}Mn_{0.5}O_2$ the Mn and Ni ions are arranged in a zig-zag manner. This Ni-Mn ordering is almost degenerate in energy with the most likely flower-like pattern,[126] and it was chosen for simplicity in this work. In the cell considered for $Li[Li_{1/6}Ni_{1/4}Mn_{7/12}]O_2$, there are four layers: two oxygen layers, one transition metal (TM) layer and one Li layer (48 atoms). Each layer is composed of twelve ions, forming an in-plane supercell. Oxygen ions are close-packed and stacked in ABC (O3) stacking, serving as the frame, while TM slab and Li slab stack alternatively. To simulate the $Li[Li_{1/6}Ni_{1/4}Mn_{7/12}]O_2$ material a complex ordering has to be imposed on the TM layer. It was found that in the most stable configuration the two “excess” Li ions located in the TM layer have distinct environments; one Li ion is surrounded by 6 Mn ions and the other Li ion is surrounded by 5 Mn ions plus 1 Ni ion (Figure 1-4B). Such ordering is compatible with experimental observations. A detailed description of this crystal model is given in reference [26].

As a first step, the structures were fully relaxed (cell parameters, volume and atomic positions) and the final energies of the optimized geometries were recalculated so as to correct the changes in the basis set of the wave functions during relaxation. Computational details are given in our previous works. [127] Secondly, the relaxed structure calculations within the GGA+U approximation were performed at various constant volumes and the energy-volume data were fitted to the Murnaghan equation of state [128]

$$P(V) = \frac{B_0}{B_0'}\left[\frac{V_0}{V}^{B_0'} - 1\right] \tag{4-1}$$

where B_0 is the isothermal bulk modulus, B'_0 is the first derivative with respect to pressure and V is the volume.

Lithium mobility in delithiated $Li[Li_{1/6}Ni_{1/4}Mn_{7/12}]O_2$ at ambient pressure and at 8 GPa was investigated using the Nudged Elastic Band method (NEB) as implemented in VASP. The energetic path for Li motion from one octahedral to adjacent octahedral site across a tetrahedral site in the Li layer was studied at the concentration $Li_{5/6}[Li_{1/6}Ni_{1/4}Mn_{7/12}]O_2$. Constant volume calculations were performed for three intermediate images not further apart than 0.8 Ǻ. To preserve pressure the volume was fixed at that of the lithiated phases. To calculate the energy at the saddle point, cubic splines were fit through the images along each hop.

4.1.2 Experimental

4.1.2.1 Synthesis

Lithium cobalt oxide (Sigma Aldrich) powders were used as obtained. The lithium-excess materials $Li[Ni_xLi_{1/3-2x/3}Mn_{2/3-x/3}]O_2$ where x= 0.25 and 0.5 were synthesized using the hydroxide coprecipitation technique with stoichiometric amounts of LiOH precursor previously described in Chapter 3. The samples were synthesized at 1000°C and furnace cooled to room temperature.

4.1.2.2 High pressure-high temperature treatment

Following the ambient pressure synthesis, the $LiCoO_2$, $LiNi_{0.5}Mn_{0.5}O_2$ and $Li[Li_{1/6}Ni_{1/4}Mn_{7/12}]O_2$ were subjected to HP/HT treatment using different presses: Belt or Conac types for hydrostatic pressure up to 8 GPa, and Rockland for uniaxial pressure up to 3 GPa. No differences were observed whether uniaxial or hydrostatic pressure is applied. Samples were exposed to HP/HT treatment with pressures in the range of 3.0 – 8.0 GPa and temperatures between 800 and 1000°C. After applying the pressure and temperature for one hour, the anvil is quenched to room temperature while pressure is slowly released.

4.1.2.3 Structural characterization

Powder X-ray diffraction patterns were taken on a Siemens D-5000 and X'Pert Pro Alpha I laboratory X-ray diffractometers. Powder diffractions of as-synthesized $Li[Li_{1/6}Ni_{1/4}Mn_{7/12}]O_2$ and $Li[Li_{1/6}Ni_{1/4}Mn_{7/12}]O_2$ following high pressure/high temperature treatment at 5.2 GPA were taken using synchrotron X-ray diffraction at the Advanced Photon Source (APS) at Argonne National Laboratory (ANL) on beamline 11-BM (λ = 0.4122 Å). Synchrotron X-ray diffraction patterns of electrochemically cycled $Li[Li_{1/6}Ni_{1/4}Mn_{7/12}]O_2$ following high pressure treatment were also collected by beamline

11-BM. The cycled samples were hermetically sealed in 0.8 mm Kapton capillaries to minimize air-exposure.

4.2 Results

4.2.1 Computational

DFT methods are a powerful tool to evaluate materials behavior under high pressure. Figure 4-1 shows the calculated total energy as a function of the volume for $Li[Li_{1/6}Ni_{1/4}Mn_{7/12}]O_2$ (Figure 4-1a) and $LiNi_{0.5}Mn_{0.5}O_2$ (Figure 4-1B), together with the corresponding fit of the DFT data to the Murnaghan equation of state (EOS). [128] From the fitting to the EOS, one can extract the variation of pressure as a function of the volume (right axis in Figure 4-1). Note that the volume corresponds to 144 atoms to facilitate comparison with experiments. Table 4-1 compares the parameters of the DFT data fitted to the EOS, with those experimentally and computationally obtained for $LiCoO_2$. $LiNi_{0.5}Mn_{0.5}O_2$ and $Li[Li_{1/6}Ni_{1/4}Mn_{7/12}]O_2$ exhibit bulk modulus of 124 GPa and 117 GPa, respectively. These values are lower than the bulk modulus found for $LiCoO_2$ (149 GPa), suggesting that Ni and Mn substitution for Co in the TM layer produces a softer, more compressible material. The lithium-excess material is more compressible than the stoichiometric $LiNi_{0.5}Mn_{0.5}O_2$ due to the presence of Li ions in the TM layer, as discussed below.

Figure 4-2 shows the calculated Li-O and M-O bond lengths as a function of volume for $Li[Li_{1/6}Ni_{1/4}Mn_{7/12}]O_2$, up to a pressure of 19 GPa (for volume-pressure dependence with volume (Figure 4-1). The cationic ordering in the TM layers is depicted in Chapter 1 in Figure 1-4B. The Li-O bonds compress 5.8% in the Li layer and 4.4% or 2.4% depending on the local environment in the TM layer. The Mn-O and Ni-O bonds are more difficult to compress than Li-O with their relative compressibility being 2.4%

and 3%, respectively. The larger Ni cation renders a more compressible Ni-O bond. The predicted bond compressibility is similar to those found in $LiCoO_2$;[121] Li-O 5.2 % and Co-O 1.5%. The Li-O bonds, in the Li layer, are about two to three times more compressible than the M-O bonds in the TM layer. It is plausible that the lower bulk moduli of $Li[Li_{1/6}Ni_{1/4}Mn_{7/12}]O_2$ compared to $LiNi_{0.5}Mn_{0.5}O_2$ is due to a more compressible TM layer on account of the presence of Li ions.

The compression of these layered materials is anisotropic. Experimental results for $LiCoO_2$ shows evidence of a 1.5% and 2.8 % contraction for the *a* and *c* lattice parameters, respectively, between ambient pressure and 19.9 GPa. The calculated data yields compressions of 3.5% (*a* parameter) and 5% (*c* parameter) for $Li[Li_{1/6}Ni_{1/4}Mn_{7/12}]O_2$ in the same pressure range. The anisotropic compression of the structure is correlated to the different compressions of inter-plane and in-plane bonds. Figure 4-3 shows the calculated in-plane and inter-plane contractions between adjacent metal ions for $Li[Li_{1/6}Ni_{1/4}Mn_{7/12}]O_2$. The inter-plane distances shorten more than in-plane distances independent of the ion (Li, Mn, or Ni), in good agreement with the large contractions in the *c* axis direction.

Lithium diffusion in the Li layer occurs from one octahedral site to the adjacent octahedral site across a face-shared tetrahedral site, a path schematized in Figure 4-4. During the hop, lithium ions can get trapped in the tetrahedral site forming a Li_{oct}-Li_{tet} dumbbell configuration with the Li ions in the adjacent TM layer. For $Li[Li_{1/6}Ni_{1/4}Mn_{7/12}]O_2$ previous investigations [127] have shown that the formation of such configuration is favored during delithiation (at c.a. 4.5 V). This causes structural transformation during electrochemical cycling causing the degradation of the electrode material. For the high pressure treated materials, one can expect that the more contracted oxygen arrangement precludes the mobility of Li ions from the octahedral sites into the tetrahedral sites, since the ions must cross a smaller triangular face, and occupy a smaller tetrahedral site. Figure 4-4 compares the calculated energy path for Li motion in $Li_{5/6}[Li_{1/6}Ni_{1/4}Mn_{7/12}]O_2$ at ambient pressure and at a constant volume of 1183 $Å^3$, which corresponds to 8.0 GPa (Figure 4-1). According with previous works at ambient pressure, the Li ion will be trapped in the tetrahedral site, the stabilization energy being about 0.1 eV with respect to the more stable octahedral site. In the more contracted lattice, there is an energetic barrier of 0.07 eV to pass across the triangular face shared between octahedral and tetrahedral sites. Nevertheless the formation of tetrahedral lithium is still favored by 0.03 eV.

Based on the DFT results, some trends can be extracted. (i) The $Li[Li_{1/6}Ni_{1/4}Mn_{7/12}]O_2$ material is softer than $LiCoO_2$ or $LiNi_{0.5}Mn_{0.5}O_2$ and will undergo larger structural modifications under a HP/HT treatment. (ii) In layered $LiMO_2$, there is a notorious compression of the Li-layer. The TM ions have smaller ionic radii than Li and may easily be accommodated in the contracted Li layer; therefore, a high pressure treatment will favor a large Li-TM interlayer mixing. (iii) The more compact structure obtained upon HP/HT treatment will have lower ion mobility and hindered Li intercalation. (iv) During delithiation, the formation of tetrahedral Li is still energetically favored, though to a lesser extent.

Even though some predictions can be made, it is important to recall that high pressure materials are metastable phases at ambient pressure, and quite frequently quenched samples do not retain the crystal structure that is actually the thermodynamically stable form at high pressure. Obviously, the retention at ambient pressure of the stable high pressure-structure is also driven by kinetics. In short, the structural changes observed in quenched samples after a HP/HT treatment might be less severe than those anticipated from DFT.

4.2.2 Experimental Results

4.2.2.1 $LiCoO_2$

Previous *in situ* high pressure experiments demonstrated that $LiCoO_2$ remains phase pure with the $R\overline{3}m$ space group up to 26 GPa and room temperature.[121] A compression of the unit cell of about 5% was observed, as discussed above related to the decreasing of the *c* lattice parameter and the high compressibility of the Li-O bonds. In the present work quenching experiments are performed, and therefore structural variations under pressure are not observed, but rather the resulting structural changes after a HP/HT treatment are reported.

Figure 4-5 shows X-ray diffraction (XRD) patterns collected from pristine (4-5a) and high pressure high temperature treated $LiCoO_2$ (HP-$LiCoO_2$) at 4.0 GPa (4-5b) and 8.0 GPa (4-5c) at 1000°C. Rietveld refinements of the patterns indicate that the post treated materials remain phase pure. Table 4-2 shows the Rietveld refinement results following HP/HT treatment. The *c* lattice parameters decrease less than 1% from 14.047 Å to 14.040 Å while the *a* lattice parameters decreases from 2.816 Å to 2.812 Å resulting in a 0.3% decrease in cell volume as a function of pressure treatment. The findings confirm that HP/HT (up to 8 GPa/1000 ºC) do not drastically affect $LiCoO_2$, as it was observed during *in situ* experiments. Figure 4-6 compares the electrochemical cycling profile of pristine $LiCoO_2$ and the post-treated $LiCoO_2$. The two post-treated materials are electrochemically active showing capacities and voltage profile very similar to the pristine material. High pressure and high temperature treatment to 8.0 GPa and 1000°C do not significantly affect the electrochemical properties.

4.2.2.2 $LiNi_{0.5}Mn_{0.5}O_2$ (x=0.5)

Figure 4-7 shows the XRD patterns collected from $LiNi_{0.5}Mn_{0.5}O_2$ as synthesized (Figure 4-7A) following high pressure/high temperature treatment at 5.2 GPa (Figure 4-7B) and at 8.0 GPa (Figure 4-7C). Examining the XRD patterns of the post treated samples indicates that an unknown secondary phase may have formed as evidenced by shoulders on the high two theta side of the (104) peak; however, fitting using the $Fd\bar{3}m$ or *C2/m* space groups for this second phase did not yield acceptable results. The results of fitting the sample to the $R\bar{3}m$ space group can be seen in Table 4-2. As the pressure increases to 8.0 GPa, c/a lattice ratio decreases from 4.947 to 4.900. Moreover, the amount of Li/Ni mixing increases from 11% to 32% following treatment at 8.0 GPa. The intensity ratio of the (003) peak versus the (104) peak is an indicator of the layeredness of the material.[44] The I(003) / I(004) ratio decreases from 0.78 in the pristine sample to 0.43 at 5.2 GPa to 0.18 in the 8.0 GPa sample. Moreover, the intensity ratio of the (101) to ((006)+(012)) peaks decreases, and the degree of peak separation (110)/(018) doublet shrinks indicating that the layeredness of the material worsens.[44, 129, 130] These findings are in good agreement with DFT results.

The structural modifications observed in the X-ray diffraction profiles are confirmed in the electrochemical testing. It is well established that for $LiNi_{0.5}Mn_{0.5}O_2$, a larger amount of Li/Ni mixing is detrimental to the electrochemical performance.[10] Accordingly, increasing HP/HT treatment increases the Li/Ni mixing and consequently inhibits the electrochemical performance. Figure 4-8 shows the first cycle charge and discharge profiles. The pristine material yields charge and discharge capacities of 189 mAh/g and 164 mAh/g, respectively, within the 4.8-2.0 V voltage window. Following HP/HT treatment, the sample treated at 5.2 GPa yields 140 mAh/g upon charging; however only 80 mAh/g is reversible following the first discharge. The capacity further fades when the material is treated at 8.0 GPa, with initial charge and discharge capacities of 69 mAh/g and 23 mAh/g respectively.

4.2.2.3 Lithium-excess $Li[Li_{1/6}Ni_{1/4}Mn_{7/12}]O_2$ (x=0.25)

Figure 4-9A shows the synchrotron X-ray diffraction pattern of the pristine $Li[Li_{1/6}Ni_{1/4}Mn_{7/12}]O_2$. The pristine phase can be indexed to the typical $R\bar{3}m$ phase and shows good layering with 4% Li/Ni mixing. Figure 4-9B illustrates that the X-ray diffraction pattern of the HP/HT materials exposed to 5.2 GPa still shows the superlattice peaks between 20-30° observed in the pristine materials, which are associated with a honeycomb ordering of Li^+, Ni^{2+} and Mn^{4+} in the transition metal layer consistent with the Li_2MnO_3-end member type ordering.[11, 12] The XRD pattern of the post treated material shows distinct evidence of second phase formation in addition to the superlattice peaks as evidenced by additional peak/shoulders next to the (101), (104), (018) and (110) peaks. Figure 4-9C shows the XRD pattern collected following HPHT treatment at 8.0 GPa. The secondary peak intensities have increased. From a structural viewpoint, the Rietveld refinement results, seen in Table 4-2, indicate that at 5.2 GPa, two layered phases exist. The primary phase shows a 0.07 Ǻ and 0.04 Ǻ decrease in the *a* and *c* lattice parameters respectively, indicating a densification of the primary phase. The calculations predicted stronger out-of-plane lattice contractions of the material which is observed in the refinement of the XRD pattern. The amount of Li/Ni mixing remains similar below 5%. In the secondary phase, the amount of Li/Ni mixing increases to 16%. Also the *a* and *c* lattice parameters increase 0.035 Ǻ and 0.012 Ǻ from the pristine material respectively, causing the c/a ratio to decrease which is an indication of decreased layeredness.[44]

Figure 4-10 compares the electrochemical properties during the first charge/discharge cycle of the pristine lithium-excess material and following high pressure treatment at 5.2 GPa and 8.0 GPa. The HP/HT treated samples display a good electrochemical response, unlike the case of $LiNi_{0.5}Mn_{0.5}O_2$. The HPHT treated samples have the same absolute irreversible capacity, but a lower reversible capacity than the untreated material indicating that the treatment does not improve the first cycle capacity loss. Both materials exposed to high pressure and high temperature showed initial charge capacities exceeding 200 mAh/g. There are important differences, particularly in the plateau region of 4.5 V region which corresponds to the oxygen removal or surface modification reactions. It has been shown that these charge compensation mechanisms are accompanied with simultaneous oxygen removal or activation.[33, 110, 112] The decreasing voltage plateau length shows that not only does the anomalous capacity originate through the activation of oxygen but concurrently is charge compensated through transition metal migration, Li^+ ion tetrahedral formation and second layered phase formation. The pristine material displayed the longest plateau region as well as a lower voltage during charging than the HP/HT materials. As the level of pressure applied to the material increased, the length of the plateau region at 4.5 V decreased with the associated specific capacity decreasing from 110 mAh/g (pristine) to 85 mAh/g (5.2 GPa) to 20 mAh/g (8.0 GPa). As the plateau region shortens, the amount of structural rearrangement would be expected to be reduced; however, we observe the same extent of structural rearrangement following electrochemical cycling as in the pristine material. Figure 4-11 shows the capacity retention with cycling for pristine and the material treated at 5.2 GPa. Both materials are able to show reversible capacities exceeding 200 mAh/g after the first discharge and stable charge and discharge capacities for the first 10 cycles.

Following ten electrochemical cycles, the cathode material exposed to HP/HT treatment at 5.2 GPa was recovered. Figure 4-12 shows the collected X-ray diffraction pattern. This pattern can be compared with the pristine material following electrochemical cycling shown in reference [26]. Important changes are observed comparing with the initial HP/HT material (Figure 4-9B). Both the superlattice peaks and the evidence of distinct shoulders have drastically decreased in intensity or disappeared. The disappearance of the superlattice peaks was previously observed for the pristine material and it was ascribed to the loss of cation ordering in the TM layer.[21, 127] In Figure 4-12, the Rietveld refinement of the XRD pattern following electrochemical cycling using two layered phases led to improved fitting parameters. As predicted by DFT results, the introduction of tetrahedral lithium into the secondary phase further improved the fitting parameters as seen in Table 4-3. The Rietveld refinement indicates that following electrochemical cycling, both phases expand and TM ions migrate to and from the Li layer. The amount of Li/Ni mixing increases from 0.047 to 0.066 in the primary phase and decreases from 0.164 to 0.150 in the secondary phase. This indicates that during electrochemical cycling the material undergoes large changes in cation occupancies, lattice parameters, as well as formation of a secondary phase with tetrahedral Li, yet remains electrochemically active displaying large specific capacities.

The details of the cation migrations and structural changes have been reported in our previous paper.[127]

4.3 Discussion

In this work, we aimed to induce structural modifications in the layered materials by HP/HT treatment in order to obtain a better understanding of the electrochemical behavior dependence with structural factors. This knowledge is critical for the commercialization and application of the promising lithium-excess electrode materials. HP/HT techniques provided a unique way of introducing structural modifications in the layered materials. We have shown that the structural modifications that can be achieved following a HP/HT treatment are different to those attainable by altering other variables in the synthesis process, such as the nature of the reactants or the temperature of synthesis.

The results obtained for $LiCoO_2$, $LiNi_{0.5}Mn_{0.5}O_2$ and $Li[Li_{1/6}Ni_{1/4}Mn_{7/12}]O_2$ following HP/HT treatment reveal that these layered materials display a large resistance to structure collapse or phase transformation. It should be noted that samples have been subjected to pressures up to 8 GPa at 1000 ºC. Under similar conditions other electrode materials have already transformed to high-pressure polymorphs, or decomposed. Indeed the calculated bulk moduli (around 130 GPa) of these layered oxides is larger than that of most electrode materials; V_2O_5 (calculated 20 GPa [131]), Li_2MSiO_4(M = Co, Mn experimental 90 GPa [132]), $LiCoPO_4$ (calculated 80 GPa [133]), $FePO_4$ (experimental 24 GPa [134]). Within the family of layered materials $Li[Li_xM_{1-x}]O_2$, the compressibility is a function of the nature of TM and the Li content. DFT calculations clearly showed that Li-O bonds are twice as compressible as M-O bonds. Furthermore, the substitution of Co with Li, Ni and Mn in the transition metal layer softens the material and decreases the bulk modulus. Rietveld refinement of the XRD spectra following high pressure treatment confirms these results. $LiCoO_2$ showed minimal structural changes. Conversely, $LiNi_{0.5}Mn_{0.5}O_2$ and $Li[Li_{1/6}Ni_{1/4}Mn_{7/12}]O_2$ showed large structural changes and in the latter the formation of second layered phase is observed.

Synthetic history and consequent structural modifications impose a fingerprint in the electrochemical behavior. The electrochemical properties of both high pressure treated $LiCoO_2$ samples were nearly identical to the pristine material, as expected for the minor structural distortion observed. The high pressure treatment of $LiNi_{0.5}Mn_{0.5}O_2$ (x=0.5) caused considerable structural modifications that decreased the layered characteristics of the material and increased the amount of Li/Ni mixing. As the Li-O bonds are twice as compressible compared to M-O bonds, the effect of pressure is to equalize the thickness of TM and Li layers favoring interlayer mixing. The electrochemical properties of $LiNi_{0.5}Mn_{0.5}O_2$ are optimal with minimal Li/Ni interlayer mixing. The first electrochemical cycle indicates that as the pressure of the treatment increases, the material becomes less electrochemically active. It is likely that the increased structural disorder from the Li/Ni mixing may have blocked Li intercalation pathways inhibiting the electrochemical performance of the material. Besides blocking of the Li paths by interlayer mixing, we have shown that densification of the lattice under pressure may also hinder the Li mobility (Figure 4-4). In the end, the structural modifications induced by the HP/HT treatment turn the samples electrochemically inactive.

The Li excess material has increased amounts of Li-O bonding originating from Li in the transition metal layer. This bonding shows the largest calculated compressibility and first principles calculations anticipated major structural changes for the lithium-excess $Li[Li_{1/6}Ni_{1/4}Mn_{7/12}]O_2$ material. Indeed the analysis of the X-ray diffraction data indicates that the material forms a second layered phase. This phase shows an expanded lattice as well as a 0.125 increase in Li/Ni mixing compared to the pristine material. The primary phase shows 0.04 Å reduction in *c* lattice parameter from the pristine structure. The amount of Li/Ni mixing remains near 4% following the treatment. Surprisingly, and contrary to what happened with $LiNi_{0.5}Mn_{0.5}O_2$, all these structural rearrangements do not result in a deterioration of the electrochemical behavior. The material was able to display electrochemical capacities exceeding 200 mAh/g for 10 cycles.

Interestingly, the anomalous capacities of the high pressure material resulted in a shorter plateau region at 4.5 V. It has been shown that the source of excess Li and the plateau region is related to the activation of Li_2MnO_3 (or $Li[Li_{1/3}Mn_{2/3}]O_2$) via oxygen loss.[20, 112] Based on X-ray diffraction and the electrochemical results, we predict that the second layered phase that forms following HP/HT treatment may be related to the $Li[Li_{1/3}Mn_{2/3}]O_2$-type end member of $Li[Ni_xLi_{1/3-2x/3}Mn_{2/3-x/3}]O_2$ with large amounts of defects. The structure refined using the Rietveld method of the secondary layered phase could be written as $Li_{0.84}Ni_{0.16}[Li_{1/3}Mn_{7/12}Ni_{1/12}]O_2$, within experimental error, which is structurally equivalent to $Li[Li_{1/3}TM_{2/3}]O_2$. This phase is believed to account for the majority of the anomalous capacity observed during the voltage plateau region.[29, 135] Following electrochemical cycling of the Li excess material, the shoulders at the majority of the peaks seen in the uncycled 5.2 GPa treated sample disappear and decrease in intensity. Also, the amount of structural reorganization including lattice expansion and cation migration is large as seen in Table 4-3. Rietveld refinement indicates that tetrahedral Li occupancy may be observed following electrochemical cycling of the high pressure material. DFT data predicted that the formation of tetrahedral Li is still energetically favorable in the compressed lattice. Additionally, the material still exists as two layered phases; with one phase including tetrahedral Li. Similarly as previously studied, the lattices of both phases expand and the amount of Li/Ni mixing increases compared to that of the pristine untreated sample.[127] The electrochemical results show that as the pressure increases, the length of the plateau region decreases indicating that the amount of Li_2MnO_3 activation is decreased, which may be due to the phase separation of the two end members that form the solid solution of $Li[Ni_xLi_{1/3-2x/3}Mn_{2/3-x/3}]O_2$.

The results reported indicate that significant structural rearrangement occurs in the HPHT treated lithium-excess layered material during electrochemical cycling. It is expected that the formation of a second layered phase and increased cation mixing induced by HPHT treatment before cycling would hinder the electrochemical characteristics of the lithium-excess material. However, the material structurally rearranges during electrochemical cycling to improve the layered characteristics unlike $LiNi_{0.5}Mn_{0.5}O_2$. The results identified here indicate that the structural rearrangements seen during the first electrochemical cycle are critical for the electrochemical activation of the material. Further research identifying when and how structural modifications occur during the first electrochemical cycle are necessary to understand how to improve the intrinsically poor rate capability and irreversible capacity loss.

Efforts to improve the performance of layered $LiMO_2$ cathode materials involve a deep understanding of the connection between crystal structure and electrochemical properties. In this context, we have investigated the high pressure-treated layered materials $LiCoO_2$ and $Li[Ni_xLi_{1/3-2x/3}Mn_{2/3-x/3}]O_2$ where x=0.25 and 0.5 combining both computational and experimental methods. We can conclude that the substitution of Co for Ni and Mn soften the layered oxides and the introduction of Li in the transition metal layer further softens the material. Some of the structural modifications induced by the HP/HT treatment are retained in the quenched samples, resulting in different electrode characteristics than those of the pristine materials.

This work illustrates that the synthesis conditions and post synthesis cathode treatment play a critical role in the electrochemical properties. However, we have not identified the source of the irreversible capacity loss and the inferior rate capabilities of the lithium-excess transition metal oxides which are hindering the commercial applications. A detailed understanding of the stability of the surface structural changes associated with cation migration is needed.

Table 4-1. Calculated equation of state parameters for layered-$Li[Li_xM_{1-x}]O_2$ materials. E_0, V_0, B_0 and B_0' are the zero-pressure energy, volume, bulk modulus and its pressure derivative, respectively.. Experimental values are given in parentheses.

Compound	B_0 (Gpa)	B_0'	V_0 (A^3)	E_0 (eV)
$LiCoO_2$[20]	142 (149)	4.51 (4.1)	1186.06 (1157)	
$LiNi_{0.5}Mn_{0.5}O_2$	125	3.80	1278.70 (1241)	-858.24
$Li[Li_{1/6}Ni_{1/4}Mn_{7/12}]O_2$	117	3.90	1261.58 (1219)	-873.76

Table 4-2. Rietveld refinement of pristine and high pressure treated $LiCoO_2$, and $Li[Ni_xLi_{1/3-2x/3}Mn_{2/3-x/3}]O_2$ (x=0.5, 0.25). n_TM (Co, Ni) is the occupation of the 3b site (Li layer) by Nickel or Cobalt with the remainder of atoms on the site being lithium. *a* and *c* lattice parameters given in Angstroms (Å)

	Pristine	5.2 Gpa	8.0 Gpa
$LiCoO_2$	a = 2.8155 ±0.0003 c = 14.0473±0.0015 c/a = 4.989 V = 96.43 z(O) = 0.2577±0.001 n_Co = 0.040±0.002 R_{wp} = 4.83 %; R_b = 5.62%	a = 2.8127±0.0003 c = 14.0441±0.0014 c/a = 4.993 V = 96.22 z(O) = 0.2597±0.0006 n_Co = 0.061±0.002 R_{wp} = 4.97%; R_b = 3.77%	a = 2.8120±0.0004 c = 14.0406±0.0021 c/a = 4.993 V = 96.15 z(O) = 0.2600±0.0009 n_Co = 0.007±0.001 R_{wp} = 3.54%; R_b = 6.62%
$LiNi_{0.5}Mn_{0.5}O_2$	a = 2.8900±0.0006 c = 14.2975±0.003 c/a = 4.947 V = 103.42 z(O) = 0.2563±0.0009 n_Ni = 0.117±0.002 R_{wp} = 5.03%; R_b = 3.01%	a = 2.8975±0.0007 c = 14.2908±0.004 c/a = 4.932 V = 103.90 z(O) = 0.2559±0.0012 n_Ni = 0.197±0.002 R_{wp} = 3.56% ; R_b =4.77%	a = 2.9165±0.0015 c = 14.2914±0.00212 c/a = 4.900 V = 105.276 z(O) = 0.2561±0.0056 n_Ni = 0.322±0.004 R_{wp} = 5.65%; R_b = 12.1%
$Li[Li_{1/6}Ni_{1/4}Mn_{7/12}]O_2$	a = 2.8667 ±0.0002 c = 14.2772±0.0003 c/a = 4.980 V = 101.61 z(O) = 0.2580±0.0001 n_Ni = 0.039±0.001 R_{wp} = 14.5%; R_b = 7.6%	**Phase 1:** a = 2.8600±0.0001 c = 14.2380±0.0002 c/a = 4.978 V = 100.86 z(O) = 0.2570±0.0015 n_Ni = 0.047±0.002 Phase Fraction: 67% **Phase 2:** a = 2.9022±0.0001 c = 14.2887±0.0004 c/a = 4.923 V = 104.23 z(O) = 0.2580±0.0003 n_Ni = 0.164±0.001 R_{wp} = 7.92%; R_b = 4.03%	

Table 4-3. Rietveld refinement results for $Li[Ni_xLi_{1/3-2x/3}Mn_{2/3-x/3}]O_2$ (x=0.25) following 5.2 GPa treatment and 10 electrochemical cycles. n_Ni is the occupation of the 3b site (Li layer) by Nickel with the remainder of atoms on the site being lithium. n_Li is the occupation of the tetrahedral site by lithium (1/3, 2/3, z=0.810) *a* and *c* lattice parameters given in Angstroms (Å)

	Pristine after 5.2 GPa	Following 10 electrochemical cycles
$Li[Li_{1/6}Ni_{1/4}Mn_{7/12}]O_2$ Following HP/HT treatment at 5.2 GPa	**Phase 1:** a = 2.8600 ±0.0001 c = 14.2380±0.0002 c/a = 4.978 z(O) = 0.2570 n_Ni = 0.047±0.002 Phase Fraction: 67% **Phase 2:** a = 2.9022±0.0001 c = 14.2887±0.0004 c/a = 4.923 z(O) = 0.2580 n_Ni = 0.164±0.001 R_{wp} = 7.92%; R_b = 4.03%	**Phase 1:** a = 2.8814±0.0001 c = 14.3381±0.0003 c/a = 5.006 z(O) = 0.2570±0.0001 n_Ni = 0.066±0.002 Phase Fraction: 60% **Phase 2:** a = 2.9095±0.0001 c = 14.3118±0.0001 c/a = 5.004 z(O) = 0.2580±0.0002 n_Ni = 0.152±0.003 n_Li = 0.146±0.002 R_{wp} = 5.7%; R_b = 2.33%

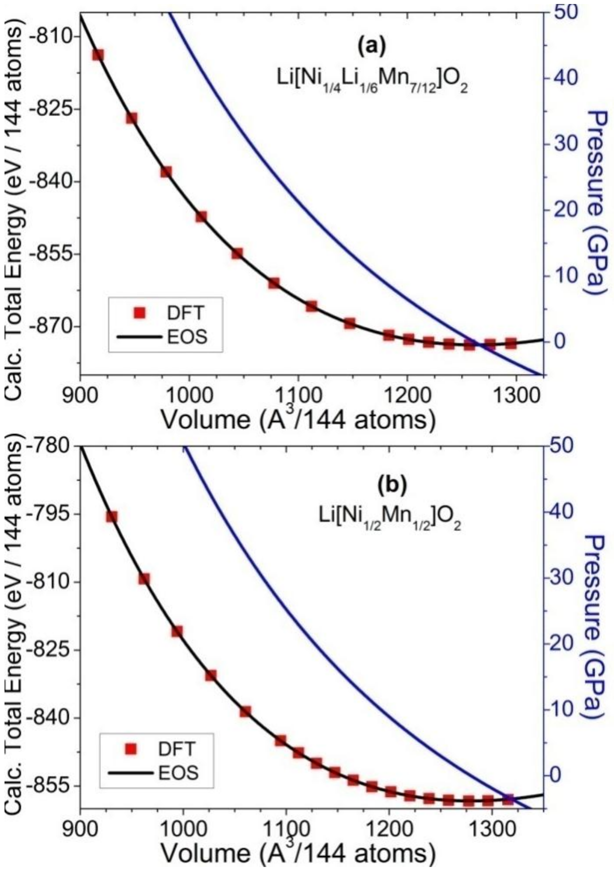

Figure 4-1. Calculated total energy as a function of the volume for A) Li[Ni$_{1/2}$Mn$_{1/2}$]O$_2$ and B) Li[Ni$_{1/4}$Li$_{1/6}$Mn$_{7/12}$]O$_2$. Marks correspond to the DFT data and the black line show the fit to the Murnagham equation of states. The dependence of pressure with volume is given in the right axis.

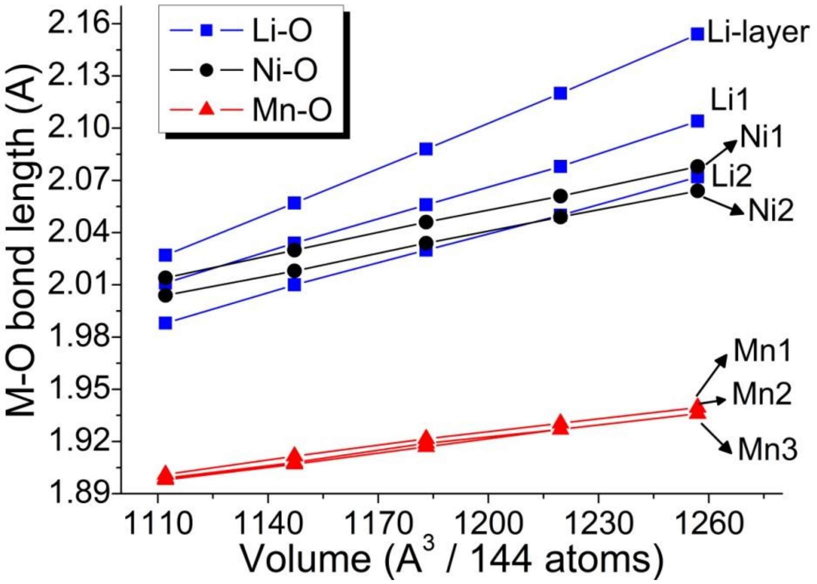

Figure 4-2. Variation of the calculated Li-O and M-O bond lengths under pressure for $Li[Li_{1/6}Ni_{1/4}Mn_{7/12}]O_2$. The ordering in the TM layer is shown in Figure 1-4.

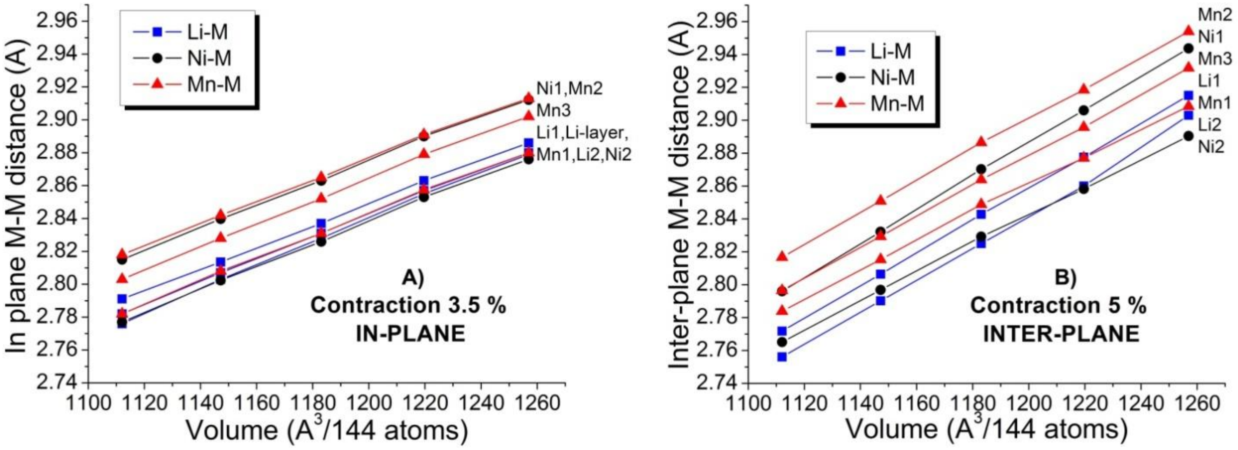

Figure 4-3. Calculated contractions between adjacent metal ions in $Li[Li_{1/6}Ni_{1/4}Mn_{7/12}]O_2$ under pressure A) in-plane and B) inter-plane.

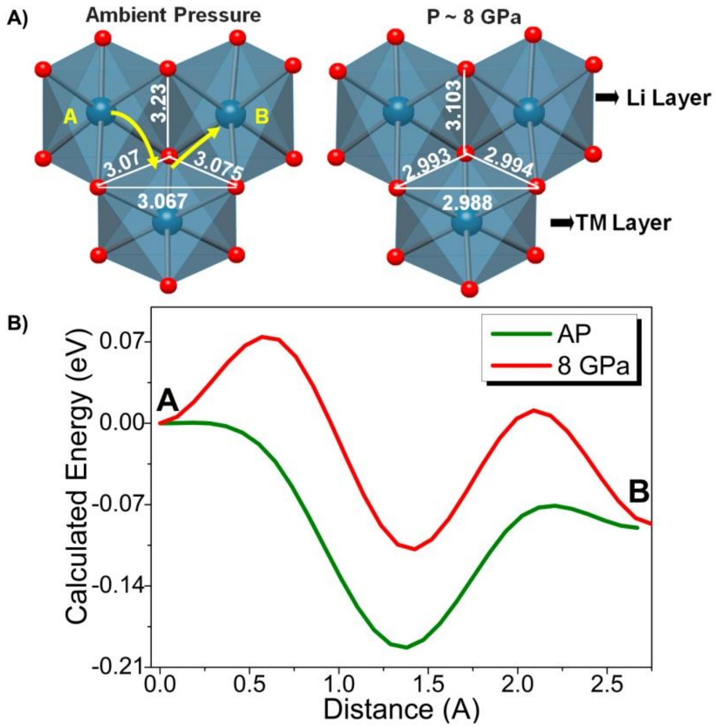

Figure 4-4. Examination of Li diffusion in the Li layer of $Li[Li_{1/6}Ni_{1/4}Mn_{7/12}]O_2$.at increasing pressures showing A) the sketch of the path for Li diffusion in the Li layer at increasing pressures. Blue=Li, Red=Oxygen and B) the calculated energy of the Li mobility at ambient pressure (green) and at c.a. 8 GPa (red).

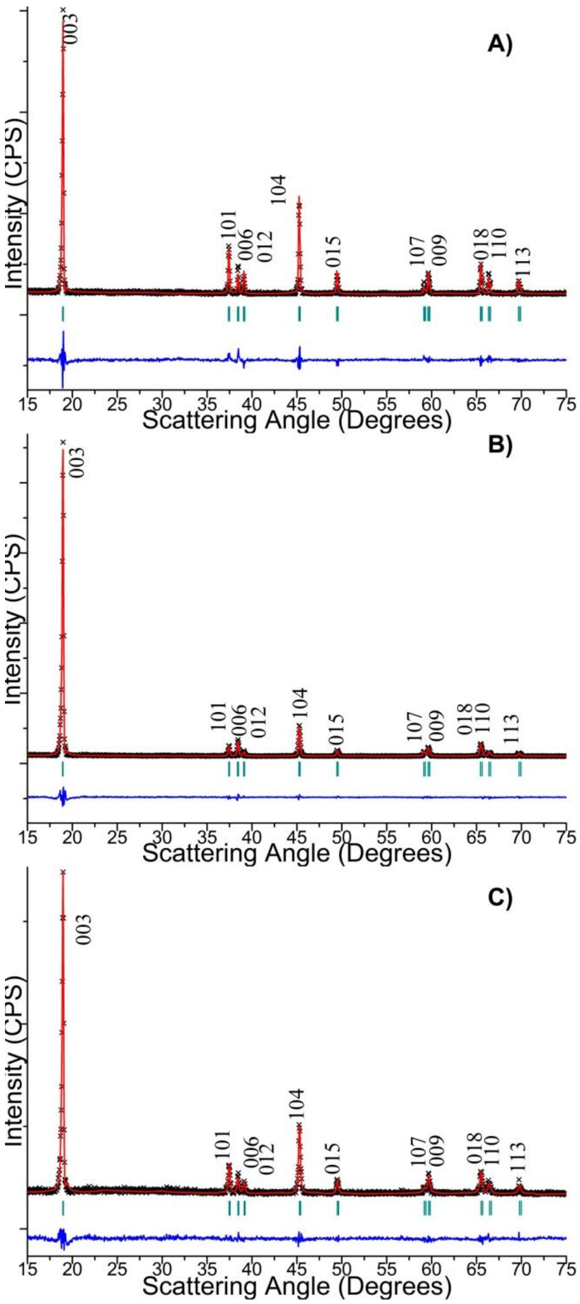

Figure 4-5. Comparison of the Rietveld refinement results from x-ray diffraction (XRD) patterns collected from $LiCoO_2$ A) before HP treatment and B) following 4.0 GPa and C) following 8.0 GPa at 1000°C. The black crosses represent the observed pattern, the red line corresponds to the calculated diffraction pattern and the blue is the difference pattern. The teal lines correspond to peak positions from the $R\bar{3}m$ space group.

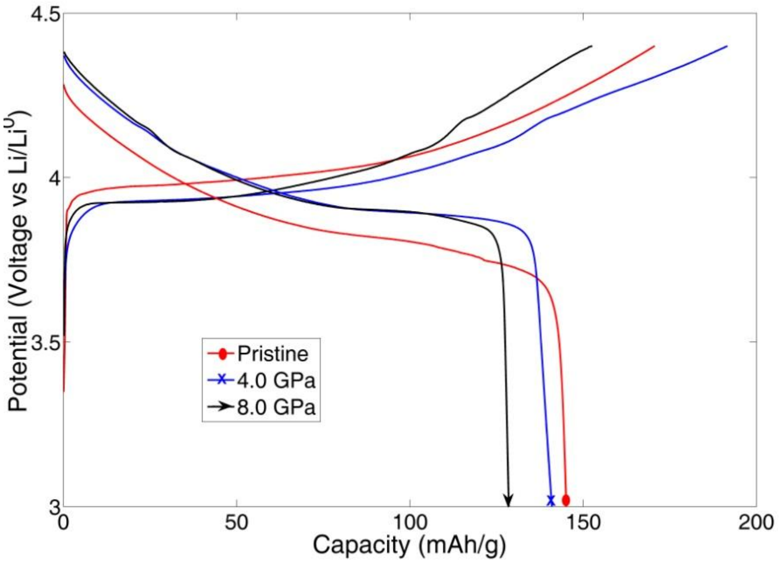

Figure 4-6. Comparison of the electrochemical cycling profile of pristine $LiCoO_2$ (red) and high pressure treated $LiCoO_2$ at 4.0 GPa (blue X) and 8.0 GPa (black arrow). A voltage window of 4.4 – 3.0 V was used

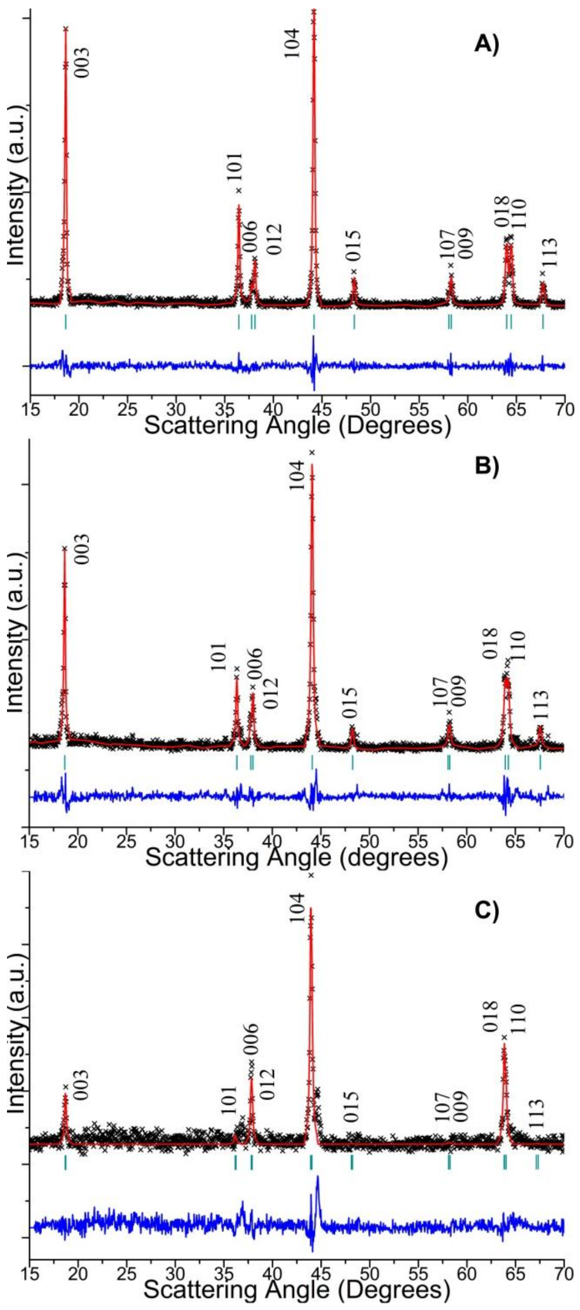

Figure 4-7. Comparison of the Rietveld refinement results from x-ray diffraction (XRD) patterns collected from $LiNi_{0.5}Mn_{0.5}O_2$ A) before HP treatment and B) following 5.2 GPa and C) following 8.0 GPa at 1000°C

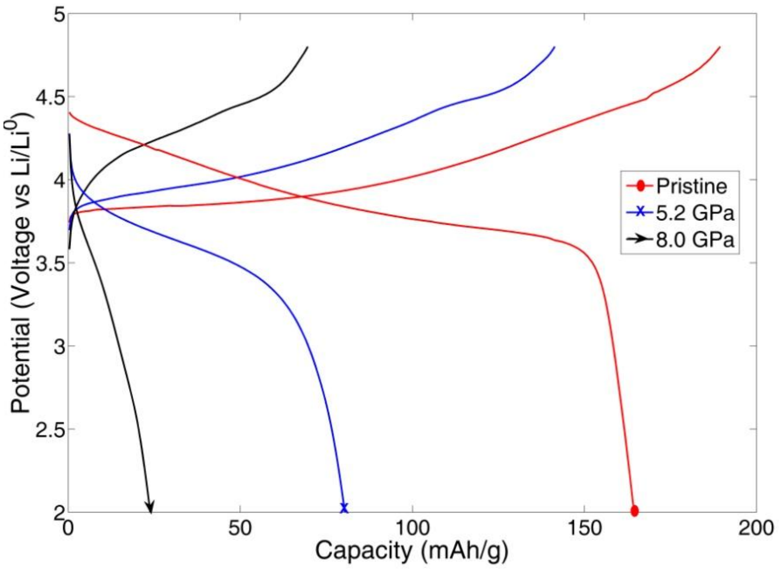

Figure 4-8. Comparison of the electrochemical cycling profile of pristine $LiNi_{0.5}Mn_{0.5}O_2$ (red) and HP/HT treated $LiNi_{0.5}Mn_{0.5}O_2$ at 5.2 GPa (blue X) and 8.0 GPa (black arrow). A voltage window of 4.8-2.0 V was used.

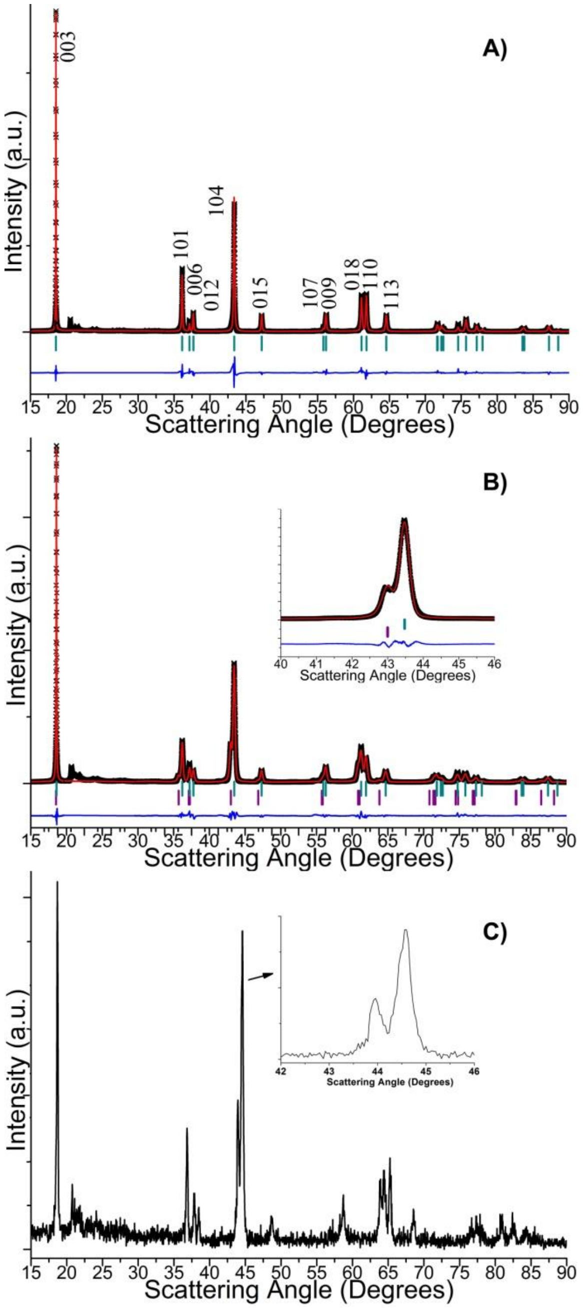

Figure 4-9. Comparison of the Rietveld refinement results from x-ray diffraction (XRD) patterns collected from $Li[Li_{1/6}Ni_{1/4}Mn_{7/12}]O_2$ A) before HP treatment and B) following 5.2 GPa and C) following 8.0 GPa at 1000°C The 2θ converted to those corresponding to a CuKα wavelength (λ=1.54 Å)

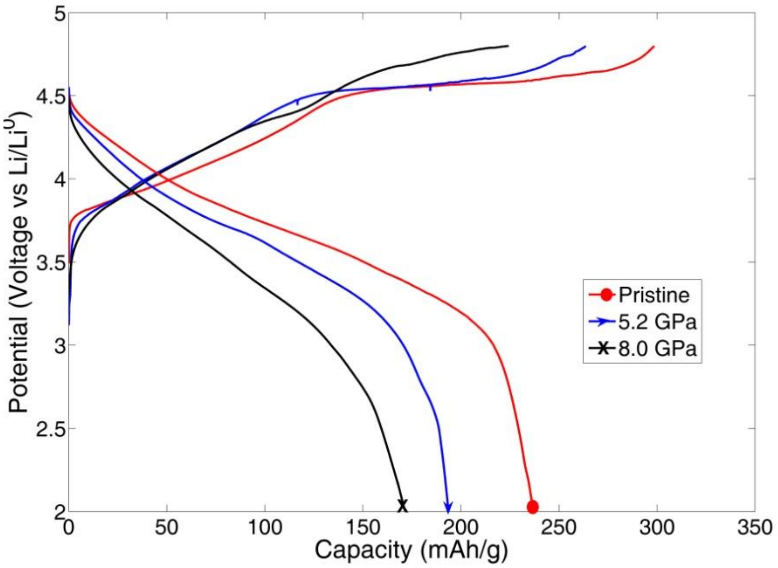

Figure 4-10. First cycle electrochemical profiles of pristine Li[$Li_{1/6}Ni_{1/4}Mn_{7/12}$]$O_2$ (red) and those exposed to HP/HT treatments at 5.2 GPa (blue arrow) and 8.0 GPa (black X) and 1000°C. Voltage windows of 4.8-2.0 V were used.

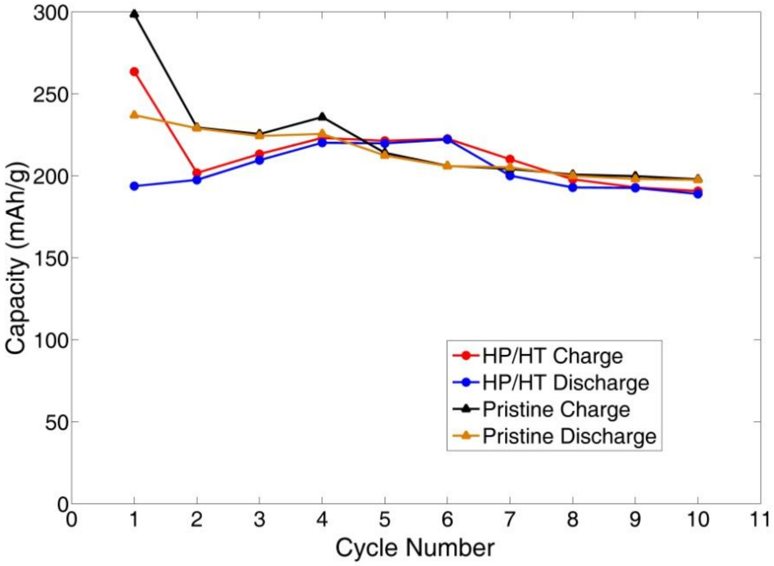

Figure 4-11. Comparison of the cycling stability of Li[$Ni_{1/4}Li_{1/6}Mn_{7/12}$]$O_2$ before and following HP/HT treatment at 5.2 GPa

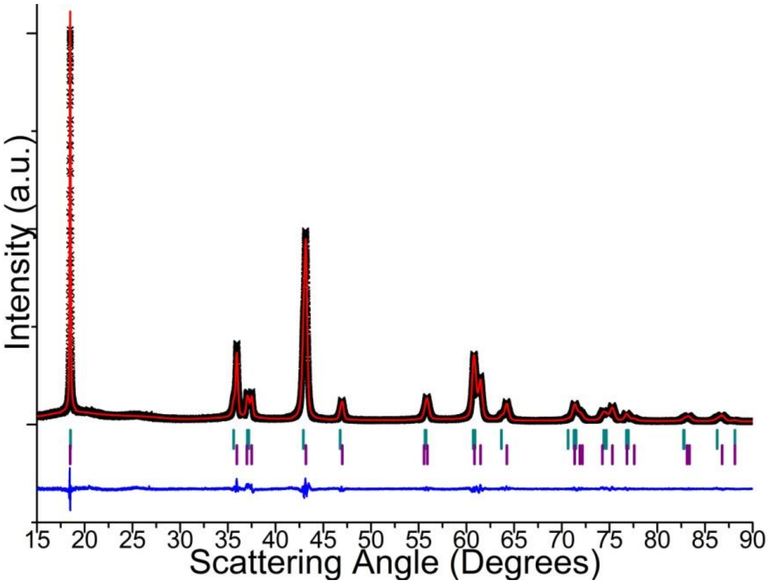

Figure 4-12. Rietveld refinement results from X-ray diffraction (XRD) patterns collected from $Li[Li_{1/6}Ni_{1/4}Mn_{7/12}]O_2$ exposed to HP/HT treatments at 5.2 GPa following 10 electrochemical cycles. The 2θ converted to those corresponding to a CuKα wavelength (λ=1.54 Å)

CHAPTER 5

IDENTIFYING SURFACE STRUCTURAL CHANGES IN LAYERED LITHIUM-EXCESS NICKEL MANGANESE OXIDES IN HIGH VOLTAGE LITHIUM ION BATTERIES: A JOINT EXPERIMENTAL AND THEORETICAL STUDY

This chapter is part of the paper: “Identifying Surface Structural Changes in Layered Lithium-Excess Nickel Manganese Oxides in High Voltage Lithium Ion Batteries: A Joint Experimental and Theoretical Study” by Bo Xu, Christopher R. Fell, Miaofang Chi Ying Shirley Meng.; Energy and Environmental Sciences, volume 4, issue 6, 2011, page 2223. *Reproduced by permission of The Royal Society of Chemistry*. (http://dx.doi.org/10.1039/C1EE01131F) The experimental work builds on the computational work by Bo Xu and the STEM/EELS instrument was operated by Miaofang Chi.

The previous two chapters detailed the critical role of the synthesis conditions to determine the microstructure, morphology and surface characteristics, thereby influencing the electrochemical response of the layered lithium-excess nickel manganese oxides. We found that controlling the precursor chemistry prevents the formation of surface –OH groups significantly reducing the first cycle irreversible capacity. Furthermore post synthesis treatment using high pressures illustrated clear formation of a second phase and large amounts of interlayer cation migration. These changes would be expected to hinder the electrochemical properties; however, the material undergoes structural rearrangement during electrochemical cycling and can deliver capacities exceeding 200 mAh/g. Nevertheless, the large first cycle irreversible capacity still remained and increased with increasing pressure treatment. This illustrated that modifications within the bulk material using post synthesis treatment would not overcome the intrinsic irreversible capacity loss.

Much prior research has been devoted to address these two issues. The most promising approaches for reducing the irreversible capacity loss involve surface coating of the cathode surface with other oxides or fluorides like Al_2O_3, $AlPO_4$ and AlF_3. [35, 37] The exact mechanisms for the surface coating are still not well understood. Wu and Manthiram proposed that the reduction in irreversible capacity loss by surface coating was attributed to the retention of part of the oxygen ion vacancies in the lattice upon first charge. [37] Chapter 3 revealed that the reversible discharge capacity was affected by the surface characteristics of as-synthesized material. [89] Even without any coating, the first cycle irreversible capacity could be significantly reduced by controlling the precursor chemistry: If the surface adsorbed –OH group can be eliminated, the irreversible capacity is less than 40 mAh/g without any surface coating. [89] The low rate capability of the pristine material was proposed to be a possible result from the formation of a thick amorphous solid-electrolyte interface (SEI) on the surface of the material during oxygen loss on charging to 4.8 V.[109] The composition of the amorphous surface layer is undetermined.

Despite much work on this family of materials, a detailed understanding regarding the stability of the surface of the material is still lacking. In depth investigations are necessary to identify surface structural changes associated with the cation migrations in the *pristine* layered lithium-excess oxides. In this chapter, we carried out Synchrotron X-Ray Diffraction (XRD), aberration corrected Scanning Transmission Electron Microscopy (*a*-S/TEM) and Electron Energy Loss Spectroscopy (EELS) combined with electrochemical testing on $Li[Ni_xLi_{1/3-2x/3}Mn_{2/3-x/3}]O_2$ (x=1/5) compounds to identify how the surface and bulk changed after the first charge/discharge cycle. First principles computation was performed on the model compound $Li[Ni_xLi_{1/3-2x/3}Mn_{2/3-x/3}]O_2$ (x=1/4) to help guide the experimental investigations and better rationalize the highly complicated experimental observations.

5.1 Methodologies

5.1.1 Experimental

5.1.1.1 Electrochemistry

For the electrochemical charge/discharge at different C-rate and cycling experiments, cathodes were prepared as described in Chapter 2. Electrochemical impedance spectroscopy (EIS) measurements were carried out using a Solartron 1287 and Solartron 1260 frequency response analyzer system at room temperature with metallic lithium as the counter and reference electrodes in the frequency range of 10kHz to 10 mHz at an AC voltage of 10 mV. The cell voltage was potentiostatically stepped at 20 mV increments and held. The EIS measurement began at each held voltage when the measured current fell below a current of 10μA corresponding to a C/200 rate.

The samples for XRD and TEM were recovered by disassembling cycled batteries in an argon-filled glovebox as described in Chapter 2.

5.1.1.2 X-ray diffraction

Powder diffractions of all samples were taken using synchrotron x-ray diffraction at the Advanced Photon Source (APS) at Argonne National Laboratory (ANL) on beamline 11-BM ($\lambda = 0.4122$ Å). Cycled samples were hermetically sealed in 1.0 mm kapton capillaries to minimize air-exposure. The beamline uses a sagittally focused x-ray beam with a high precision diffractometer circle and perfect Si(111) crystal analyzer detection for high sensitivity and resolution. Instrumental resolution at high Q is better than $\Delta Q/Q \approx 2\times10^{-4}$, with a typical 2θ resolution of < 0.01° at 30 keV XRD data analysis was carried out by Rietveld refinement method using FullProf and GSAS/EXPGUI software. [93, 136, 137]

5.1.1.3 a-STEM/EELS

Electron Microscopy work was carried out on a Cs-corrected FEI Titan 80/300-kV TEM/STEM microscope equipped with a Gatan Image Filter Quantum-865. All STEM images and EELS spectra were acquired at 300KV and with a beam size of ~0.7Å. EELS spectra shown in this work were acquired from a square area of ~0.5*0.5nm with an acquisition time of 3secs and a collection angle of 35 mrad. HAADF images are obtained with a convergence angle of 30 mrad and a large inner collection angle of 65 mrad. To minimize possible electron beam irradiation effects, EELS and HAADF figures here are acquired from areas without pre-beam irradiation.

5.1.2 Computational Methods

The first principles calculations were performed in the spin-polarized GGA+U approximations to the Density Functional Theory (DFT). Core electron states were represented by the projector augmented-wave method[138] as implemented in the Vienna ab initio simulation package (VASP). [124, 125, 139] The Perdew-Burke-Ernzerhof exchange correlation [140] and a plane wave representation for the wavefunction with a cutoff energy of 450eV were used. The Brillouin zone was sampled with a dense k-points mesh by Gamma packing. The supercell is composed of twelve-formula units of $Li[Ni_{1/4}Li_{1/6}Mn_{7/12}]O_2$. The lattice shows a $R\bar{3}m$ layered structure. The atomic positions and cell parameters are fully relaxed to obtain total energy and optimized cell structure. To obtain the accurate electronic structures, a static self-consistent calculation is run, followed by a non-self-consistent calculation using the calculated charge densities from the first step. The cell volume is fixed with internal relaxation of the ions in the second step calculation. The Hubbard U correction was introduced to describe the effect of localized *d* electrons of transition metal ions. Each transition metal ion has a unique effective U value applied in the rotationally invariant LSDA+U approach. [141] The applied effective U value given to Mn ions is 5eV and to Ni ions is 5.96eV, consistent with early work on $LiNi_{1/2}Mn_{1/2}O_2$. [142]

5.2 Results

5.2.1 Electrochemical Properties

Electrochemical measurements of $Li[Li_{1/5}Ni_{1/5}Mn_{3/5}]O_2$ electrodes were performed in lithium half-cells cycled between 2.0 to 4.8 V. Figure 5-1A displays the voltage (V) versus capacity (mAh/g) electrochemical curves for $Li[Li_{1/5}Ni_{1/5}Mn_{3/5}]O_2$ in galvanostatic mode at C/50 for the first charge/discharge cycle. During the first charge step, the voltage in the cell increases monotonically until 4.4 V, and reaches a plateau region between 4.4 and 4.6 V. The discharge capacity of first cycle is 255 mAh/g, around 50 mAh/g less than the first cycle charge capacity. Figure 5-1B shows the capacity versus cycle number of $Li[Ni_{1/5}Li_{1/5}Mn_{3/5}]O_2$ electrodes. The material shows steady reversible cycling reaching capacities exceeding 200 mAh/g at C/50 and C/20 rates. Electrochemical impedance spectroscopy (EIS) was performed to study the change of impedance in the $Li[Li_{1/5}Ni_{1/5}Mn_{3/5}]O_2$/Li half cell as a function of the state of charge (SOC). Figure 5-2 compares the EIS spectra of the cell at 3.8, 4.0, 4.2, 4.4, 4.5 and 4.6 V. The impedance spectra were analyzed using physical processes that could be represented as a combination of resistive/capacitive elements. Due to the non-homogeneity of the composite electrode system reflected as depressed semicircles in the impedance response, constant phase elements are used in place of capacitors to model the data. The equivalent circuit in the insert of Figure 5-2 was used for fitting of the data. The cross points are experimentally measured data and the line is from the equivalent circuit fitting. Table 5-1 shows the values obtained from the equivalent circuit fitting of the electrolyte resistance, R_e, surface resistance, R_s and charge transfer resistance, R_{ct}. At low voltages, the figure exhibits two depressed semicircles at the high frequency regimes and a sloped line at low frequencies. The impedance spectra changes shape as the voltage increases. The size of the second lower frequency semicircle increases in diameter and the sloped line disappears as the voltage increases from 4.40 V to 4.60 V. The distinct regions on the figure represent separate time constants in the delithiation process. The first semicircle in the high frequency region is potential independent and represents the lithium ion diffusion across the electrode/electrolyte (solid/liquid) interface. The intercept of the first semicircle at the highest frequency with the real axis (Z_{re}) corresponds to the ohmic resistance originating from the electrolyte (R_e). The second semicircle in the middle frequency region is related to the charge transfer region between the surface film and the $Li[Li_{1/5}Ni_{1/5}Mn_{3/5}]O_2$ particle interface. The diameter of this second semicircle represents the charge transfer resistance (R_{ct}). At lower voltages (up to 4.4 V) and lower frequencies, a narrow Warburg region is followed by a sloped line. This region is attributed to solid-state diffusion of Li ions into the bulk cathode material.[143] Before the plateau region at 3.80, 4.00, 4.20 and 4.40 V, the surface resistance R_s reduces slightly, while the solid diffusion represented by the linear Warburg region and the charge transfer resistance remain relatively constant. Once the voltages reach the plateau region between 4.50 and 4.60 V, the surface resistances remain relatively constant, while the major changes in the spectra is dominated by a significant increase in the charge transfer resistance (R_{ct}). This trend is in contrast with other conventional layered transition metal oxide cathode materials (e.g. $LiCoO_2$) where R_{ct} was observed to decrease with the states of charge.[143, 144]

5.2.2 X-Ray Diffraction

Figure 5-3A shows X-ray diffraction pattern of pristine $Li[Li_{1/5}Ni_{1/5}Mn_{3/5}]O_2$. Rietveld refinement of the pristine phase is a typical well layered phase with 0.03 Li/Ni mixing. X-ray diffraction pattern of the material following 10 electrochemical cycles are also shown in Figure 5-3 and refined using a single $R\bar{3}m$ phase (Figure 5-3B) as listed in the inset table. The superlattice peaks between 20-30° observed in pristine materials disappeared in the cycled materials. Based on the capacities observed, the cycled material has 0.8 Li remaining in the structure. Compared to the pristine materials, a significant *c* lattice expansion is observed accompanied by an increased amount of Li/Ni interlayer mixing. The Rietveld refinement using a single layered phase provides reasonably good fitting based on the R_{wp} and R_b fitting factors; however, large mismatch of the (003) peak can be observed clearly as shown in the inset in Figure 5-3B. To correct this mismatch, a two-phase refinement including a second $R\bar{3}m$ phase was performed. The fitting pattern is shown in Figure 5-3C and the refinement results are listed in Table 5-2. Both of the layered phases show an expanded lattice, however one phase shows little Li/Ni interlayer mixing and the other layered phase shows increased Li/Ni mixing compared to the pristine material. The inset in Figure 5-3C shows significant improvement in fitting of the (003) peak based on two phases. Rietveld refinement included tetrahedral Li ions in one of the two layered phase was also performed and the results are listed in Table 5-3. R_{wp} and R_B fitting factors can be further reduced when ~13% tetrahedral Li ions are included. More details on the formation of tetrahedral Li will be discussed later.

5.2.3 a-STEM

Figure 5-4 and 5-5 depict electron microscopy data from the pristine sample and cycled sample (at the discharge state after 10 cycles between 2 to 4.8 V). The particles show a high degree of crystallinity and well faceted surfaces. Multiple grains were selected for study and the results are consistent, therefore only representative data are shown here. Images acquired by an HAADF detector with a small convergence angle and a relative large inner collection angle are also called “Z-contrast” images, where the contrast is proportional to $Z^{1.7}$.[145, 146] In atomic resolution Z-contrast images, the contrast of the atomic columns thus can be used to differentiate different elements and provide atomic-structural information.

Figure 5-4A is a typical Z-contrast image recorded along the [1 0 0] zone axis and Figure 5-4B shows a high magnification image from a selected area in Figure 5-4A. The arrays of atomic columns are clearly revealed. The atomic columns in the horizontal direction are separated by a distance of 4.3 Å, corresponding to the (100) projection of √3a superlattice in $R\bar{3}m$ layered structure; and 4.8 Å in the vertical direction, corresponding to 1/3 of typical *c* lattice in $R\bar{3}m$ layered structure. The zoomed-in image in Figure 5-4B clearly shows a pattern of two brighter columns followed by a darker column; such pattern is a direct result of the cation ordering in the TM plane: Two TM-rich columns (higher Z) and one Li-rich column (lower Z). An atomistic model is placed next to the HAADF image for clarity. The well layered properties in the bulk of the pristine material extend to the surface. Moreover, the stacking sequence of the ordered

TM layers along the (001) c-direction is random. Our observations are consistent with previous report on uncoated pristine $LiLi_{1/5}Ni_{1/5}Mn_{3/5}O_2$ material by Lei et.al.

Figure 5-5A shows traditional bright field images of the surface and bulk of the material following 10 electrochemical cycles recorded along the [1 0 0] zone axis. A 2-5 nm amorphous layer was observed on the surface of the material, which might be related to the side reaction of electrolyte at high voltage (>4.5 V). Detailed analysis of this layer will be discussed in a separated paper. The HAADF image in Figure 5-5B shows that the bulk of the grains still maintain the well layered structure as in seen in Figure 5-4. The surface structure of the cycled grains, however, is obviously changed based on the contrast change of the atomic columns. Along the (001) direction, the dark columns of bulk (Li atomic columns) become much brighter on the surface. In fact, their contrast is almost comparable to their neighboring TM columns. This suggests that a significant amount of transition metal ions migrate into the Li sites resulting in a loss of the layered characteristics at the surface of the materials.

5.2.4 EELS

Figure 5-6 compares the EELS spectra of the oxygen K-edge (top) and the manganese L_3 and L_2 edges from the surface and bulk of the pristine and cycled samples respectively (bottom). The fine structure and energy position of O-K and Mn-L edges imprints the electronic structure of the sample and thus can be used to study the structural evolution on the cycled surface. The energy position and fine structures of Mn-L edges are almost identical on the spectra from the pristine surface and bulk, and the cycled bulk. However, those from the cycled surface area slightly shift to a lower energy loss, which indicates a decreased oxidation state of Mn. This is also proved by its relatively higher L_3/L_2 ratio, which is a well-known indicator of oxidation state variations in transition metals.[63, 67] Fine-structure modifications of O-K edges are noticeable on the spectrum from the cycled surface compared to the other spectra. The first peak, at energy loss of ~532 eV almost vanished on the spectrum from the cycled surface. This O-prepeak can be attributed to the transition of 1s core state to the unoccupied O-*2p* states hybridized with TM-*3d* states. The decreased intensity of this peak on the cycled surface likely indicates the modification of unoccupied states of TM-*3d* and bonding lengths of TM-TM. These electronic structure changes correlate well with the atomic structure modification revealed by Z-contrast imaging. EELS quantification shows that O/Mn ratio variation among the cycled surface and bulk is less than 5%, which imply no significant oxygen losses in the cycled sample. In contrast, obvious Li loss (more than 50%) was found on the cycled surface, seen in Figure 5-7. This is consistent with the fact that significant TM atoms occupy Li site on the cycled surface, which is revealed by Z-contrast imaging (Figure 5-5).

5.2.5 First-Principles Calculations

The compound $Li[Ni_{1/4}Li_{1/6}Mn_{7/12}]O_2$ is modeled as a solid solution of Li_2MnO_3 and $LiNi_{0.5}Mn_{0.5}O_2$. For the convenience to interpret computation results, the formula of this compound will also be referred as $Li_{14/12}Ni_{1/4}Mn_{7/12}O_2$. There are four layers in each suprecell, two oxygen layers, one transition metal (TM) layer and one Li layer. Each layer is composed of twelve ions, forming a $2\sqrt{3}a_{hex.} \times 2\sqrt{3}a_{hex.}$ in-plane supercell. Oxygen ions are close-packed and stacked in ABC (O3) stacking, serving as the frame, while TM slab and Li slab stack alternatively.. In the model with the lowest energy, Li layer supercell is composed of 12 Li ions (Figure 5-8B) and the in-plane cation ordering of the TM layer is shown in Figure 5-8A. There are two “excess” Li ions located in the TM layer, one Li ion is surrounded by 6 Mn ions and the other Li ion is surrounded by 5 Mn ions plus 1 Ni ion. The Ni ions are arranged in the “broken zigzag” shape. In this model the cation arrangements are most consistent with experimental observations including NMR[147], electron diffraction[21] and x-ray diffraction and is used as the basis to investigate the lithium de-intercalation mechanism of the materials. Although the models we propose here are all solid-solutions of Li_2MnO_3 and $LiNi_{0.5}Mn_{0.5}O_2$, phase separations may happen. The mixing energy calculated by following equation is around +40 meV per formula. Note that in the synthesis of this series of materials, 900-1000 °C heating temperature is used, that very likely overcomes a small positive mixing energy.

$$\Delta E_{mixing} = E_{Li[Ni_{1/4}Li_{1/6}Mn_{7/12}]O_2} - 0.5 \times (E_{Li_2MnO_3} + E_{LiNi_{0.5}Mn_{0.5}O_2}) \quad (5\text{-}1)$$

The formation enthalpy of $Li_{n/12}Ni_{1/4}Mn_{7/12}O_2$ ($8<n<14$) versus lithium concentration is calculated with two reference states set as n=8 and n=14 (Figure 5-8C). When n=8, all Ni ions are oxidized to the highest valence state. Further removal of Li ions beyond this critical lithium concentration will result in the additional capacities related to non-redox centers. The calculated voltages, (shown in red line in the inset of Figure 5-8C) ranging from 3.86 V to 4.48 V, match well with the experimental measurements of the 1st cycle charging voltage (shown in black line in the inset of Figure 5-8C). At each concentration, various Li-vacancy configurations are calculated and those with the lowest energies are depicted by red crosses in Figure 5-8C. These configurations usually involve tetrahedral Li ions (Li_{tet}) formed in the Li layer. Structures of Li_{oct}-vacancy configurations are also investigated and the most stable configurations are depicted by the green dots. Below certain lithium concentrations ($n<11$), however, these configurations usually have higher energies. The blues stars in Figure 5-8C depict the structures based on a defect spinel model as illustrated in Figure 5-9 In the defect-spinel model, the Li layer supercell is composed of 11 Li ions with 1 Ni ion, and the TM layer in-plane cation ordering is shown in Figure 5-9A. When n=14, the TM ions in the TM layer are arranged following the Mn lattice in [111] plane of spinel $LiMn_2O_4$ illustrated in Figure 5-9B. Therefore, when n=8, the formula of the compound $Li_{2/3}Ni_{1/4}Mn_{7/12}O_2$ can be re-written as $Li[Li_{1/3}Ni_{1/2}Mn_{7/6}]O_4$, forming a lithium-excess defect-spinel phase where part of the *16d* octahedral sites are occupied by Li ions (Figure 5-9C). In a perfect spinel phase, only transition metal ions reside on *16d* sites. At fully lithiated state (n=14), the formation enthalpy of this defect-spinel phase is +105 meV and at x=8 the formation enthalpy of this phase is -101 meV with respect to the corresponding layered form.

Calculations of electronic structures are performed on $Li_{n/12}Ni_{1/4}Mn_{7/12}O_2$ at (0<n<14). For n < 8, structures are modeled without introduction of oxygen vacancies. The valences of TM ions are estimated from the calculated TM magnetizations. The electron configurations of TM ions within octahedral ligand fields are shown in Figure 5-10 insets. In Figure 5-10, the average of Ni and Mn magnetizations are plotted versus lithium concentration. For Mn ions, the average magnetization retained is 3.1 μ_B per ion when n>8, consistent with a high spin Mn^{4+}. It increases slightly to 3.4 μ_B per ion when n<8, mainly due to the significant charge redistribution around oxygen ions. Careful inspection of the projected density of the state in Figure 5-11 of Mn ions confirm that the valence state of Mn is unchanged as 4+. For Ni ions, the average magnetizations reduces from 1.7 μ_B per ion to 0.4 μ_B per ion when n>8. This is expected as all high spin Ni^{2+} ions are oxidized to low spin Ni^{4+}, which has been seen experimentally. [22] When n <8, the average Ni magnetizations fluctuates around 0.5 μ_B. It suggests that the valence of Ni ions remains unchanged. The valence of oxygen ions can also be investigated qualitatively from the change of spin distribution over oxygen layer. Three different states of charge are shown in Figure 5-12. For clarity, in Figure 5-12A part of the oxygen layers of $Li_{n/12}Ni_{1/4}Mn_{7/12}O_2$ supercell is presented by the pink balls together with the adjacent TM slab. The corresponding spin density of this region at n=14, 8, and 0, are presented respectively in Figure 5-12B, C, and D. Though the plane cut through oxygen layer, positive spin density of Ni and Mn ions can still be observed partially. At full lithium concentration (n=14), well bonded oxygen *2p* electrons can be clearly observed in Figure 5-12B. However, the shape of oxygen *2p* electron clouds begins to distort at lower lithium concentration (n=8, Figure 5-12C), suggesting a potential change of oxygen valence. At n=0 (Figure 5-12D), the spin distribution around oxygen ions change significantly. The spin densities of Mn ions also increase slightly, possibly due to weakening of Mn-O bonding, which is consistent with the change of Mn magnetization as described above. Note that no oxygen vacancies are allowed in current models. The above results indicate that during the charging stage, the extra electrons that cannot be provided by the Ni redox couples are coming from oxygen ions.

5.3 Discussion

The choice of composition for first principles computation is primarily limited by the size of supercell that is reasonable with modern computation resources. So far we have presented all experimental characterization on $Li[Ni_{1/5}Li_{1/5}Mn_{3/5}]O_2$, previous reports and our study on other compositions have proven that the lithium-excess layered oxide, $Li[Ni_xLi_{1/3-2x/3}Mn_{2/3-x/3}]O_2$ ($0 \leq x \leq 1/2$) series show similar behavior before, during and following electrochemical cycling. [19, 89, 109] Therefore the results from both computations and experimental characterizations could be combined to understand the structural and electrochemical properties of this material series from various aspects. The combined results allow us to present an alternative Li de-intercalation mechanism in the lithium-excess layered oxides.

There are two distinct regions in the delithiation process. The initial charging region is before the plateau region when the voltage is less than 4.45 V or the amount of Li is greater than 0.8 per formula. The second step is when the voltage is in the plateau region greater than 4.50 V and the concentration of Li^+ ions is less than 0.8 per formula. For the convenience of general discussion, $Li_{\delta}Ni_{1/5}Mn_{3/5}O_2$ is taken as the example and discussed in following sections.

5.3.1 Initial Stage Of Lithium Deintercalation (Voltage Up To 4.45 V; $0.8 < \Delta < 1.2$)

First principles calculations suggest that a solid solution behavior exists in this region of the delithiation process consistent with previous experimental work. [89] The Li is continuously extracted from the material, which is depicted by the electrochemical curve as a sloping region from the open circuit voltage to 4.45 V. This region provides 120 mAh/g capacity (0.4 Li per formula unit) and the charge compensation originates from the Ni ions which is consistent with previous x-ray absorption spectroscopy results showing that the Ni^{2+} ions are oxidized to Ni^{4+}. [22] Both the Mn^{4+} and O^{2-} valences are not changed during this region. The computation results predict that lithium will migrate into tetrahedral sites. This process is illustrated in Figure 5-13. Initially the Li^+ ions are removed from the Li layer first seen in Figure 5-13A. The energy of removing one Li per cell from Li layer is more than 300 meV lower than that from TM layer. The Li ion in the transition metal layer (Li_{TM}) is edge-sharing with three octahedral Li ions (Li_{oct}) in the adjacent Li layer. When these edge-sharing Li_{oct} ions are extracted, a Li^+ ion will migrate from the octahedral site into the tetrahedral site, as shown in Figure 5-13B, face-sharing with Li in the TM layer. During this process, the Li in the TM layer will migrate to the shared tetrahedral site in the opposite site forming a Li-Li dumbbell (Figure 5-13C) and the total energy of the structure is further reduced. On the other hand, TM ions in the structure may be able to diffuse following similar ways as Li diffusion. Preliminary calculations give the hints that under certain circumstances, Ni^{2+} ($t_{2g}^6e_g^2$) may migrate from one octahedral site to another adjacent octahedral site through an empty tetrahedral site, with relatively low energy barriers at the beginning of the charge state. Ni ions therefore may diffuse out of the TM layer, diminishing the ordering contrast in the TM layer, and diffuse into the Li layer, increasing the Li/Ni interlayer mixing.

5.3.2 Second Stage Of Lithium Deintercalation (Plateau Up To 4.8 V; $0.2 < \Delta < 0.8$)

In the electrochemical voltage profile, a plateau region exists between 4.4 V and 4.6 V indicating a two-phase reaction. As suggested by first principles calculations, during this region, the remaining Li^+ ions in the octahedral sites are extracted from the Li layer, while the tetrahedral Li-Li dumbbells are very stable and need voltages exceeding 5.0 V to be removed. Therefore these Li-Li dumbbells may never be removed during the first cycling up to 4.8 V, blocking the empty sites in the TM layer, therefore may partially cause the irreversible capacity during the first cycle. EELS spectra of Li edge (Figure 5-7) indicates that the surface has only about half of the Li concentration as the bulk even at the fully discharged state. The tetrahedral Li that remained in the structure combined with the TM ions migrating into the Li layer can facilitate the formation of the proposed spinel-like phase which has an extremely low energy at low lithium concentration regions (high voltage region). Such a second phase may be generated near the surface of the material. The electrochemical impedance data (Figure 5-2) shows that the resistance at the interface between the surface layer and the pristine particles dramatically increases especially at high voltages. Such resistance increase may partly be due to the generation of the two phase boundary between the bulk materials and the surface phase. As certain amount of TM ions are now in the Li layers near the surface, as shown by *a*-STEM Z-contrast images (Figures 5-4 and 5-5) as well as Rietveld refinement of XRD (Figure 5-3), the original Li diffusion planes are populated with high density of TM ions, and the general Li mobility of the material at high voltage (low lithium concentration) is negatively affected. With this specific surface phase structural change, the materials therefore exhibit inferior rate capabilities. Our first principles data, as well as the synchrotron XRD data suggest the formation of tetrahedral Li; however X-ray diffraction is insensitive to Li ions; therefore, the absolute amount of Li present in the tetrahedral layer is still uncertain.

The charge compensation mechanism may originate from the oxygen ions as previously explored with the activation of the Li_2MnO_3 region.[18, 32] Mn-O bonding is weakening due to the change of the oxygen charge densities, resulting in Mn-O distortions. Typically Mn^{4+} has the t_{2g}^3 electron configuration and MnO_6 octahedrons are highly stable. Such distortion will lead to significant change in the bonding characteristics of Mn-O. EELS observations clearly show that the valence of Mn ions near the surface (about 2-5nm thick) has been reduced from 4+ and oxygen pre-peak diminished. More careful study on the impact of Mn-O distortions and the possibility of oxygen vacancy formations will be helpful.

Based on the combined experimental and computational results presented, we can conclude that permanent changes occur at the surface of the Li excess layered materials during the initial charging cycle. A new defect-spinel solid phase is formed on the surface of the electrode materials after high-voltage cycling. An atomistic model for such a spinel-like phase is proposed for the first time. We believe that such a surface phase transformation may be part of the sources contributing to the first cycle irreversible capacity and the main reason for the intrinsically poor rate capability of these materials. The surface phase developed in this series of materials following electrochemical cycling is 2-5nm thick on the surface making it difficult to identify. Characterization of the surface is equally difficult because the oxygen framework remains the same but changes in the transition metal layers and lithium layers appear. The results from this work required the use of sophisticated techniques such as atomic resolution STEM and EELS with high spatial resolution. The atomic contrast STEM images can be used to identify changes in the stacking and ordering within the material while the EELS analysis complements the STEM results with quantifiable changes. The combination of the two techniques provides strong evidence for the growth of a surface layer on the lithium-excess series of materials. Such surface structural change may lead to a phase transformation from layered structure to defect-spinel structure at the surface of the materials. The large irreversible capacity after cycling and the low rate capability of the materials are therefore partially attributed to this surface phase transformation.

Table 5-1. Fitting parameters for the equivalent circuit model represented in Fig. 5-2 applied to the electrochemical impedance (EIS) curves recorded between 3.80 V and 4.60 V

Voltage	R_e	R_s	R_{ct}
3.80 V	11.3	63.0	245.0
4.00 V	11.4	49.9	284.2
4.20 V	11.4	40.6	254.4
4.40 V	11.7	38.4	319.4
4.50 V	13.2	44.1	552.7
4.56 V	13.0	39.2	713.3
4.60 V	12.9	36.7	925.5

Table 5-2. Two phase Rietveld refinement results for discharged $Li[Ni_{1/5}Li_{1/5}Mn_{3/5}]O_2$ following 10 electrochemical cycles using two $R\bar{3}m$ phases

Atom	Site	Positions			Occupancy
Ni1	3a	0	0	0	0.104(1)
Ni2	3b	0	0	0.5	0.096 (1)
Mn1	3a	0	0	0	0.600
Li2	3b	0	0	0.5	0.696 (1)
Li1	3a	0	0	0	0.104 (1)
O	6c	0	0	0.2576(1)	2.000
Phase Fraction 55.1(4)%					
a_{hex}: 2.8758(1) Å		c_{hex}: 14.3750(2) Å		c/a: 4.999	$R\bar{3}m$
Atom	**Site**	**Positions**			**Occupancy**
Ni1	3a	0	0	0	0.178(1)
Ni2	3b	0	0	0.5	0.022(1)
Mn1	3a	0	0	0	0.600
Li2	3b	0	0	0.5	0.771(1)
Li1	3a	0	0	0	0.029(1)
O	6c	0	0	0.258	2.000
a_{hex}: 2.8763(1) Å		c_{hex}: 14.3225(2) Å		c/a: 4.999	$R\bar{3}m$
Conventional Rietveld Reliability Factors: R_{wp}: 7.33% R_b: 4.04%					

Table 5-3. Two phase Rietveld refinement results for discharged $Li[Ni_{1/5}Li_{1/5}Mn_{3/5}]O_2$ following 10 electrochemical cycles including one phase with Li on the (*1/3, 2/3, z*) tetrahedral site

Atom	Site	Positions			Occupancy
Ni1	3a	0	0	0	0.121(1)
Ni2	3b	0	0	0.5	0.079(1)
Mn1	3a	0	0	0	0.600
Li2	3b	0	0	0.5	0.721(1)
Li1	3a	0	0	0	0.079(1)
O	6c	0	0	0.2572(1)	2.000

Phase Fraction 60.1(3)%

a_{hex}: 2.8760(1) Å c_{hex}: 14.3757(1) Å c/a: 4.999 $R\bar{3}m$

Atom	Site	Positions			Occupancy
Ni1	3a	0	0	0	0.151(1)
Ni2	3b	0	0	0.5	0.047(1)
Mn1	3a	0	0	0	0.600
Li2	3b	0	0	0.5	0.618(1)
Li1	3a	0	0	0	0.047(1)
Li_{TET}	6c	0.333	0.667	0.7987(1)	0.135(1)
O	6c	0	0	0.2582(3)	2.000

a_{hex}: 2.8766(1) Å c_{hex}: 14.3234(2) Å c/a: 4.979 $R\bar{3}m$

Conventional Rietveld Reliability Factors: R_{wp}: 7.12% R_b: 3.68%

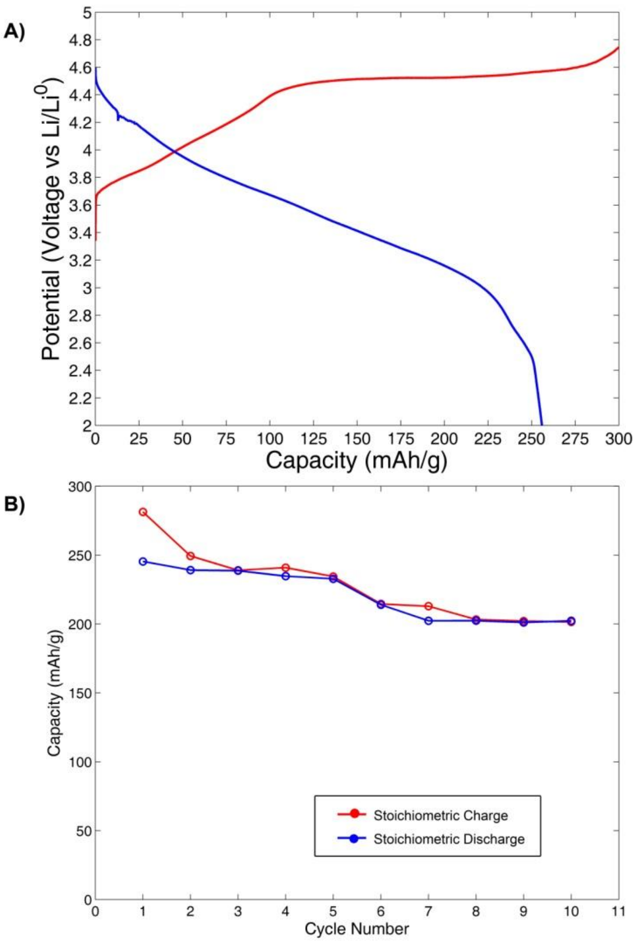

Figure 5-1. Electrochemical profile of $Li[Ni_xLi_{1/3-2x/3}Mn_{2/3-x/3}]O_2$ (x=1/5) showing A) the first cycle voltage profile versus capacity using a voltage window of 4.8 – 2.0 V. B) The capacity versus electrochemical cycle where the first 5 cycles correspond to a C/50 rate and cycles 6-10 correspond to a C/20 rate.

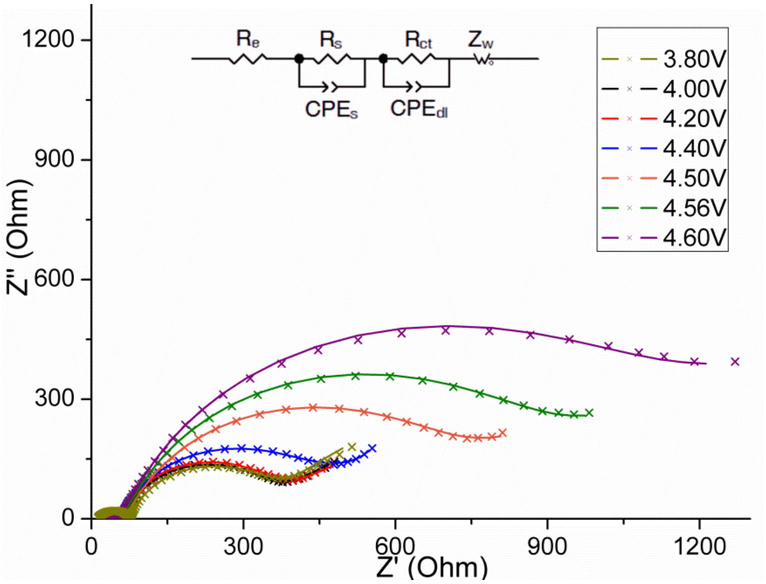

Figure 5-2. Experimental observations (marked by X) of electrochemical impedance spectroscopy (EIS) of Li[$Ni_{1/5}Li_{1/5}Mn_{3/5}$]O_2 during the first electrochemical charging cycle at different states of charge(SOC) The equivalent circuit model in the inset was used to fit the experimental model and plotted as a line at different SOC.

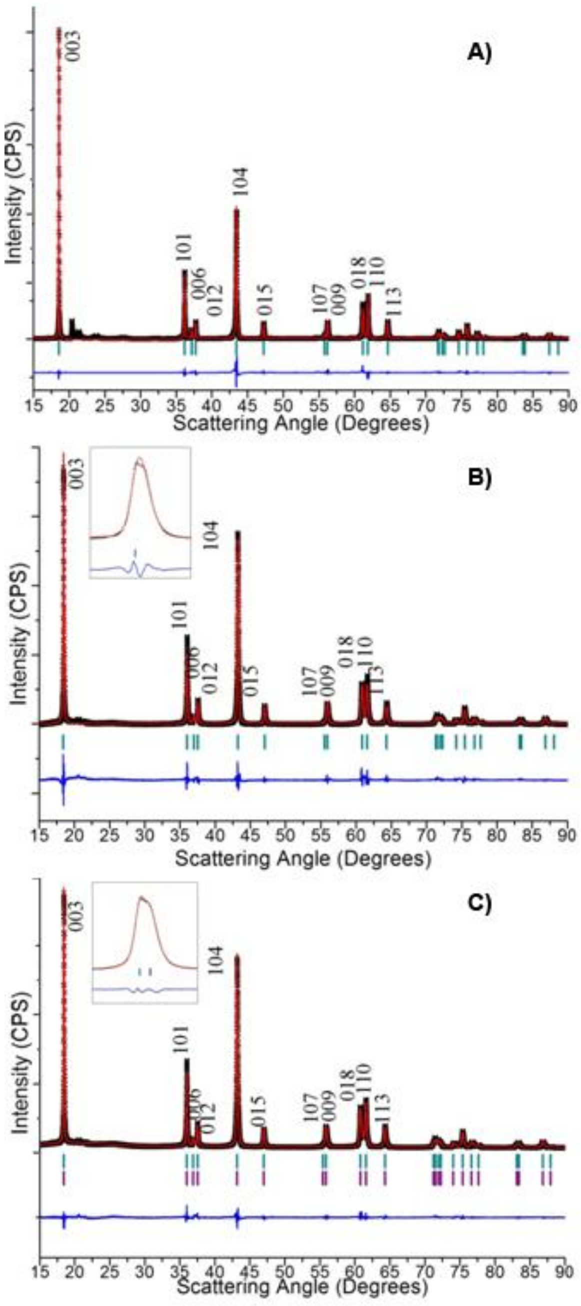

Figure 5-3. Comparison of the Rietveld refinement results from synchrotron X-ray diffraction patterns collected from $Li[Ni_{1/5}Li_{1/5}Mn_{3/5}]O_2$ A) before 10 electrochemical cycles and B) following 10 electrochemical cycles using one $R\bar{3}m$ phase and C) following 10 electrochemical cycles using two $R\bar{3}m$ phases. The black crosses represent the observed pattern, the red line corresponds to the calculated diffraction pattern and the blue is the difference pattern. In this and subsequent figures, the 2θ values are converted to those corresponding to a Cu Kα wavelength (λ=1.54 Å)

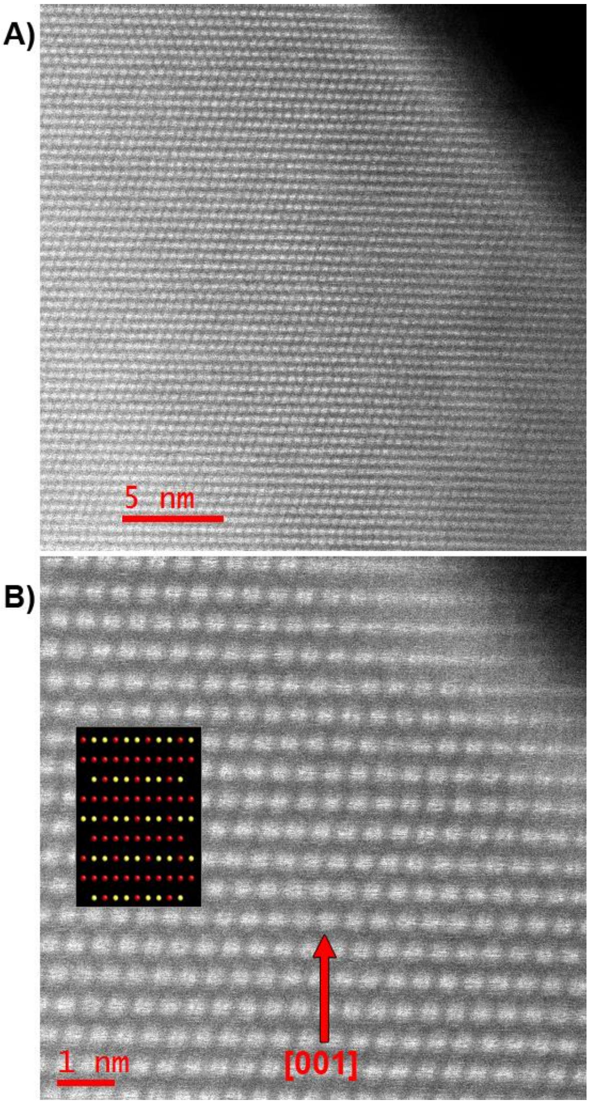

Figure 5-4. High resolution S/TEM images of the bulk and surface of pristine $Li[Ni_{1/5}Li_{1/5}Mn_{3/5}]O_2$ taken at A) low magnification and B) high magnification along [100] . The insert in B) is a schematic representation of the Li ions (red) and transition metal ions (yellow) showing the cation ordering and stacking along the c_{hex} axis

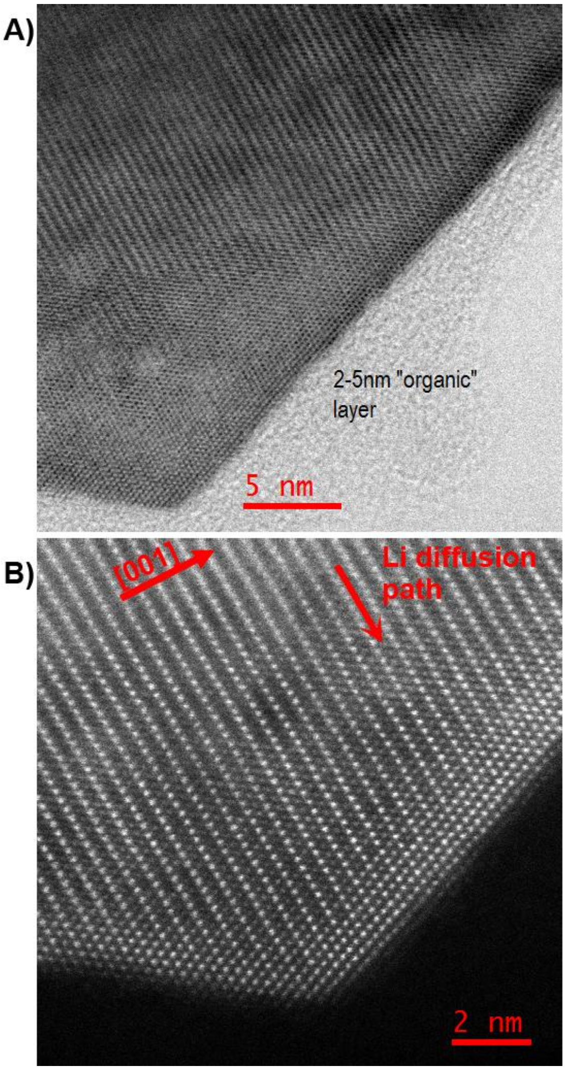

Figure 5-5. Examination of the bulk and surface regions of the electrochemically cycled $Li[Ni_{1/5}Li_{1/5}Mn_{3/5}]O_2$ using A) high resolution S/TEM imaging and B) corresponding HAADF imaging along the [110] zone axis

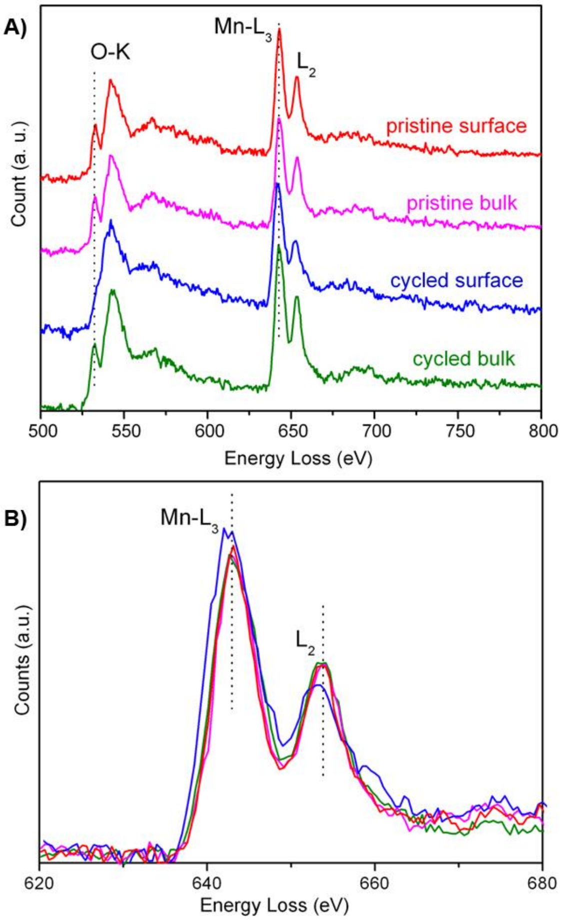

Figure 5-6. Representative EELS spectra from the surface and bulk of the pristine and electrochemically cycled Li[$Ni_{1/5}Li_{1/5}Mn_{3/5}$]O_2 material showing the A) O K-edge and A) and B) Mn L-edge

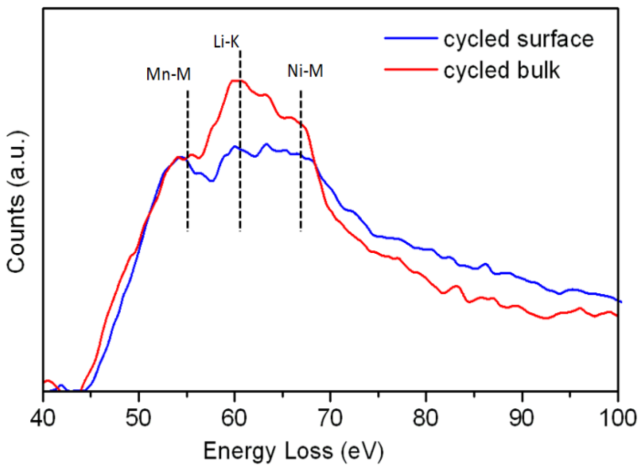

Figure 5-7. Comparison of Li-K edges from the surface and bulk in the cycled material. Obvious Li signal drop was observed on the spectrum from the surface area compared to that from bulk, although Li-K edge overlaps TM-M edges. Dotted lines mark the main peak position of Li-K and TM-M edges.

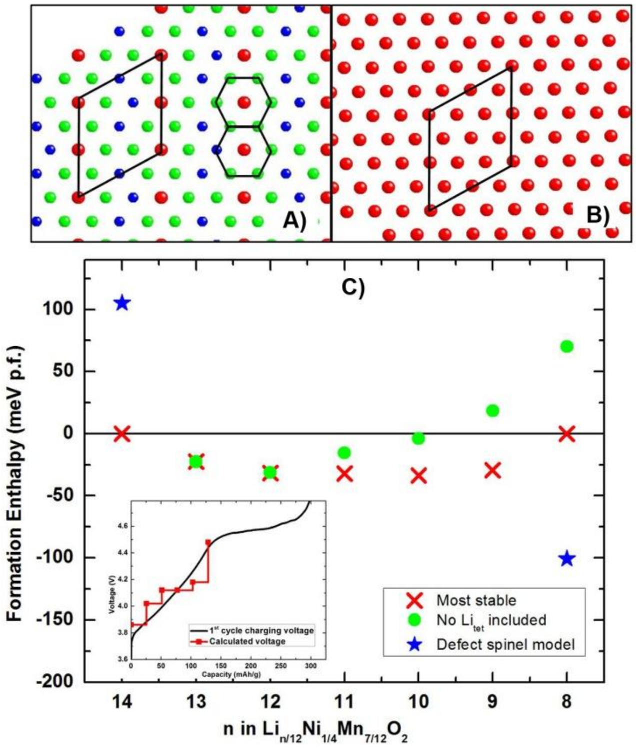

Figure 5-8. The cation in-plane ordering of $Li[Ni_{1/4}Li_{1/6}Mn_{7/12}]O_2$ showing A) the transition metal layer and B) the lithium layer (Red: Li; Green: Mn; Blue: Ni) C) Calculated voltage and formation enthalpy of $Li_{x/14}Ni_{1/4}Mn_{7/12}O_2$ (8<x< 14) versus lithium concentration

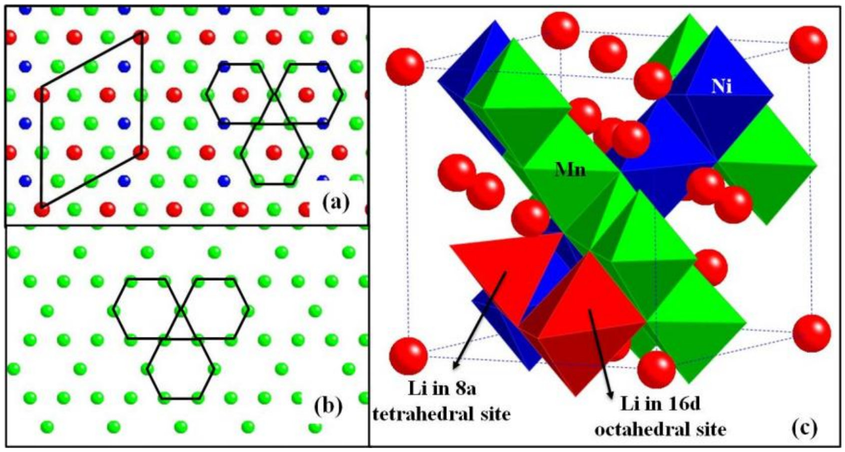

Figure 5-9. The defect-spinel model of Li[$Ni_{1/4}Li_{1/6}Mn_{7/12}$]$O_2$ showing A) the transition metal layer, B) the lithium layer and C) the Li[$Li_{1/3}Ni_{1/2}Mn_{7/6}$]O_4, lithium-excess defect-spinel phase.

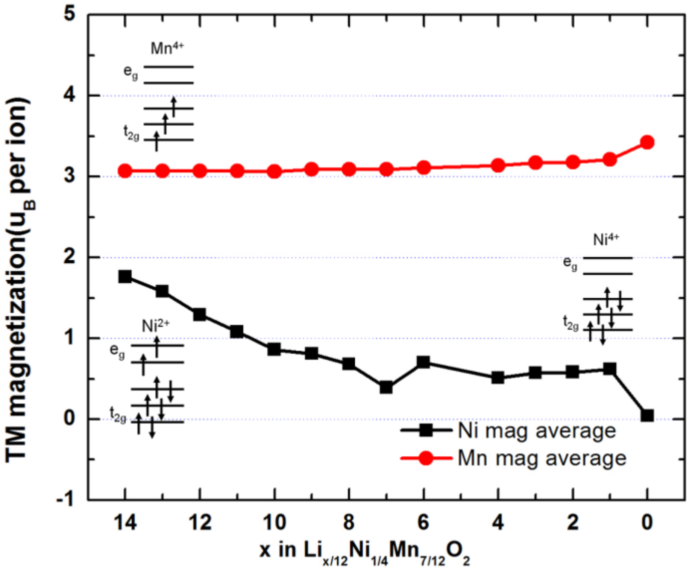

Figure 5-10. Calculated magnetization of Ni and Mn ions versus lithium concentration

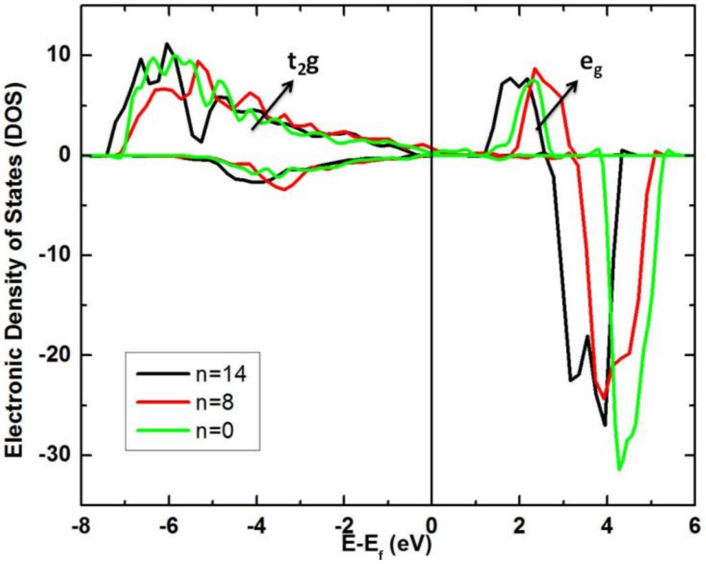

Figure 5-11. calculated projected DOS of Mn ions in $Li_{n/12}Ni_{1/4}Mn_{7/12}O_2$ with three different charging state, n=14 (black), n=8 (red) and n=0 (green).

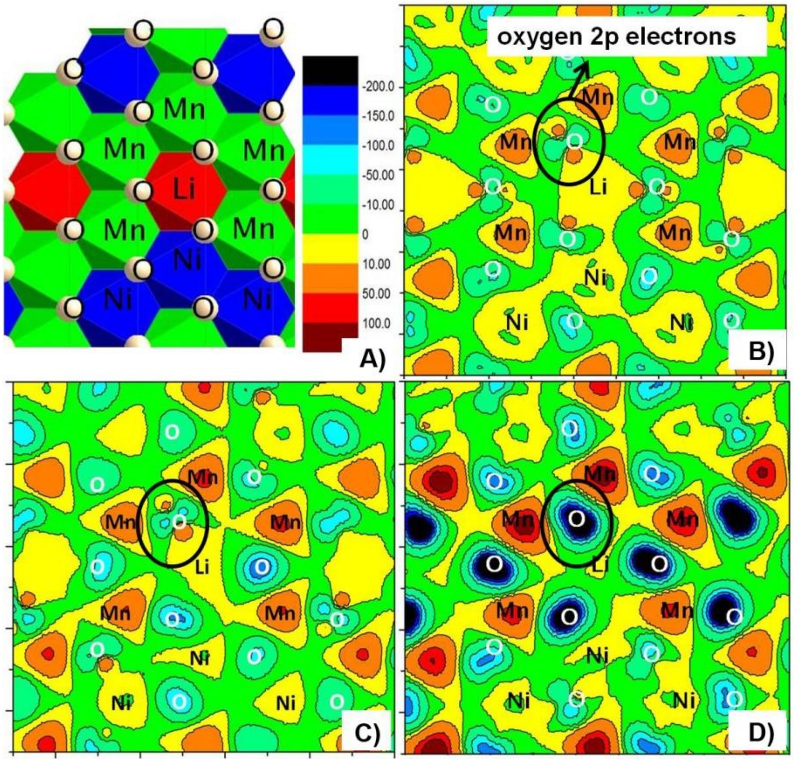

Figure 5-12. A) Sketch of partial oxygen layer in $Li_{x/14}Ni_{1/4}Mn_{7/12}O_2$ and its calculated spin density at B) x=14 C) x=8 and D) x=0.(Pink balls: oxygen ions; Colored polyhedrons: adjacent TM slab)

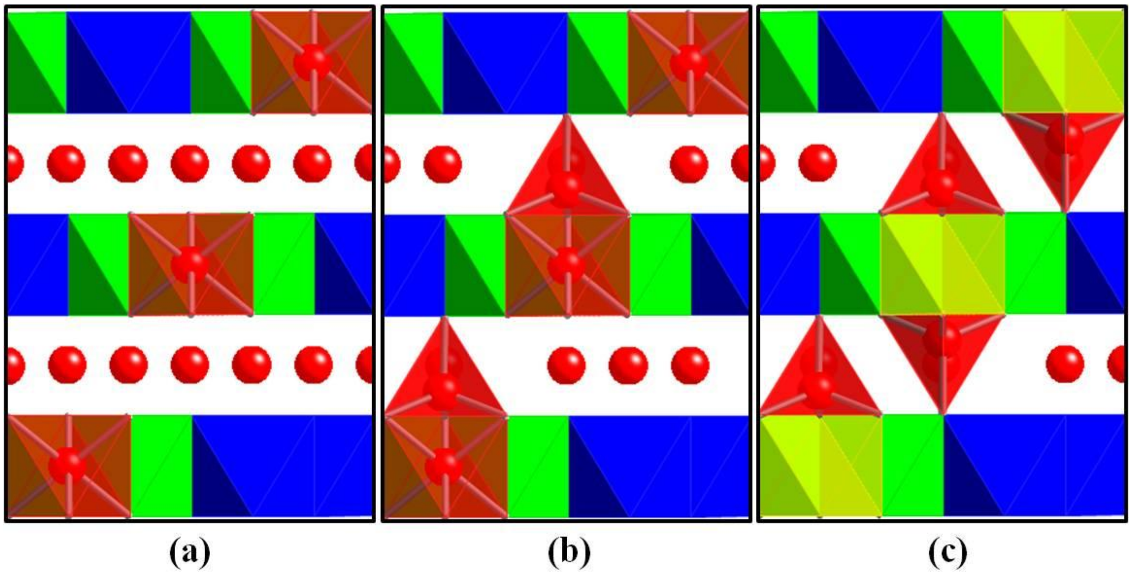

Figure 5-13. Sketch of Li-Li dumbbell formation in $Li_{x/14}Ni_{1/4}Mn_{7/12}O_2$ (Red:Li; Green:Mn; Blue:Ni; Yellow: Vacancy) at A) x=14, B) x=11 and C) x=8

CHAPTER 6

IN SITU X-RAY DIFFRACTION STUDY OF THE LITHIUM-EXCESS LAYERED OXIDE COMPOUND $LI[LI_{0.2}NI_{0.2}MN_{0.6}]O_2$ DURING ELECTROCHEMICAL CYCLING

This chapter is part of the paper: "*In Situ* X-ray Diffraction Study of the Lithium Excess Layered Oxide Compound $Li[Li_{0.2}Ni_{0.2}Mn_{0.6}]O_2$ During Electrochemical Cycling" by Christopher R. Fell, Miaofang Chi, Ying Shirley Meng and Jacob L. Jones.; Solid State Ionics, Volume 207, Issue 44, 2012, page 44. *Reproduced with permission from Elsevier*. The STEM microscope was operated by Miaofang Chi.

Chapters 3, 4, and 5 detailed the complexity of the interface in the lithium-excess layered transition metal oxides and the structural interface changes following electrochemical cycling. These studies were conducted *ex situ* and identified the structural changes *after* the electrochemical processes. The use of *in situ* techniques can identify when and how fast the changes occur.

There have been great efforts to observe the detailed structural changes that occur in the bulk and at the surface of the layered Li excess family of materials during the charging and discharging processes. The advantage of *in situ* x-ray diffraction lies in the ability to directly monitor detailed structural changes in the electrode material as Li extraction/insertion proceeds. The *in situ* x-ray measurement, combined with electrochemical measurements provides valuable information about the relationship between structure and electrochemical properties which is not obtainable from *ex situ* structural measurements. [26, 148-150] The layered Li excess compounds have not been extensively studied using *in situ* x-ray diffraction. Previous experiments by Lu and Dahn have explored changes in volume and lattice parameters showing the collapse in the *c* lattice parameter during the first charge cycle leading to a modified structure following the first discharge cycle. [26] However, the use of peak profile analysis to reveal the microstructure change of these materials has not been quantitatively done.

In situ x-ray diffraction using a laboratory diffractometer equipped with a curved position sensitive detector is a powerful technique to probe changes to the structure during the first charge and discharge cycle. These changes are linked to the structural model to illustrate significant strain contributions developing during the first electrochemical cycle profile.

6.1 Experimental Method

6.1.1 Sample Synthesis And Cathode Preparation

$Li[Ni_xLi_{1/3-2x/3}Mn_{2/3-x/3}]O_2$ (x=1/5) powders were prepared by the mixed hydroxide method as previously explained in Chapter 3.

Plastic-like peelable cathode electrodes were designed for use in the *in situ* electrochemical experiment. 51.6 wt.% active material is intimately mixed with 31.8 wt.% polyvinyl difluoride (PVDF) and 16.6 wt.% acetylene black. This mixture was added to an adequate amount of acetone to sufficiently dissolve the polymer and make a uniform slurry. The slurry was then tape cast onto a sheet of Mylar film to obtain an even thickness of 0.66 mm. Following acetone evaporation, the films were peeled off of the sheet and punched into circular disks with a diameter of 12 mm. The punched electrode disks were dried at 80°C in vacuum overnight.

6.1.2 *In situ* Electrochemical X-Ray Diffraction

In situ XRD of the electrochemical cells was performed using an INEL CPS120 diffractometer (INEL) in reflection geometry. The diffractometer is equipped with a curved position sensitive (CPS) detector, a Cu X-ray tube source, and multilayer mirror optics for increased incident intensity. A Bio-Logic SP-150 potentiostat was used to electrochemically cycle the cell under constant charge and discharge currents corresponding to a rate of C/50 between the desired potential limits 2.25 V and 4.85 V. An XRD pattern was measured every 7 minutes equivalent to 0.5 mAh/g during electrochemical cycling.

The *in situ* electrochemical cell was assembled in an argon glovebox with a lithium metal anode, a Celgard model C480 separator (Celgard Inc, USA) and a 1M $LiPF_6$ in a 1:1 volume ratio of ethylene carbonate to dimethyl carbonate (Ferro) electrolyte. The cathode and separator were pre-soaked in electrolyte to eliminate excess liquid in the cell to maximize X-ray diffraction signals. The positive current collector of a standard 2032 coin cell was punched with a 9.5 mm diameter hole window for the *in situ* electrochemical measurements. A 0.03 mm thick sheet of Kapton film was adhered over the window using Loctite 11C Hysol Resin and Loctite EPKC Hysol hardener and dried in air at 60°C overnight. A spring washer was added between the cathode and the positive current collector of the coincell to prevent direct contact with the kapton film and establish electrical contact.

6.2 Results And Discussion

6.2.1 *In situ* X-Ray Diffraction

To elucidate when changes in the $Li[Li_{0.2}Ni_{0.2}Mn_{0.6}]O_2$ structure occur during the first electrochemical cycle, *in situ* X-ray diffraction (XRD) experiments are carried out under constant current charge/discharge. The electrochemical properties as well as the structural parameters of the as-synthesized material have been characterized and the results are reported elsewhere. [89] The electrochemical properties of the *in situ* cell compare favorably to a coincell prepared without a kapton window (standard configuration) displaying the characteristic sloping region up to 4.45 V, a plateau region at 4.5 V and a charging capacity exceeding 250 mAh/g. Upon discharge, a large polarization was observed in the *in situ* cell; therefore the discharge capacity achieved was 155 mAh/g instead of the 200 mAh/g capacity in a standard coin cell. [19, 89] The electrochemical data presented in this study is represented as voltage versus time to correlate with the time resolved XRD patterns. The cell was cycled with a constant current corresponding to a C/50 rate between 2.25 V and 4.85 V.

Figure 6-1 shows several specific XRD peaks evolution versus time. The electrolyte present in the cell reduced the beam intensity, increased background intensities at low angles. Therefore, low angle peaks were not used for quantitative analysis in the present study. Peaks were fit using a Pearson VII type profile shape function and the 2θ peak center positions are shown versus time in Figure 6-1. The decrease in intensity during the discharge region originates from electrolyte interfering with the beam and does not originate from changes in the material. Figure 6-2 shows the changes in lattice parameters calculated with Rietveld refinement using Fullprof software [93] during the first electrochemical cycle. The *c* lattice parameter increases during the sloping region, then decreases dramatically during the plateau region. During discharge, the lattice parameters increase to values larger than observed in the pristine material. These results follow the same trends of previously published literature. [26] Returning to Figure 6-1, the peak positions for the (101), (104) and (110) peaks increase monotonically during the sloping region to 4.50 V corresponding to the Ni^{2+}/Ni^{4+} redox region. [22] As Li^+ is being removed from the layered structure, Ni ions oxidize from Ni^{2+} to Ni^{4+}, during which the ionic radius decreases from 0.69 Å to 0.48 Å. [25] During this region the material behaves like a solid solution as Li^+ is removed from

$Li_{1.2-x}Ni_{0.2}Mn_{0.6}O_2$ based on steady monotonic increases in peak position. Once the electrochemical profile reaches the plateau, the magnitude of the peak position shifts becomes minimal and remains at the largest 2θ values. The three peaks of (101), (104) and (110) increase by 0.18°, 0.14° and 0.35° respectively during the sloping region and only increase 0.05° during the plateau region to their maximum values when the corresponding charging capacity reaches 200 mAh/g. The material does not show evidence of degradation of the pristine phase during the first charging step. Upon discharge the (101), (104) and (110) peak positions consistently decrease in their 2θ position, though do not return to the original positions. The *c* lattice parameter increases from a minimum value of 14.169 Å at the end of the first charge to 14.311 Å after the first discharge. Similarly, the *a* lattice parameter increases from 2.840 Å at the end of the first charge to 2.855 Å following discharge. The fully discharged material loses 100 mAh/g capacity which corresponds to approximately 0.27 mol of Li^+ irreversibly lost from first discharge. Irreversible capacities previously reported range between 50 and 100 mAh/g in this material [18, 89], which is in good agreement to that observed in the current study. The final shifts in peak positions are consistent with the permanent changes to the crystal structure resulting from dynamic cation migration during electrochemical cycling. The permanent shifts in the peak positions supports previously reported results that the superstructure peaks dramatically decrease following electrochemical cycling and the c/a lattice ratio expands.[89, 109]

During the first electrochemical cycle, the (108) plane remains unchanged and predominantly corresponds to the out-of-plane ordering, which intersects 1 in every 8 transition metal (TM) or Li^+ layers (along the c_{hex} axis) as seen in Figure 6-3A. The out-of-plane ordering shows changes corresponding strongly to the *c* lattice parameter. As *l* increases in the (10*l*) family of peaks, the two theta peak position shift decreases in magnitude. Figure 6-3B shows the (110) plane illustrating the in-plane slice corresponding to the $\sqrt{3}\boldsymbol{a}_{\mathrm{hex}} \times \sqrt{3}\boldsymbol{a}_{\mathrm{hex}}$ ordering in the TM layers as well as faults in the stacking sequences perpendicular to the TM layers along the $\mathbf{c}_{\mathbf{hex}}$ axis.[21] A sharp increase in the 2θ position of the (110) peak strongly correlates with decreases in the *a* lattice parameter illustrating strong anisotropy in the material during the charging step. The degree of 2θ separation (110) and (108) peaks has been previously associated with the layeredness and ordering in the material. At the end of the plateau region, the difference in 2θ positions of these two peaks is the greatest.

6.2.2 Strain Effects During Electrochemical Cycling

Evidence for microstrain can be extracted by examining line broadening observed in the XRD patterns. With a technique developed by Williamson and Hall,[151] X-ray line broadening can be used to determine microstrain and crystallite size in a given sample.

The microstrain extracted from Williamson-Hall type analysis can be explained by non-uniform strain originating from systematic shifts of atoms from their ideal positions resulting from defects such as point defects, site-disorder and vacancies as well as plastic deformation. Figure 6-4 shows strain values obtained at different points of the first electrochemical cycle. The points at t = 0 and t = $2.6 \mathrm{x} 10^5$ seconds correspond to the pristine material and the electrochemically cycled material obtained following 10 cycles, respectively. The plot shows that the strain in the material increases during the initial sloping region.

The combined results allow us to propose a mechanism to explain the changes in strain during the first electrochemical cycle. The increase in strain during the sloping region could be attributed due to the removal of Li from the lithium layer causing a concentration gradient in the structure. As Li is extracted from the lithium layer, strains may originate from electrostatic repulsions from adjacent oxygen layers. Our previous research showed that in this region, the Li migrated into the tetrahedral sites above and below the Li layer. [127] Preliminary research suggests that Ni^{2+} ions may migrate to adjacent Li layer causing site vacancies in the TM layer. Moreover the Li transport is accompanied by the oxidation of Ni^{2+} to Ni^{4+} which could impart stress on the structure due to the shrinking *a* lattice parameters. The lithium ions can form an energetically stable phase with tetrahedral dumbbells by the end of the slope region and at the same time the lithium layer will be partially filled by migrating Ni ions mitigating the strain created by local lithium concentration gradient. This reduces the microstrain as observed at the beginning of the plateau region. During the plateau region, the strain begins to increase. There are several mechanisms that could explain this increase in strain. First, previous research has indicated oxygen removal occurs during the plateau. [18, 29, 32] The Li ions in the TM layer are removed simultaneously with oxygen loss. A second possibility is that lithium and oxygen vacancies are created *non-uniformly* during the plateau region, which may increase microstrain in the structure. Figure 6-6A shows e*x situ* TEM taken at this plateau region. The figure depicts changes in image contrast indicating the material is full of defects and strain.

As the discharge step begins, the strain decreases first then increases to a value matching that observed from *ex situ* measurements. This validates the results found by the present *in situ* study. The reduction in strain at the beginning of the discharge cannot be clearly explained yet. Overall, during the discharge step, the strain increases. This originates from the large Li^+ ions re-entering the structure causing lattice expansion and filling lattice vacancies. During the charging step, the material has a clear strain and stress relief mechanism via lithium tetrahedral formation, oxygen loss and transition metal migration; however, during discharge, these mechanisms are no longer available. Second phase particles and concentration gradients in the particles both contribute to non-uniform microstrain.

The proposed lithium and transition metal migration mechanisms are depicted in Figure 6-5. The first electrochemical cycle is divided into 7 regions. Initially Li ions are removed from the Li layer causing a concentration gradient and electrostatic repulsion from adjacent oxygen layers accounting for the increased strain and *c* lattice parameters (Figure 6-5A). At the end of the sloping region (Figure 6-5C), Ni and Mn ions are in their fully oxidized 4+ state. Our previous finding [21] indicates that energetically stable tetrahedral Li ions form. These two factors account for the *a* and *c* lattice collapse and the strain decreases at the end of the sloping region. During region 4 (Figure 6-5D), the plateau region, *a* lattice parameter increases while *c* lattice parameter continues to decrease while the strain increases. This indicates that the strain can be correlated to the *a* lattice changes. During the plateau region, simultaneous oxygen and Li removal creates large vacancies across several layers. Transition metal cations may migrate to fill these large vacancies causing the *c* lattice parameter to remain stable; however, the increase in *a* lattice parameter may be attributed to new electrostatic repulsion forces. The first source may originate from an unbalanced number of oxygen in the cation octahedrals due to oxygen vacancies. The second source of electrostatic repulsion may originate from adjacent oxygen ions near vacant oxygen sites. As large Li ions are reinserted into the structure during the discharge step as seen in Figure 6-5F, both lattice parameters and the strain begins to increase. The material no longer has TM migration and second phase formation to mitigate the strain formation. During the final discharge step (Figure 6-5G), the material has expanded in volume compared to the original structure.

During the first electrochemical cycle, the material undergoes large changes in strain; however is able to reversibly cycle well with little capacity loss indicating that this lithium-excess family of materials can structurally withstand large lattice dimension changes (strain). The data provides evidence that the structure undergoes irreversible changes in lattice parameters and strain during the first electrochemical cycle. Rietveld refinement of the X-ray diffraction data of the electrochemically cycled electrode materials show dynamically changing lattice parameters. Anisotropy in a and c directions are observed and is the greatest during the plateau region. Following the electrochemical cycling, both lattice parameters have expanded from the pristine material showing irreversible changes. Microstrains observed in the material were extracted using Williamson-Hall analysis. The strain analysis shows that the material undergoes large changes in the strain; however is able to reversibly cycle. During the charging cycle, the charge compensation mechanisms such as oxygen removal and cation migration accommodates the strain; however during discharge, these compensation mechanisms do not exist; therefore, causing the strain to increase. The large changes in strain are linked to the lithium and cation transport mechanisms observed in these materials.Our *in situ* analysis of specific structural changes in $Li[Li_{0.2}Ni_{0.2}Mn_{0.6}]O_2$ material further improved the understanding of the dynamic changes in these complex oxides when Li is extracted and/or inserted.

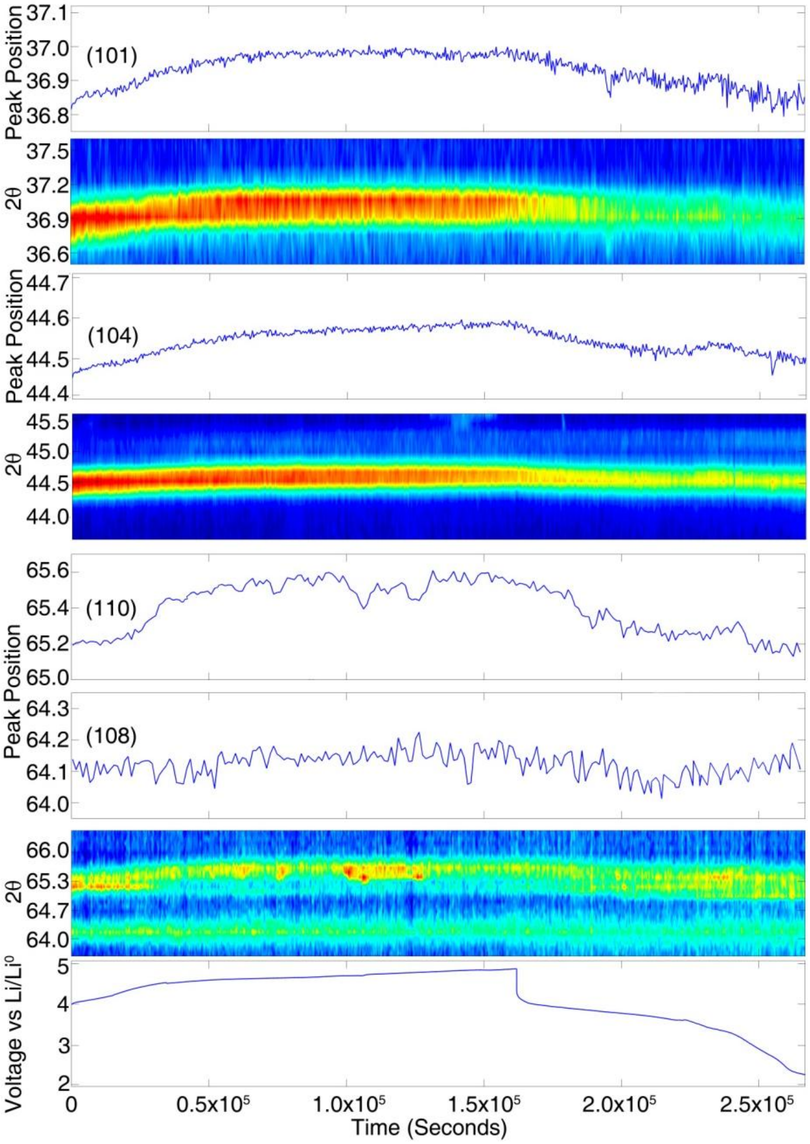

Figure 6-1. *In situ* electrochemical measurements during the first charge and discharge cycle with sectioned surface contour plots of the (101), (104), (110) and (108) X-ray diffraction reflections.

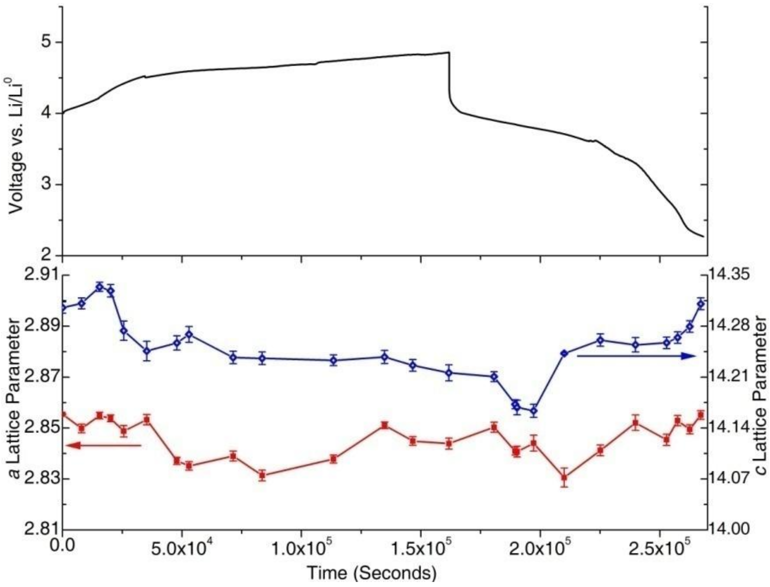

Figure 6-2. The first cycle *in situ* electrochemical profile plotted versus time. Lattice constants *a* and *c* of Li[$Li_{0.2}Ni_{0.2}Mn_{0.6}$]O_2 plotted as a function of time. The red square and blue diamond lines represent the *a* and *c* lattice parameters of the pristine material respectively. Error Bars shown correspond to σ

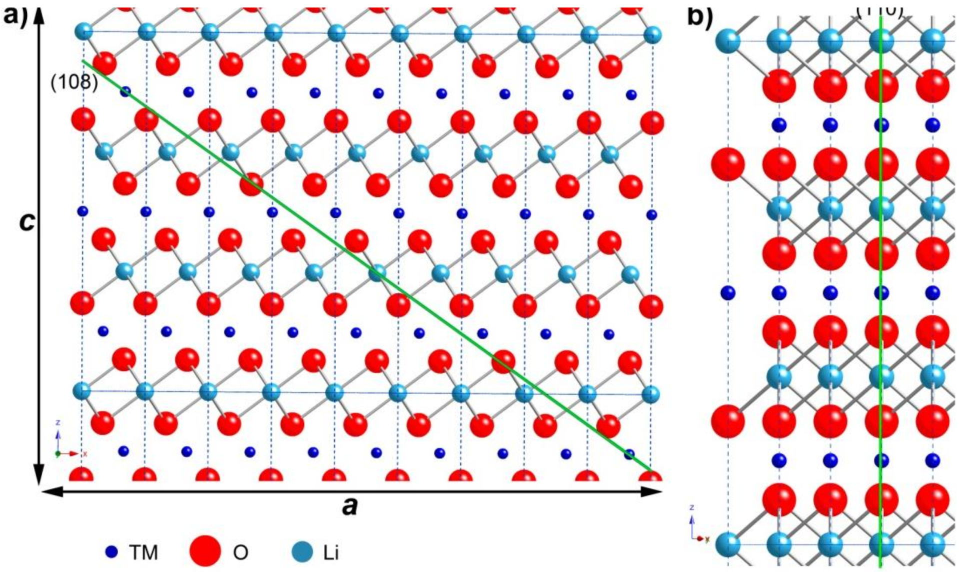

Figure 6-3. The structure of the Li[$Li_{0.2}Ni_{0.2}Mn_{0.6}$]O_2 illustrating alternating transition metal, oxygen and lithium layers of the A) (108) and B) (110) planes.

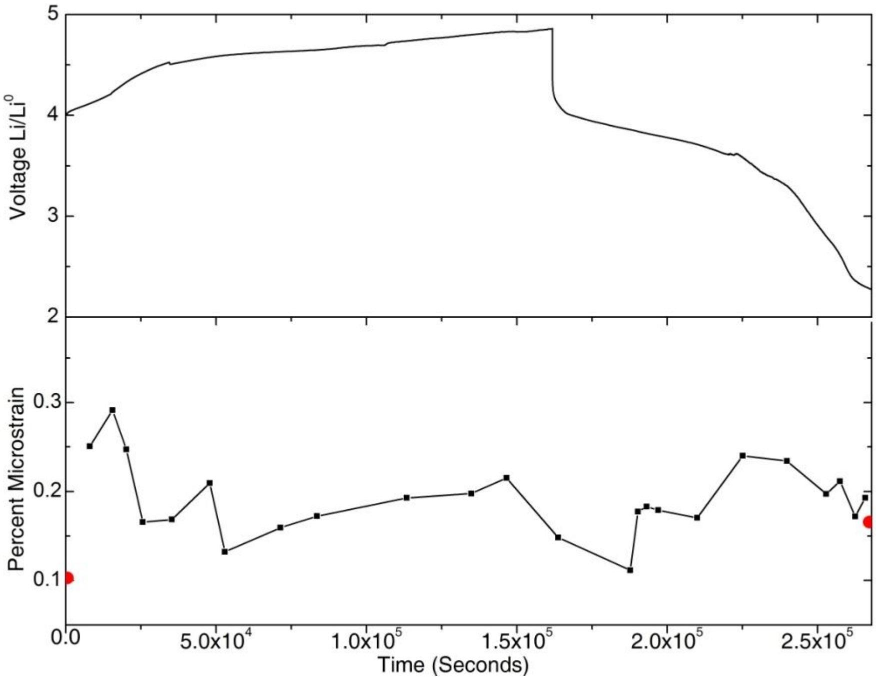

Figure 6-4. *In situ* electrochemical measurements combined with the strain calculated using Williamson-Hall equations during electrochemical cycling. Red dots correspond to strain measurements obtained from the as-synthesized (t=0) and *ex situ* measurment (t=2.68x10^5)

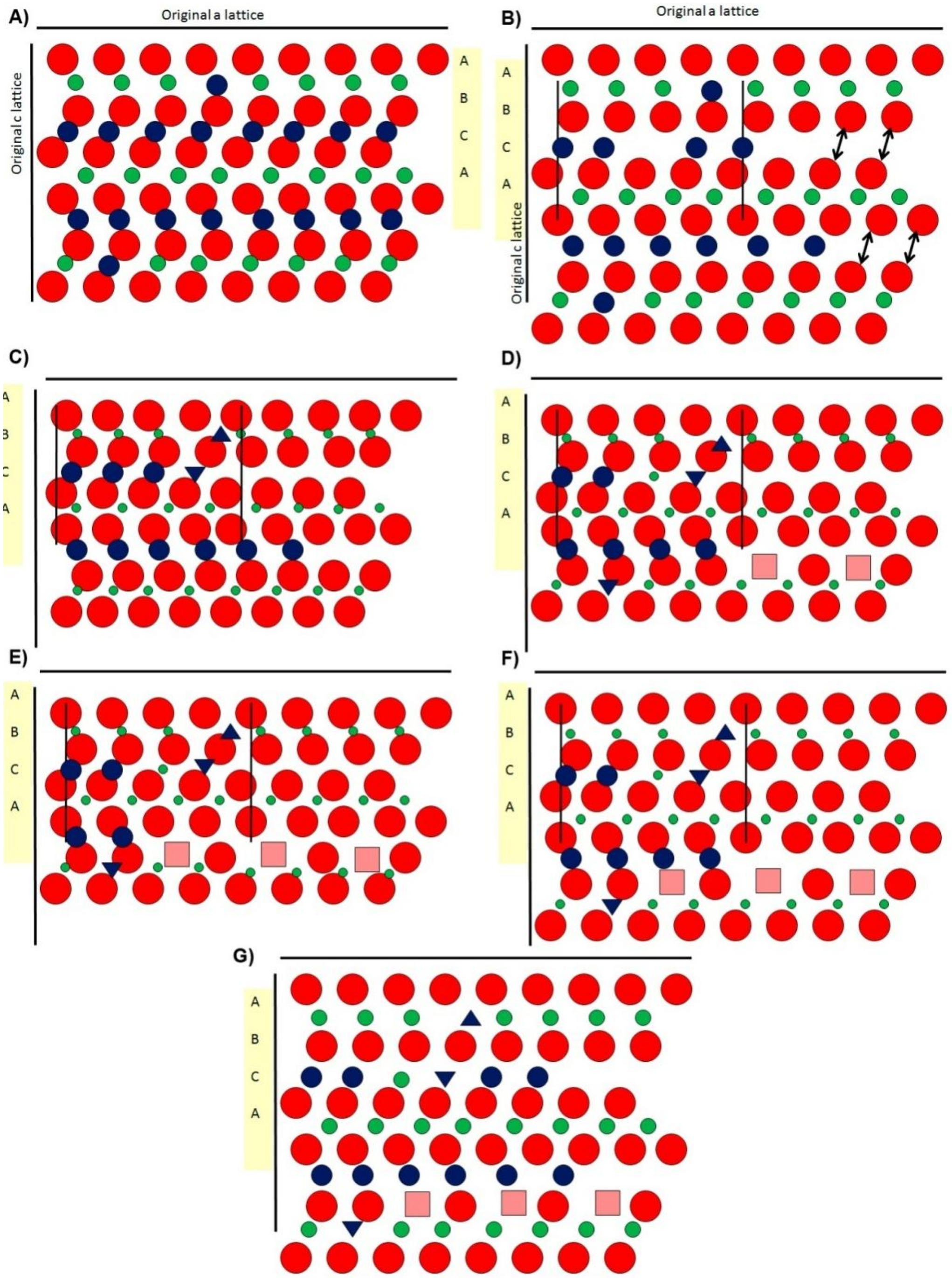

Figure 6-5. Sketch of Li and TM cation migration during 7 regions of the first electrochemical charge/discharge cycle at A) pristine, B) middle of the sloping region C) end of the sloping region, D) middle of the plateau E) end of the first charge cycle F) middle of the first discharge G) end of the first discharge. . (Red: Oxygen, Green: TM, Blue: Li, Pink: Vacancy)

CHAPTER 7
DYNAMIC STRUCTURAL CHANGES IN LITHIUM-EXCESS LAYERED OXIDES DURING THE FIRST ELECTROCHEMICAL CYCLE

This chapter is based on the manuscript “Dynamic Structural Changes In Lithium-Excess Layered Oxides During The First Electrochemical Cycle” by Christopher R. Fell, Kyler J. Carroll, Gabriel M. Veith, Miaofang Chi, Jacob L. Jones Ying Shirley Meng. *(In preparation)* a-STEM and EELS was operated by Miaofang Chi and XPS data was operated by Kyler J. Carroll.

The findings from Chapter 6 linked the changing structural parameters to the first electrochemical charge cycle using *in situ* X-ray diffraction. The lithiation mechanisms for the lithium-excess materials have been extensively examined in the prior chapters, a detailed understanding of the oxygen loss mechanism during the plateau region, contributing to the anomalous capacities, remains unanswered. In this chapter, a detailed study using synchrotron X-ray diffraction, aberration corrected scanning transmission electron microscopy, electron energy loss spectroscopy combined with electrochemical testing on $Li[Ni_xLi_{1/3-2x/3}Mn_{2/3-x/3}]O_2$ (x=1/5) compounds during the first electrochemical cycle at different states of charge were performed to identify structural changes.

7.1 Methodologies

7.1.1 Electrochemistry

Electrochemical properties were measured on an Arbin battery cycler in galvanostatic mode as described in Chapter 2.

The intermittently cycled samples for characterization were recovered by disassembling cycled batteries in an argon-filled glovebox. The cathode was washed by submerging in Acetonitrile (H_2O<1 ppm) 3 times. The cathode was allowed to dry in

Argon atmosphere overnight. The powder was scraped and mounted in a hermetically sealed capillary for synchrotron X-ray diffraction. For TEM sample preparation, the powders were suspended on a copper grid with lacey carbon. The approximate time of sample exposed to air (from a sealed environment to the microscope column) is less than 5 seconds.

7.1.2 Structural Characterization

7.1.2.1 Synchrotron x-ray diffraction

Powder X-ray diffraction patterns were taken using synchrotron X-ray diffraction at the Advanced Photon Source (APS) at Argonne National Laboratory (ANL) on beamline 11-BM ($\lambda = 0.413$ Å). All samples were hermetically sealed in 1.0 mm kapton capillaries to minimize air-exposure. The beamline uses a sagittally focused x-ray beam with a high precision diffractometer circle and perfect Si(111) crystal analyzer detection for high sensitivity and resolution. Instrumental resolution at high Q is better than $\Delta Q/Q \approx 2\times10^{-4}$, with a typical 2θ resolution of $< 0.01°$ at 30 keV. XRD data analysis was carried out by Rietveld refinement method using FullProf and GSAS/EXPGUI software.

7.1.2.2 a-STEM/EELS

Electron Microscopy work was carried out on a Cs-corrected FEI Titan 80/300-kV TEM/STEM microscope equipped with a Gatan Image Filter Quantum-865. All STEM images and EELS spectra were acquired at 300KV and with a beam size of ~0.7Å. EELS spectra shown in this work were acquired from a square area of ~0.5*0.5nm with an acquisition time of 3 seconds and a collection angle of 35 mrad. HAADF images are obtained with a convergence angle of 30 mrad and a large inner collection angle of 65 mrad. To minimize possible electron beam irradiation effects, EELS and HAADF figures here are acquired from areas without pre-beam irradiation.

7.2 Results

7.2.1 Electrochemistry

Electrochemical measurements of Li[$Li_{1/5}Ni_{1/5}Mn_{3/5}$]O_2 electrodes were performed in lithium half-cell batteries. Figure 7-1 displays the voltage (V) versus capacity (mAh/g) electrochemical curves in galvanostatic mode at C/50 for the first charge/discharge cycle. During the first electrochemical cycle, the electrochemical test is stopped at 8 different states of charge positions. Table 7-1 indicates the voltages, capacities and corresponding Li remaining in the material assuming all of the electrochemical capacity corresponds to Li removal and insertion from the material.

7.2.2 Synchrotron X-Ray Diffraction

High resolution synchrotron X-ray diffraction was utilized for the analysis of the change in crystal structures of Li[$Li_{1/5}Ni_{1/5}Mn_{3/5}$]O_2 during the first electrochemical cycle as shown in Figure 7-2. The X-ray diffraction pattern (Figure 7-2I) of the pristine material was reproduced from Ref. [127]. Rietveld refinement of the pristine material indicates that it is a typical well layered phase with 0.03 Li/Ni mixing. XRD patterns were taken at 4.40 V (A in Fig. 7-1) during the sloping region where Ni^{2+} is oxidized to Ni^{4+} (Figure 7-2II). It is clear from the diffraction pattern that the superlattice ordering remains intact as was previously shown from literature. Rietveld refinement at position A indicates that the material maintains the well layered phase and the amount of Li/Ni mixing decreases. Figure 7-3 and Table 7-2 shows that the *a* lattice parameter decreases 0.0089 Å and the *c* lattice parameter increases 0.032 Å from the pristine material. This trend is consistent with the oxidation of Ni^{2+} to Ni^{4+}, during which the ionic radius decreases from 0.69 Å to 0.48 Å. [25] The refinement also confirms the material remains a single layered phase with no obvious phase transformations at position A. At the end of the sloping region 4.45 V, position B, Rietveld refinement indicates that a single layered phase provides the best fitting seen in Figure 7-2III. Figure 7-3 and Table 7-2 shows that the amount of Li/Ni mixing continued to decrease leading to the end of the sloping region. Moreover, the *a* and *c* lattice parameters continue to decrease and increase, respectively, consistent with the Ni^{2+}/Ni^{4+} redox reaction. Our previous research indicated that at the end of the sloping region, tetrahedral Li^+ would be energetically favorable for formation. [127]

When the single phased layered refinement model assumed tetrahedral Li^+ site occupancy, the conventional Rietveld reliability factors R_{wp} and R_b results showed no improvement. More details on the formation of tetrahedral Li^+ will be discussed later. At the end of the charging cycle to 4.80 V, Figure 7-2IV (D in Fig. 7-1) shows the results of crystallographic refinements using the diffraction pattern of $Li[Li_{1/5}Ni_{1/5}Mn_{3/5}]O_2$. The refinement used two independent phases of the $R\bar{3}m$ space group where one of the $R\bar{3}m$ phases assumed tetrahedral Li^+ occupancy. The addition of a second layered phase with tetrahedral Li^+ occupancy improved the fitting of the (003), (104), (110) and (108) peaks over a single layered $R\bar{3}m$ phase or two independent $R\bar{3}m$ layered phases without tetrahedral Li^+ occupancy. The use of a second phase increased the flexibility in the refinement to account for peak broadening as well as peak shoulders forming in the diffraction pattern. Moreover, the second phase helps explain the stacking faults forming in the microstructure which will be explained later. Rietveld refinement of the material electrochemically cycled to 4.80 V (Figure 7-2IV, D in Fig. 7-1) indicates that there is strong evidence of tetrahedral Li^+ formation. The Rietveld reliability factor R_b shows improvement from 5.3 to 3.77 when 0.1 tetrahedral Li^+ ions are included in a second layered phase. The pattern also illustrates that the superlattice peaks are still evident indicating that long range cation ordering is still present in the transition metal layer even when the material is delithiated to $Li_{0.25}Ni_{0.2}Mn_{0.6}O_2$ or the removal of 0.95 structural Li^+ ions. This may indicate that the Li^+ ions are pinned in the TM layers unable to diffuse. At this point of the electrochemical cycle, the amount of Li/Ni interlayer mixing increased to 0.05 from 0.015 at the end of the sloping region seen in Table 2. The increased interlayer mixing could be facilitated by the cation migration of the Li^+ ions from the transition metal layer into the tetrahedral sites and the large amounts of vacancies created the Li^+ layer. To explore the possibility of oxygen loss in the structure, oxygen occupancies were refined without constraints. The Rietveld refinement results indicate that in the layered phase with tetrahedral Li^+ ion formation, 20% oxygen loss is observed, while the oxygen content of the second layered phase remains constant at 2.0. The R_{wp} values improve from 3.63 to 3.53 while the Rb values remain constant. The other refined parameters including lattice parameters, cation occupancies, lattice positions remain constant as shown for D in Table 7-2.

During discharge, refinement using a single layered phase no longer leads to pattern convergence. Rietveld refinement confirms that the material retains the two independent layered phase structures with tetrahedral Li^+ ion occupancy. The fitting results during the discharge cycle can be seen in Table 7-2B. During the discharge cycle, the superlattice peaks between 20° and 30° 2θ are evident until position F at 3.30 V as seen in Figure 7-2V. The X-ray diffraction pattern following the first electrochemical cycle is shown in Figure 7-2VI (A’ in Fig 7-1). The superlattice peaks do not return during the remainder of the discharge cycle as confirmed from previous research. [34, 109]

Rietveld refinement results of the tetrahedral Li^+ ion occupancy indicate that following the discharge cycle, the tetrahedral site occupancy increases from 8.7% to 10.1%. Our previous research found that following 10 electrochemical cycles the tetrahedral site occupancy increased further to 13.5%. Both layered phases show a decreasing trend in the *c* lattice parameter. The phase including tetrahedral Li^+ occupancy decreased 0.1% and the other layered phase decreased 0.3% during the discharge cycle. However, the *c* lattice parameter expands 0.4% overall from the pristine material to the end of the discharge cycle. In contrast, the *a* lattice parameter expands during the discharge cycle. The expansion of the phase including tetrahedral Li^+ occupancy is 0.7%, meanwhile the other layered phase expands 0.2%. The overall *a* lattice parameter expansion during the first electrochemical cycle is 0.2%

7.2.2.1 Strain effects during electrochemical cycling

Evidence for microstrain can be extracted by examining line broadening observed in the XRD patterns. The Williamson-Hall method [151] considers the contributions of crystallite size and microstrain in X-ray line broadening. to be additive where:

$$\beta_{total} = \beta_{particle\ \ size} + \beta_{strain} \qquad (7\text{-}1)$$

Crystallite size is given by the Scherrer equation [84] while the contributions of broadening due to microstrain are obtained by differentiating Bragg's law.

$$\beta_{total} = \frac{0.94\lambda}{t\cos\theta} + 4\tan\theta\ (\frac{\Delta d}{d} \qquad (7\text{-}2)$$

where the final Williamson-Hall equation is obtained by multiplying both sides of Equation 7-2 by cosθ to give the final form of

$$\beta_{total}\cos\theta = \frac{0.94\lambda}{t} + 4\sin\theta\ (\frac{\Delta d}{d}) \qquad (7\text{-}3)$$

The diffraction angle is given by θ, β_{total} is calculated from the integral breadth from the measured samples during the first electrochemical cycle subtracting for instrumental contributions, λ is the X-ray wavelength of the source, t is the crystallite size and the microstrain is represented by Δd/d. The strain is extracted from the slope of the plot of β cos θ versus 4sin θ. Figure 7-3 shows microstrain values obtained at different states of charge during the first electrochemical cycle. The error bars correlate to the standard error σ. Williamson-Hall type microstrain can be explained by non-uniform strain effects originating from systematic shifts of atoms from their ideal positions resulting from defects such as point defects, site-disorder, vacancies as well as plastic deformation. The plot shows that the microstrain remains constant from the pristine material through the sloping region to 4.45 V. At the end of the electrochemical charging cycle to 4.80 V, the microstrain increases 0.1%. However, the errors associated with the microstrain values with states of charge at 4.80 V, 4.00 V and 3.30 V (Positions D, E, F respectively in Fig 7-1) have increased significantly seen in Figure 7-4. TEM images taken at these states of charge show large amounts of stacking faults and the formation of dislocations within the material. Figure 2-10 shows that when the amount of dislocations increase in a material, the use of the linear Williamson-Hall analysis does not produce good fitting and the use of the modified Williamson-Hall plot is necessary. However, in this series of materials, the stacking fault systems and burgers vectors are not well explored or easily calculated. In this analysis, the conventional Williamson-Hall analysis was performed; however, future research should identify and correct the source of error found in this research. The microstrain increase correlates well with the amount of Li^+ ion vacancies in the delithiated sample as well as site-disordering from the possibility of tetrahedral Li^+ site formation seen in Table 7-2. Microstrain effects may also originate from cation migration including oxygen removal, Li/Ni site mixing and a second layered phase formation. Cation migration is confirmed from Rietveld refinement of the XRD patterns and oxygen loss is confirmed from the EELS spectra. The microstrain values continue to increase during the first half of the discharge cycle. At this point, large Li^+ ions are re-entering the structure creating stacking faults along the *c* (001) direction as evidenced with TEM. Furthermore, the Ni^{4+} ions are reducing to Ni^{2+} as supported through the EELS spectra causing a contracting lattice during discharge supporting increased microstrain and stacking fault formation in the material. The microstrain decreases as additional Li^+ are intercalated into the material at the end of the discharge cycle. Increased Li^+ ion intercalation compensates the site defects and vacancies created in the delithiated material accounting for the decreasing microstrain. Overall the microstrain created in the material is not completely reversible which contributes to the irreversible capacity loss as well as the low cycling rates required by this material during the first electrochemical cycle to activate the additional Li^+ ion removal.

7.2.3 TEM/STEM

Figure 7-5 depicts electron microscopy data at 3 different points along the first electrochemical charging cycle (4.45 V 4.60 V and 4.80 V) and 2 different points during the first electrochemical discharging cycle (3.50 V and 2.00 V). Multiple grains were selected for study and the results are consistent, therefore only representative data are shown here. Figure 7-5I shows that the pristine material has well faceted surfaces, a high degree of crystallinity and well layered properties in the bulk extending to the surface. Figure 7-5II shows the TEM image following charging to the end of the sloping region at 4.45 V, illustrating the formation of nano-cracking extending through the first 20 nm of the material. The figure shows that the faceted and clear cut surfaces in the pristine material begin to lose faceting indicating possible material loss. Attempts to capture HAADF-STEM imaging were unsuccessful from the beginning of the voltage plateau region throughout the remainder of the first electrochemical charge/discharge cycle because of the evolution of strains and defects preventing visualization of the atomic columns. Figure 7-5III shows low magnification TEM images taken of the sample stopped at the middle of the plateau region (4.60 V) corresponding to a charging capacity of 200 mAh/g. The figure shows a significant increase in the formation of nano-cracks that span into the bulk of the material. The zoomed surface in Figure 7-5III (right) shows large amounts of strain, nano-cracks and dislocations extending from the bulk of the material to the surface.

Upon discharge to 3.30 V, approximately 0.5 Li^+ ions are re-intercalated into the structure. The TEM image in Figure 7-5IV suggests that the amount of nano-cracking and defect densities continue to increase in the material. High resolution TEM images show increased stacking faults and even the possibility of the inclusion of lamellar twinning [152] as highlighted in the image. Electron diffraction of the particle reveals that there are no longer distinct spots consistent with a well layered structure, but streaking indicating changes in long range ordering and layeredness of the material which can be seen in Figure 7-6. This streaking has been found consistent with changes in periodicity suggesting the formation of a spinel like phase. Following discharge to 2.00 V, Figure 7-5V shows that the nano-cracks as well as the defects seen at previous points during the electrochemical cycle have disappeared. The large amounts of stacking faults seen in

Figure 7-5IV as well as the nano-cracking seen in Figure 7-5III have disappeared and the material domains appear more homogeneous. Furthermore, following discharge is the first point where the strain does not overwhelm the image and Z-contrast images, using an HAADF detector can be collected. Figure 7-7 compares the Z-contrast images of pristine $Li[Ni_{1/5}Li_{1/5}Mn_{3/5}]O_2$ and following the first full electrochemical cycle. The image shows that the bulk of the material still maintains the well layered structure; however, the contrast within the first 2 nm of the surface changes. Along the *(0 0 -1)* direction, the dark columns become much brighter on the surface. The contrast matches that of the neighboring TM columns. This suggests that, following the first electrochemical cycle, a defect spinel like structure has formed, consistent with previous findings.[127]

7.2.4 EELS

Figure 7-8I compares the EELS spectra of the oxygen K-edge, manganese L_3 and L_2 edges and nickel L_3 and L_2 edges from the bulk of the structure taken at different states of charge during the first electrochemical cycle. The structural evolution can be interpreted using changes in the fine structures and the energy positions of the O-K, Mn-L and Ni-L edges which correlate to the electronic structure of the sample.

Examining the Mn L-edge energy loss positions during the sloping region of the first charging cycle shows that the peak positions remain constant. Furthermore, the L_3/L_2 intensity ratio remains constant. When the material is electrochemically charged into the voltage plateau region, there is a noticeable shift in the L_3/L_2 intensity ratio, which indicates oxidation state variations in transition metals.[63, 67] At this position both the Mn and Ni ions are in their fully oxidized 4+ state; therefore, this shift in Mn fine-structure may indicate that the bulk Mn^{4+} ions may be involved in supplying charge compensation for the anomalous capacity during the plateau region.

Figure 7-8II shows that the oxygen K-edge energy loss position shifts to higher energies during the first electrochemical charging cycle. The shifting energy loss during the sloping region correlates with the Ni^{2+}/Ni^{4+} redox reaction. However, the Oxygen K-edge shifts to higher energy losses into the plateau region. This indicates that the oxygen may continue to participate in the electrochemical reactions or there is a shift in the local environment due to oxygen loss. From the end of the sloping region at 4.45 V to the end of the middle of the plateau region at 4.60 V, the O-K edges show fine-structure modifications on the spectrum. The first peak, at energy loss of ~532 eV decreases in intensity indicating a transition of 1s core states to the unoccupied O-*2p* states hybridized with TM-*3d* states. As this peak intensity is decreasing, it indicates that there is modification of the unoccupied states of TM-*3d* and bonding lengths of adjacent transition metal ions. These results show that in the bulk structure beginning at the voltage plateau region, Ni^{4+}, Mn^{4+} and Oxygen are simultaneously changing local environments and may all participate in charge compensation during the voltage plateau region.

During the discharge cycle, the Ni L-edge fine structure and energy positions revert to the original energy losses of the pristine material indicating that the Ni redox reaction is a reversible process such that the Ni^{4+} is reduced to Ni^{2+} following the first electrochemical cycle. The Mn L-edge energy loss positions during the discharging cycle shows that the peak positions remain constant. However, the intensity ratio of the L_3 peak to L_2 peak decreases towards the ratio seen in that of the pristine material;

however, remain slightly elevated compared to the pristine material. This indicates that the Mn ions change oxidation state indicating that the ions are involved in the electrochemical cycle. The process is not completely reversible and may account for capacity fading in subsequent cycles. During the discharge cycle, the oxygen K-edge energy loss peak positions does not shift back to the original energy loss suggesting permanent changes in the oxygen local environment.

7.3 Discussion

The combined results obtained from synchrotron XRD, TEM and EELS allow us to identify the origin and explain the formation of lithium delithiation/reintercalation mechanisms within the first electrochemical cycle. We have shown that the structural modifications occurring during the first electrochemical cycle play a significant role in the electrochemical properties of the lithium-excess series of materials. There are two distinct regions during the first charging cycle which can be separated into the initial stage before the plateau region before 4.45 V and the voltage plateau region between 4.50 V and 4.80 V. The mechanisms forming during discharge cycle will be explained as an entity.

7.3.1 Initial Stage Of Lithium Deintercalation (Pre-Plateau Up To 4.45 V)

The results obtained from XRD refinement and EELS suggest that solid solution behavior exists between open circuit voltage and 4.40 V. The structural modifications seen in this region is reversible. The Li^+ ion is continuously extracted from the material with the oxidation of Ni^{2+} to Ni^{4+} accompanied with monotonically shifting lattice parameters consistent with previous experimental work.[22, 26] Changes to the material begin occurring at the end of the sloping region at 4.45 V. TEM images indicate that defects and nano-cracks are forming in the material; however, the Williamson-Hall calculations indicate that the microstrain is not increasing. The constant microstrain may be explained by the formation tetrahedral Li^+ ion sites, which were found to be very energetically favorable and would require large voltages for removal, thus preventing an increase in microstrain. A decrease in Li/Ni interlayer mixing during the sloping region can be explained by the ability of Ni^{2+} ions to migrate between adjacent octahedral sites through empty tetrahedral sites.

7.3.2 Plateau Region (4.45 V To 4.80 V)

The results indicate that irreversible structural changes begin forming during the plateau region. XRD, EELS and TEM results show significant changes to the structure and local atomic environments. We propose that these changes originate from oxygen ions providing the anomalous charge compensation through direct oxidation or oxygen loss creating oxygen vacancies. The oxygen vacancies and changes in the oxygen octahedrals create stacking faults which in turn provides a mechanism for the formation of a second layered phase. The formation of a second layered phase combined with the increased vacancies, interlayer (Li/Ni) and intralayer (Li^+ tetrahedral) cation migration cause the calculated microstrain to increase from 0.15% before the plateau region to 0.28% following the first electrochemical cycle. These mechanisms are explained in detail below.

The TEM images taken during the charging cycle in the middle of the plateau region at 4.60 V, shows large increases in the concentration of defects as well as nano-cracking throughout the entire material. The EELS spectra taken from the bulk at this state indicate that the oxygen pre-peak intensity significantly decreases and the energy loss of the peak position increases. Rietveld refinement of the XRD pattern taken at position D, charged to 4.80 V, shows evidence of 20% oxygen loss from the structure.

These observations suggest possible oxygen loss or oxygen oxidation that could contribute to the anomalous capacity seen in this region. Previous evidence suggests the possibility of direct oxygen oxidation from O^{2-} to O_2 in these lithium-excess compounds. [109, 153] Other research results support our observation suggesting possible oxygen loss concomitant with lithium removal; however, were unable to use Rietveld refinement to quantify the oxygen loss. [18, 32] The participation of oxygen in the charging process or oxygen removal at this position is believed to help facilitate the structural changes during the remainder of the first electrochemical cycle. It has been previously reported that ordered and disordered vacancies as well as the creation of stacking faults are created by transition metal or lithium layer gliding to reduce the structural free energy. Layer gliding of the TM-O and Li-O layers can create peak broadening observed in X-ray diffraction patterns. [154, 155] Following charging through the voltage plateau region to 4.80 V, the microstrain in the material has increased to a near maximum value of 0.28%. The microstrain nearly doubles from the end of the sloping region to the end of the first charge cycle consistent with the increase in the concentration of vacancies and defects or stacking faults. The TEM images taken following the first charge cycle to 4.80 V qualitatively support the large defect concentration and creation of stacking faults. We proposed that oxygen vacancies may assist cation migration. During the plateau, the structure undergoes an increase of Li^+ and Ni ion interlayer cation migration. Preliminary calculations suggest that Ni^{2+} ions may migrate from one octahedral site to another adjacent octahedral site through empty tetrahedral sites when oxygen vacancies appear in nearby atomic positions. This supports the findings that up to 4.45 V, the amount of Li/Ni interlayer mixing remains very low; however, following charging through the plateau region to 4.80 V, the amount of Li/Ni interlayer mixing increases to 0.05 and 0.07 for each phase. When compared to the pristine material, this is nearly a twofold increase. Similarly, Rietveld refinement of the XRD patterns indicates that the tetrahedral Li^+ ion formation is statistically favored. Our previous results indicated that Li^+ ion migrates in a similar mechanism to the TM ions through the tetrahedral sites; however, are trapped in these sites because of the favorable energy configuration.[126, 127] The oxygen vacancies create unstable TM or Li^+ ion octahedra which may induce layer gliding that is believed to induce a second layered phase formation at the end of the first charging cycle.

7.3.3 Discharge Region (4.80 V To 2.00 V)

The structural modifications observed during the charging region created a mechanism for the material to continue to undergo changes during the first discharge. It is proposed that the oxygen vacancies created during the plateau region induce stacking faults causing layer gliding and a second layered phase. The formation of the second layered phase at the end of the first charge cycle is still seen throughout the discharge cycle. The changes that occur during the charging cycle permanently affect the material. In fact, it has been shown that the second layered phase that we propose here remains in the material even following 10 electrochemical cycles.[109, 127] The defects formed in the material during electrochemical charging evidenced through elevated microstrain values continue to propagate during the discharge cycle.

While discharging the material to 3.30 V, the Li/Ni interlayer mixing remains near the maximum values observed at the end of charge cycle. Li^+ ion tetrahedral site occupancy remains constant during the discharge cycle showing the stability of the tetrahedral sites once formed within the material. These factors indicate that defects and site disordering remain in the material. The superlattice peaks disappear following discharge to 3.30 V (F in Fig. 1) on the discharge and do not reappear in subsequent states of discharge. It is proposed at this state of discharge, the long range ordering in the transition metal layers is disrupted by the lithiation of the structure which may create additional site defects. Microstrain values reach maximum values of 0.32% upon discharging to 3.30 V. Moreover, the amount of stacking defaults and defects seen in the TEM images following discharge to 3.30 V supports the microstrain increases in the material calculated from the Williamson-Hall analysis. The TEM image suggests that there is the formation of lamellar twinning. The physical origin of this mechanical twinning has been ascribed by most authors to a reduction of the mechanical stress fields. [156] This is an indication that during the first half of the discharge cycle, the material does not overcome the defect mechanisms initiated. The microstrain and stacking faults are not compensated by relief mechanisms as seen during the charging region. However, in the last half of the discharge from 3.30 V to 2.00 V, the Li^+ ions continue to re-lithiate the structure. The reduction in the microstrain during this region is not completely yet understood. One possibility for the decrease is that the defects and site vacancies in the delithiated Li^+ layer during the charging cycle are now re-occupied which could lead to microstrain reduction. Moreover, the TEM results taken following the first electrochemical cycle indicate that the amount of defects and stacking faults has decreased. Furthermore following the first electrochemical cycle, the STEM image (Figure 7-5) clearly shows the well layered structure in the bulk; however, the surface structure of the cycled grain is obviously changed. Along the (*0 0 -1)* direction, the dark columns (Li atomic columns) become increasingly brighter at the surface. The contrast is nearly identical to their neighboring transition metal columns. This indicates an increased concentration of transition metal ions occupying the Li layer with the first 1-2 nm of the surface. This result is consistent with the results following 10 electrochemical cycles that suggested the formation of a defect spinel-like phase formed at the surface. [127]

7.3.4 Summary

Based on the experimental results presented, we have shown that the mechanisms providing charge compensation during the first electrochemical cycle of the lithium-excess layered oxide materials are complex. We have presented direct evidence to describe the formation and propagation of previously identified lithium intercalation mechanisms at different states of charge. The first electrochemical cycle mechanism may be summarized as follows. Within the sloping region to 4.45 V, the Li/Ni interlayer mixing decreases while Rietveld refinement of XRD results indicate the formation of tetrahedral Li^+ sites. These two mechanisms counteract an increase of microstrain expected from delithiation associated with the oxidation of Ni^{2+} to Ni^{4+} and the accompanying lattice expansion.

During the plateau region between 4.50 V and 4.80 V, a number of structural, electrical and mechanical modifications are simultaneously occurring that enable the material to exhibit the anomalous capacities, yet reversibly cycle upon subsequent cycles with little capacity fading. We have shown that these mechanisms may originate from oxygen participation in the anomalous charge compensation via direct oxidation or oxygen loss. The oxygen activation creates a mechanism for the formation of a second layered phase with 10% tetrahedral Li^+ occupancy. We showed that the formation of a second layered phase is combined with increases in interlayer (Li/Ni) and intralayer (Li^+

tetrahedral) cation migration. The resulting cation movement and structural changes are supported by the calculated microstrain increasing nearly twofold following the first electrochemical cycle. Mechanisms to accommodate the microstrain are introduced during the first charging cycle in the form of nano-cracking and lamellar twinning.

As the material begins to discharge, we showed that the oxygen vacancy mechanism created during the plateau region continues to induce structural changes. The second layered phase formed at the end of the first charge cycle is still seen throughout the discharge cycle. Defects including increased Li/Ni interlayer mixing as well as tetrahedral Li^+ ions remain showing the stability of these defects. Upon further lithiation to 3.30 V, the superlattice peaks disappear signifying the loss of long range ordering in the transition metal layer. The concentration of defects and stacking faults are now maximized as evidenced through a maximum in the microstrain calculations. These results show that during the first half of the discharge cycle, the material does not recover and the microstrain and stacking faults are not compensated by relief mechanisms as seen during the charging region. As the material finishes discharge to 2.00 V, the defects and site vacancies in the vacant Li^+ layer during the charging cycle are now re-occupied thereby reducing the microstrain; however, permanent structural rearrangement has occurred. This includes the formation of a second layered phase that includes 10% tetrahedral Li^+ ions, increased Li/Ni interlayer mixing in both layered phases, expanded *a* and *c* lattice parameters, and residual microstrains. Furthermore, we identify the formation of a 1-2nm thick defect-like spinel phase following the first electrochemical cycle.

Our results presented here suggest that a combination of these mechanisms forming during the first charge, particularly in the voltage plateau region, impede lithium diffusion causing the low intrinsic rate capabilities and large irreversible capacity losses of this material. Identification of these mechanisms forming during the first electrochemical cycle raises questions about how surface coatings improve irreversible capacity fading and whether they remove or delay these mechanisms from forming during the first electrochemical cycle.

Table 7-1. State of charge, voltages, capacities and corresponding Li^+ remaining in the material assuming all of the electrochemical capacity corresponds to Li^+ removal and insertion from the material.

Sample Position	Cutoff Voltage	Capacity	Total Li remaining in $Li_{1.2}Ni_{0.2}Mn_{0.6}O_2$
A	Charge: 4.40 V	110 mAh/g	0.850
B	Charge: 4.45 V	125 mAh/g	0.800
C	Charge: 4.60 V	200 mAh/g	0.565
D	Charge: 4.80 V	300 mAh/g	0.248
E	Discharge: 4.00 V	50 mAh/g	0.407
F	Discharge: 3.30 V	150 mAh/g	0.725
G	Discharge: 3.00 V	200 mAh/g	0.813
A’	Discharge: 2.00 V	250 mAh/g	1.041

Table 7-2. Rietveld refinement results for Li[Li1/5Ni1/5Mn3/5]O2 at different states of charge during the first electrochemical cycling using one or two independent $R\bar{3}m$ phases. n_Li is amount of Li in tetrahedral site *a* and *c* lattice parameters given in Angstroms (Å)

Charging		
Pristine	a = 2.8608±0.0001 c = 14.2584±0.0001 c/a = 4.989 z(O) = 0.2576±0.0001 n_Ni (in Li layer) = 0.033±0.001 R_{wp} = 10.7% R_B = 6.4%	
A	a = 2.8519 ±0.0001 c = 14.2902±0.0001 c/a = 5.011 z(O) = 0.2594±0.0001 n_Ni (in Li layer) = 0.018±0.001 R_{wp} = 9.67%; R_B = 4.20%	
B	a = 2.8516±0.0001 c = 14.2995±0.0002 c/a = 5.014 z(O) = 0.2597±0.0001 n_Ni (in Li layer) = 0.015±0.001 n_Li = 0.108±0.001 R_{wp} = 10.7%; R_B = 4.95%	
D	**Phase 1:** a = 2.8595 ±0.0002 c = 14.3620±0.0003 c/a = 5.023 z(O) = 0.2598±0.0003 n_Ni (in Li layer) = 0.050±0.002 Phase Fraction: 57% R_{wp} = 8.65%; R_B = 4.19%	**Phase 2:** a = 2.8478±0.0001 c = 14.3203±0.0002 c/a = 5.028 z(O) = 0.2602±0.0001 n_Ni (in Li layer) = 0.071±0.001 n_Li = 0.099±0.001
Discharging		
E	**Phase 1:** a = 2.8600 c = 14.3844 c/a = 5.029 z(O) = 0.2608±0.0001 n_Ni (in Li layer) = 0.062±0.001 Phase Fraction: 51.7% R_{wp} = 7.50%; R_B = 3.58%	**Phase 2:** a = 2.8530 c = 14.3144 c/a = 5.017 z(O) = 0.2595±0.0001 n_Ni (in Li layer) = 0.059±0.001 n_Li (in tetrahedral site) = 0.087±0.001

Table 7-2. Continued

Discharging		
F	**Phase 1:** a = 2.8687±0.0001 c = 14.3626±0.0003 c/a = 5.007 z(O) = 0.2598±0.0001 n_Ni (in Li layer) = 0.059±0.002 Phase Fraction: 51.3%	**Phase 2:** a = 2.8655±0.0001 c = 14.3364±0.0002 c/a = 5.003 z(O) = 0.2589±0.0001 n_Ni (in Li layer) = 0.070±0.002 n_Li (in tetrahedral site) = 0.87±0.002
	R_{wp} = 7.34%; R_B = 4.04%	
G	**Phase 1:** a = 2.8667±0.0001 c = 14.3405±0.0002 c/a = 5.002 z(O) = 0.2603±0.001 n_Ni (in Li layer) = 0.042±0.001 Phase Fraction: 47.2%	**Phase 2:** a = 2.8653±0.0001 c = 14.2978±0.0002 c/a = 4.990 z(O) = 0.2583±0.001 n_Ni (in Li layer) = 0.046 n_Li (in tetrahedral site) = 0.089±0.001
	R_{wp} = 6.04%; R_B = 3.43%	
A’	**Phase 1:** a = 2.8676 ±0.0001 c = 14.3216±0.0002 c/a = 4.994 z(O) = 0.2584±0.001 n_Ni (in Li layer) = 0.38 ±0.002 Phase Fraction: 47.6%	**Phase 2:** a = 2.8688±0.0001 c = 14.3066±0.0002 c/a = 4.987 z(O) = 0.2581±0.001 n_Ni (in Li layer) = 0.061±0.002 n_Li (in tetrahedral site) = 0.101±0.002
	R_{wp} = 7.27; R_B = 3.64%	

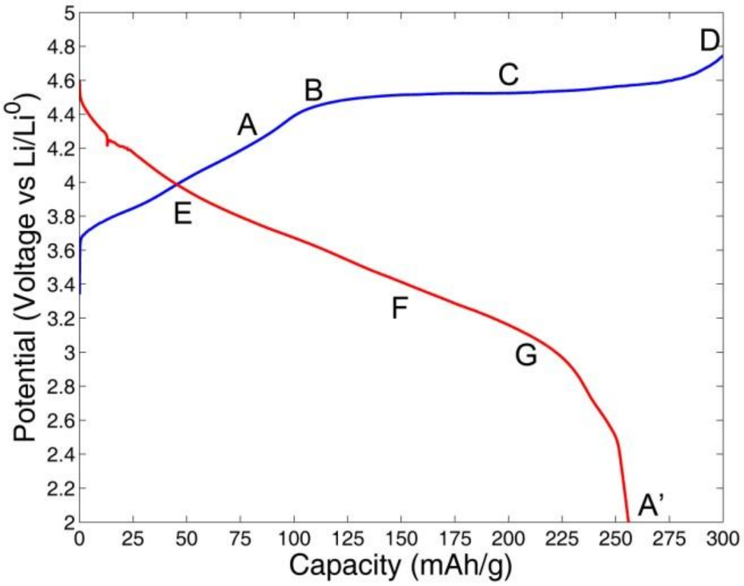

Figure 7-1. First charge/discharge curve for the layered lithium-excess cathode $Li[Li_{1/5}Ni_{1/5}Mn_{3/5}]O_2$ and the associated state of charge points studied.

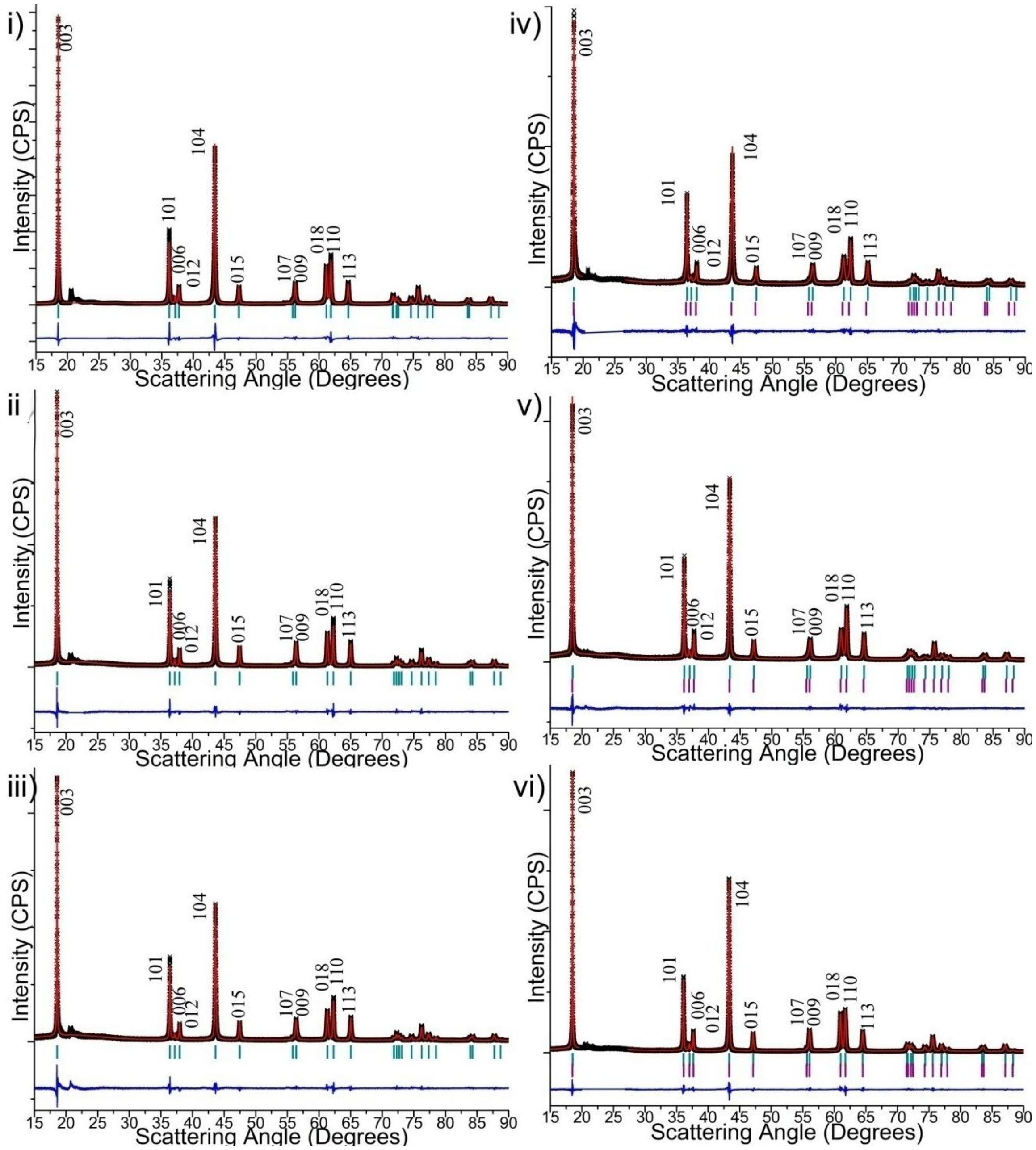

Figure 7-2. Profile fits for Reitveld refinement of synchrotron X-ray diffraction (XRD) patterns showing collected from I) the pristine Li[$Li_{1/5}Ni_{1/5}Mn_{3/5}$]O_2, II) charged to 4.40 V, III) charged to 4.45 V, IV) fully charged to 3.30 V, V) discharged to 3.30 V and VI) fully discharged to 2.00 V during the first electrochemical charge/discharge cycle. (x) indicates observed data; solid line indicates calculated profile and residual error.

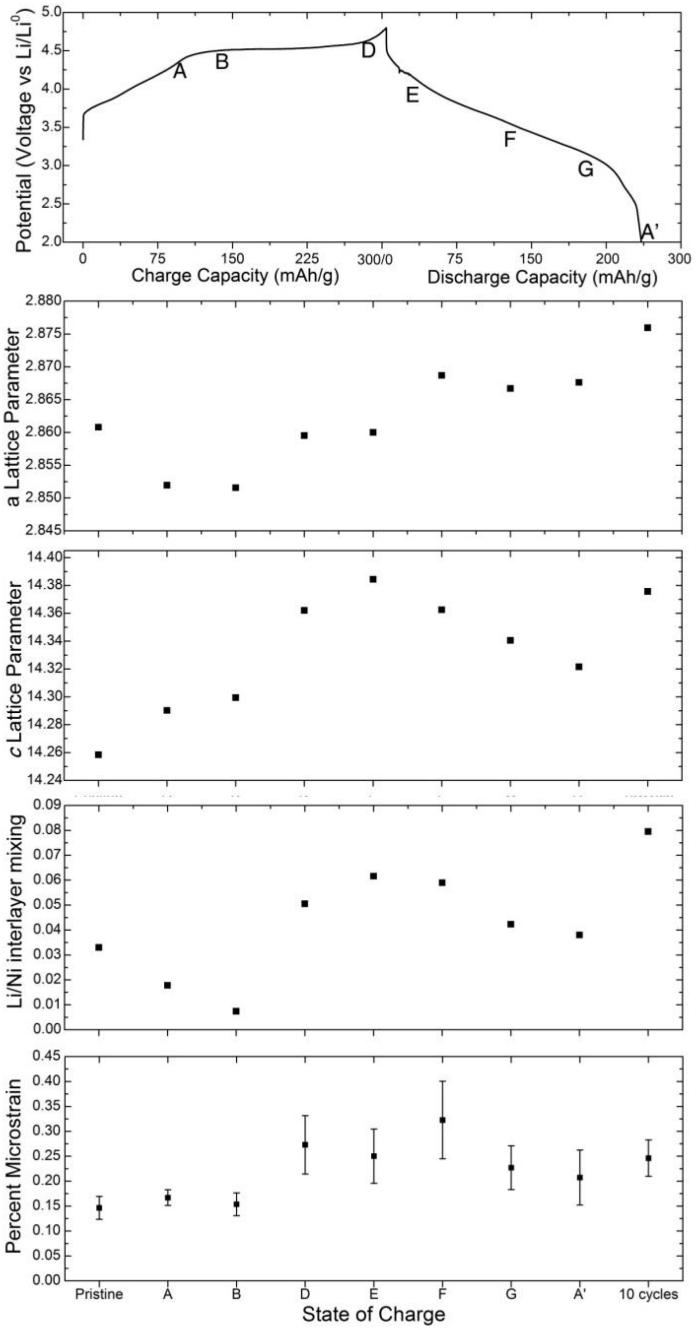

Figure 7-3. The first electrochemical voltage profile showing the points studied. Lattice constants *a* and *c*, Li/Ni interlayer mixing and percent microstrain of $Li[Li_{0.2}Ni_{0.2}Mn_{0.6}]O_2$ plotted corresponding to the state of charge in the first electrochemical voltage profile (Fig. 7-1). Error Bars shown correspond to *σ.*

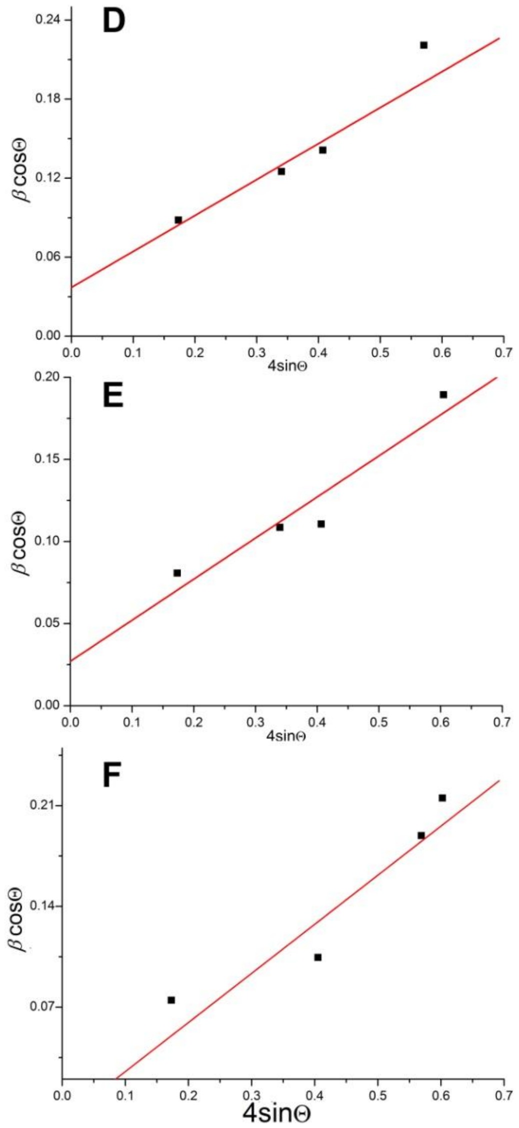

Figure 7-4 Williamson-Hall plot at states of charge 4.80 V, 4.00 V and 3.30 V corresponding to positions D, E, F in Figure 7-1 respectively

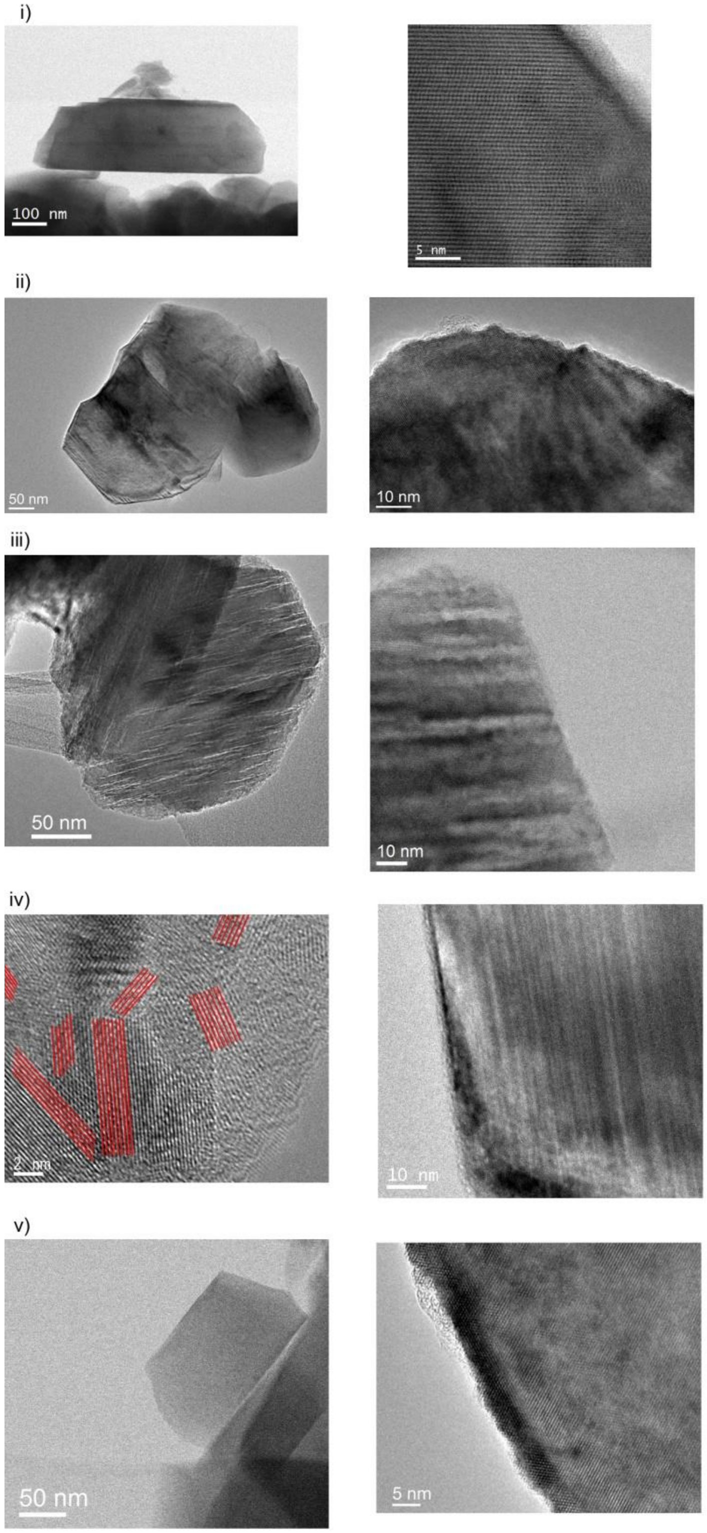

Figure 7-5. High resolution TEM images collected from $Li[Li_{1/5}Ni_{1/5}Mn_{3/5}]O_2$ I) Pristine II) charged to 4.45 V, III) charged to 4.60 V, IV) discharged to 3.30 V and V) fully discharged to 2.00 V during the first electrochemical charge/discharge cycle.

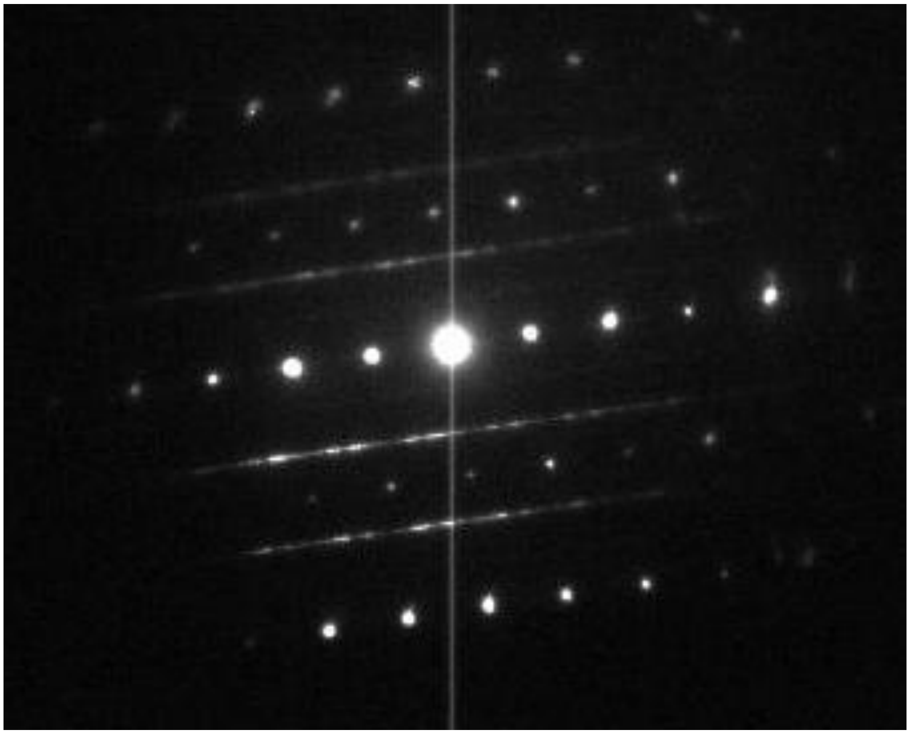

Figure 7-6. $[1\ 0\ 0]_{hex}$ electron diffraction patterns of $Li[Ni_{1/5}Li_{1/5}Mn_{3/5}]O_2$ discharged to 3.30 V (F in Fig 7-1).

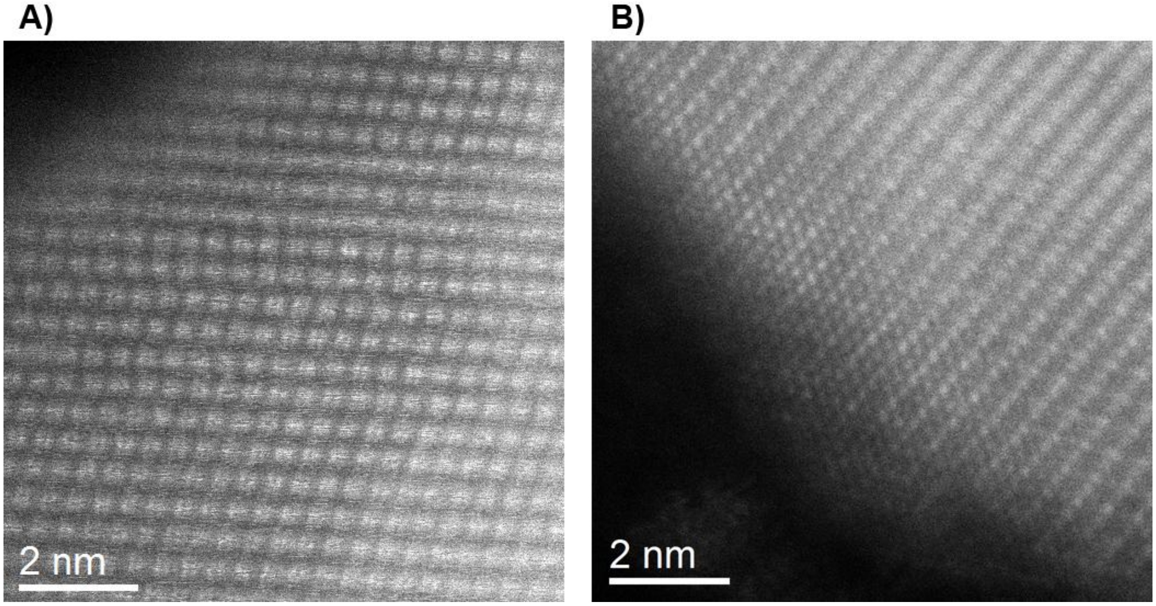

Figure 7-7. High resolution S/TEM HAADF image of the bulk and surface regions of A) pristine $Li[Ni_{1/5}Li_{1/5}Mn_{3/5}]O_2$ taken along the [1 0 0] zone axis and B) $Li[Ni_{1/5}Li_{1/5}Mn_{3/5}]O_2$ taken along the [-1 -1 0] zone axis following the first electrochemical cycle 2.00-4.80 V.

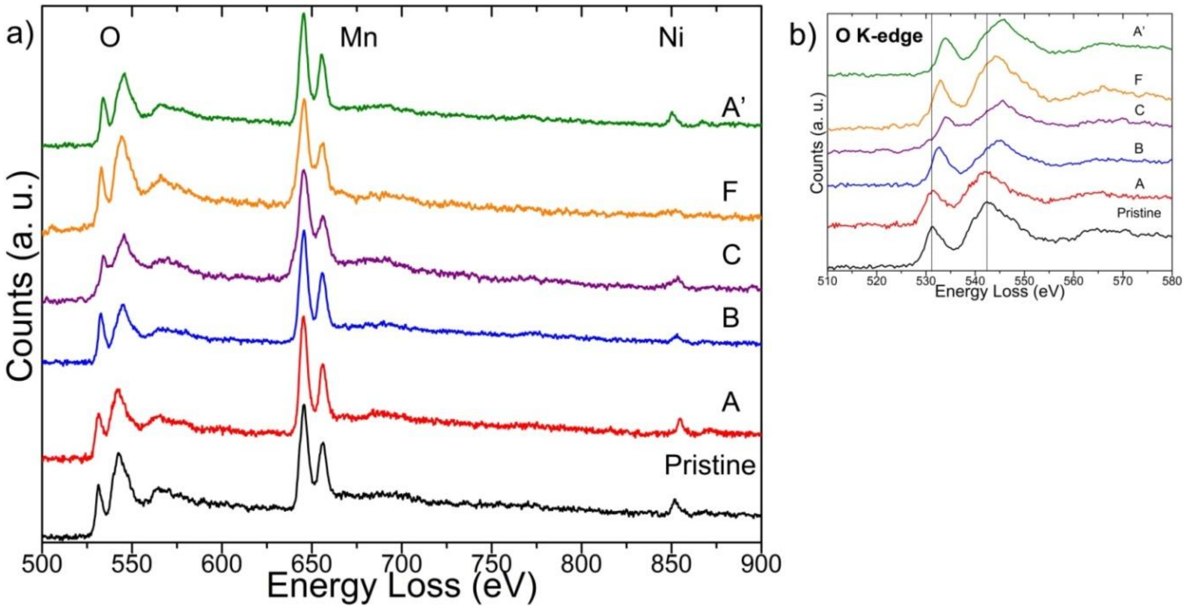

Figure 7-8. Representative EELS spectra of the bulk of the Li[$Ni_{1/5}Li_{1/5}Mn_{3/5}$]O_2 during the first electrochemical showing the A) O K-edge, and A) and B) Mn L-edge.

CHAPTER 8
SUMMARY AND FUTURE WORK

8.1 Summary

In this research, a combination of advanced characterization techniques was used to perform a thorough study on lithium-excess transition metal oxide $Li[Ni_xLi_{1/3-2x/3}Mn_{2/3-x/3}]O_2$. Chapter 3 explored and developed a relationship of the surface morphologies, bulk structure and lithium intercalation mechanisms to the electrochemical properties. Initial research explored the effects of synthesis techniques on the electrochemical properties of the material. The surface characteristics as well as particle shape and distribution dramatically affect the electrochemical properties. It was found that changing the precursor chemistry from hydroxides to carbonates increases the power and energy densities over 50% at high rates. The work also connected how the interface of particles could be altered by changing the amount of precursor thus hindering electrochemical performance including cycling stability, rate capability and the lithium diffusion coefficient. Exposing the layered lithium-excess materials, $Li[Ni_xLi_{1/3-2x/3}Mn_{2/3-x/3}]O_2$ where x=0.25, to high pressure and high temperature treatments led to drastic structural modifications, including the formation of a second layered phase with increased Li/Ni mixing and a contracted *c/a* lattice parameter ratio which was identified in Chapter 4. The post-treated $Li[Li_{1/6}Ni_{1/4}Mn_{7/12}]O_2$ samples display a good electrochemical response, with clear differences compared to the pristine material in the 4.5 voltage region. Pristine and post-treated $Li[Li_{1/6}Ni_{1/4}Mn_{7/12}]O_2$ deliver capacities upon cycling near 200 mAh/g, even though additional structural modifications are observed in the post-treated material following electrochemical cycling. The results presented reinforce the flexibility of the structure of $Li[Li_{1/6}Ni_{1/4}Mn_{7/12}]O_2$; a material able to undergo large structural variations without significant negative impacts in the electrochemical performance. It is expected that the formation of a second layered phase and increased cation mixing induced by HPHT treatment before cycling would hinder the electrochemical characteristics of the lithium-excess material. However, the material structurally rearranges during electrochemical cycling to improve the layered characteristics. These results indicate that the structural rearrangements seen during the first electrochemical cycle are critical for the electrochemical activation of the material.

Once the complexity of the interface in the $Li[Ni_xLi_{1/3-2x/3}Mn_{2/3-x/3}]O_2$ material system was understood, Chapter 5 identified the structural interface changes following electrochemical cycling. The characterization techniques linked the analysis of the electrolyte, the surface and the bulk of the cathode to gain a complete understanding of the delithiation mechanism. The surface analysis required state of the art techniques using an aberration corrected TEM. The findings led to the discovery of a new surface phase that is only 1 to 5 nm thick. Rietveld refinement of the synchrotron XRD confirmed the formation a second phase, which supports our previous research as well as led to the first detailed characterization of such a phase. This research provided a detailed cation rearrangement process and consequent phase transformation that can contribute to the variation of electrochemical properties following the charging/discharging cycle. More importantly such knowledge is pivotal to the optimization of these high voltage cathode materials.

The previous research investigated the structural changes following electrochemical cycling; however, identification of when the structural changes occurred during the electrochemical cycle is lost. *In situ* techniques were used to identify when the changes occurred. I*n situ* collection of X-ray diffraction patterns collected during the first electrochemical cycle provided evidence in Chapter 6 that the structure undergoes irreversible changes in lattice parameters and strain during the first electrochemical cycle. Rietveld refinement of the X-ray diffraction data of the electrochemically cycled electrode materials showed dynamically changing lattice parameters. The electrochemical process is anisotropic in the *a* and *c* directions and is most evident during the plateau region. Following the electrochemical cycling, both lattice parameters have expanded from the pristine material showing irreversible changes. Microstrains observed in the material were extracted using Williamson-Hall analysis in Chapter 7. The strain analysis shows that the material undergoes large increases in the strain during the plateau region; however was able to reversibly cycle. During the charging cycle, the charge compensation mechanisms such as oxygen removal and cation migration accommodates the strain; however during discharge, these compensation mechanisms do not exist; therefore, causing the strain to remain elevated. The large changes in strain were linked to the lithium and cation transport mechanisms observed in these materials.

The analysis of structural changes before, during and following electrochemical property testing has led to an increased the understanding of the lithium transport mechanisms in the lithium-excess series of materials. The findings from this research not only helps to understand and eventually improve the lithium-excess series of materials, but also can be expanded to other material systems to understand complex intricacies such as surface coatings, Li diffusion and oxygen loss mechanism, as well as phase transformation induced by ion migration.

8.2 Future Work

8.2.1 Surface Coatings

This work shows that the surface of the material plays a significant role in the electrochemical properties of the material. It was found that a 1-5 nm surface phase forms within the first electrochemical cycle and may be responsible for the large irreversible capacity loss from the first cycle and the poor rate capabilities observed in these materials. Researchers have discovered that a wide variety of surface coatings improve the rate capability, the irreversible capacity loss and the impedance in the material. However, with this research, identification of the surface film's interaction with the host material is not well documented. Coatings of layered cathode materials using ionically conducting[157], ionically insulating [158], electrically conducting [159, 160], and electrically insulating [161, 162] materials have all proven to improve the electrochemical properties of layered oxide cathode materials. Therefore, an atomic level understanding of the surface mechanism for coated layered cathodes is necessary to choose a superior coating material. Our preliminary research explores AlF_3 coated $Li[Li_{0.2}Ni_{0.2}Mn_{0.6}]O_2$. Figure 8-1 confirms previous research showing improved rate capabilities for the coated cathode versus the bare electrode. Initial XPS results following 14 electrochemical cycles indicates a transformation of the pristine AlF_3 material into an $Al(OH)_3$ type structure. An initial hypothesis may suggest that the coating acts as a sacrificial coating to prevent surface deterioration caused by the electrolyte.

These initial results call for further investigation into the reasons why surface films improve the first cycle irreversible capacity loss as well as the rate capabilities. Detailed structural analysis before, during and following electrochemical cycling using advanced characterization techniques capable of probing the first 1 – 10 nm of the surface is necessary to explore the interaction of the surface film with the host material.

8.2.2 *In situ* Neutron Characterization

The *in situ* X-ray characterization from Chapter 6 and the high resolution *ex situ* X-ray characterization from Chapter 7 yielded information regarding migration of Ni and Mn in the structure; however, detailed analysis of the migration of Li and oxygen during electrochemical cycling is lacking caused by the limitations of X-ray diffraction. Neutron diffraction provides increased sensitivity to Li and oxygen as well as the ability to differentiate Ni and Mn ion site occupancy. It is therefore worthwhile to perform structural analysis using *in situ* and *ex situ* neutron diffraction during the first electrochemical cycle of the layered lithium-excess cathode materials. *In situ* neutron diffraction can also continue to explore the effects of electrochemical cycling and the relationship to microstrain forming in the material. The high resolution synchrotron data in Chapter 7 showed increased errors in the Williamson-Hall plots, which needs further analysis to identify the source that may be possible with *in situ* neutron diffraction. Figure 8-2 shows the neutron diffraction pattern collected from pristine $Li[Li_{0.2}Ni_{0.2}Mn_{0.6}]O_2$ collected at Oak Ridge National Laboratory HFIR HB-2A beamline. Rietveld refinement of the pattern confirms Li/Ni interlayer mixing. Experimental techniques similar to ones described in Chapters 6 and 7, can be applied to perform these measurements.

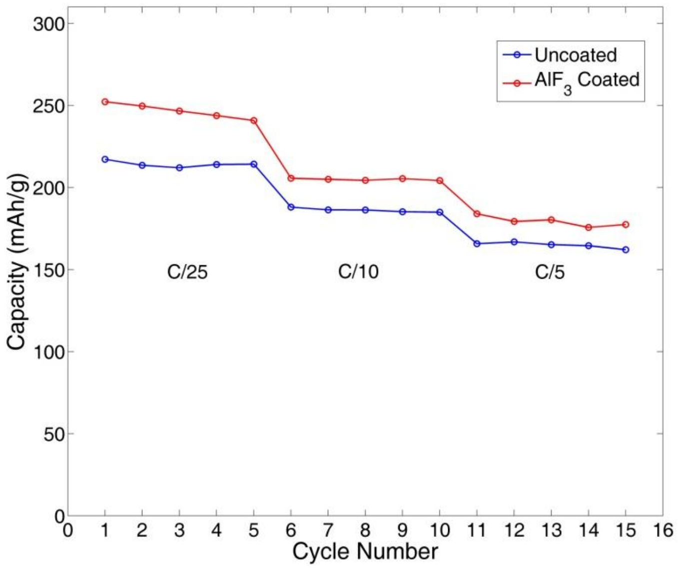

Figure 8-1. Comparison of the discharge rate capability of pristine and AlF_3 coated $Li[Ni_{1/5}Li_{1/5}Mn_{3/5}]O_2$ particles.

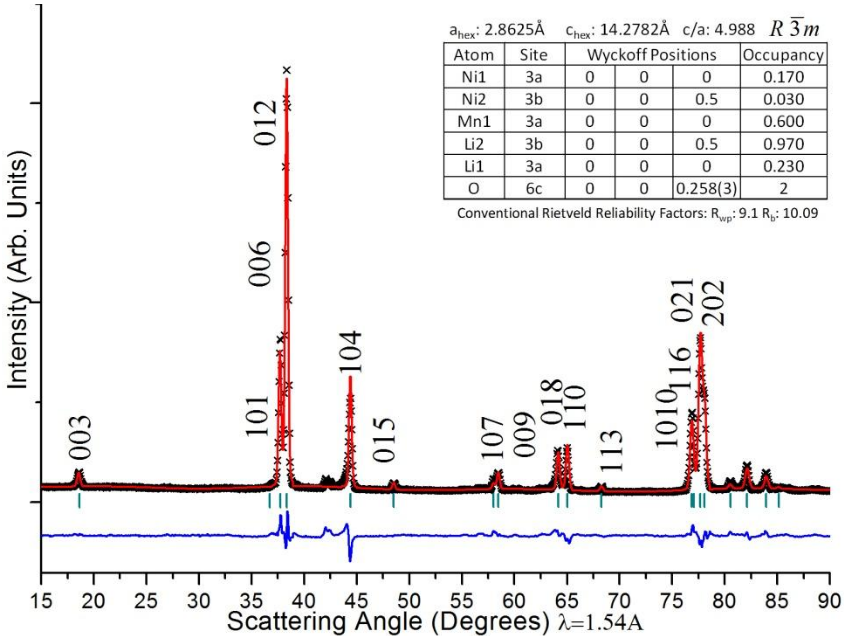

a_{hex}: 2.8625Å c_{hex}: 14.2782Å c/a: 4.988 $R\bar{3}m$

Atom	Site	Wyckoff Positions			Occupancy
Ni1	3a	0	0	0	0.170
Ni2	3b	0	0	0.5	0.030
Mn1	3a	0	0	0	0.600
Li2	3b	0	0	0.5	0.970
Li1	3a	0	0	0	0.230
O	6c	0	0	0.258(3)	2

Conventional Rietveld Reliability Factors: R_{wp}: 9.1 R_b: 10.09

Figure 8-2. Neutron diffraction pattern of pristine $Li[Ni_{1/5}Li_{1/5}Mn_{3/5}]O_2$ material.

APPENDIX
SYNTHESIS STANDARD OPERATING PROCEDURE

The pristine Li[$Ni_{1/5}Li_{1/5}Mn_{3/5}$]O_2 were synthesized by the coprecipitation processing. Stoichiometric amounts of LiOH • H_2O, $Ni(NO_3)_2$ • $6H_2O$ and $Mn(NO_3)_2$ • $4H_2O$, purchased from either Fisher or Sigma Aldrich were weighed . The amounts of each material were calculated to synthesize 4 grams of the final double hydroxide with the composition $(Ni_{1/4}Mn_{3/4})(OH)_2$. The Ni and Mn nitrate precursors were added to 50 mL of deionized H_2O in a 100 mL beaker. The LiOH precursor was added to 400mL of deionized H_2O in a 500mL curved bottom flask. Each vessel was stirred at 700rpm until all precursor solid had dissolved. The transition metal nitrates were added to the LiOH solution using a peristaltic pump. The flow rate of the transition metal solution was set at 0.4mL/minute. Figure A-1 shows the synthesis setup. The pH of the LiOH and transition metal solution was measured every 30 minutes. Following the addition of the $Ni(NO_3)_2$ • $6H_2O$ and $Mn(NO_3)_2$ •$4H_2O$ to the LiOH solution, the solution was stirred for an additional 2 hours. The resulting double hydroxide solution will be a chocolate brown in color. The solution was then funneled using a Buchner funnel. The collected precipitate was washed 3 times with deionized water and collected. The collected powder was placed into a 180°C for 10 hours. Following the evaporation of the H_2O from the material, the resulting $NiMn(OH)_2$ was weighed. Using the amount of collected sample, the moles of lithium source (LiOH•H_2O) was calculated using the following conversion:

$$\frac{x\ (Li)}{y\ (Ni+Mn)} = \frac{1.2}{0.2+0.6} = 1.5 \text{ when to synthesize Li}[Ni_{1/5}Li_{1/5}Mn_{3/5}]O_2 \qquad \text{(A-1)}$$

The dried $NiMn(OH)_2$ precipitate was ground with the LiOH lithium source using a mortar and pestle for 30 minutes until it becomes a very fine uniform powder.

Approximately 1 gram of uniformly mixed powder was added into a 15mm die press and uniaxially pressed at 20.6 MPa for 1 minute. The pellet sample was placed into a room temperature furnace. The furnace was ramped at 5°C/min up to 480°C and fired for 12 hours with furnace cooling. The powder was reground using the mortar and pestle. After the powder was reground, the powder was reformed into pellets using the same procedure and fired samples at 1000°C for 12 hours using a 5°C/min ramp rate. The samples were allowed to return to room temperature with furnace cooling.

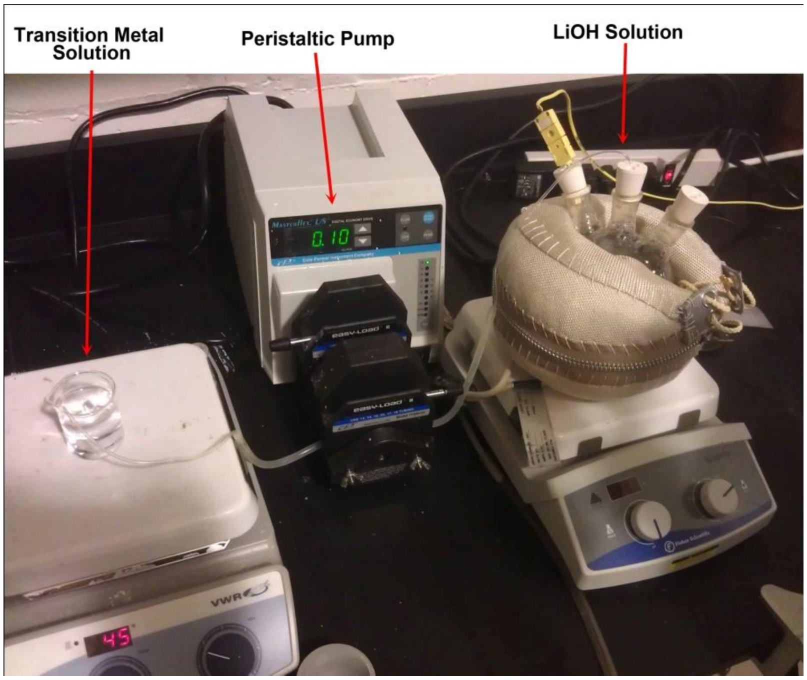

Figure A-1. Illustration of the coprecipitation setup to synthesize Li[$Ni_{1/5}Li_{1/5}Mn_{3/5}$]O_2

LIST OF REFERENCES

1. T. Nagaura and K. Tozawa, *Progresses in Batteries and Solar Cells*, 1990, **9**.

2. J.-M. Tarascon and M. Armand, *Nature*, 2001, **414**, 359.

3. V. Etacheri, R. Marom, R. Elazari, G. Salitra and D. Aurbach, *Energy & Environmental Science*, 2011, **4**, 3243-3262.

4. M. Wakihara and O. Y. (Eds.), *Li-Ion Batteries: Fundamentals and Performance*, Kodansha, Tokyo, 1998.

5. M. Armand and J. M. Tarascon, *Nature*, 2008, **451**, 652-657.

6. J. M. Tarascon and M. Armand, *Nature*, 2001, **414**, 359-367.

7. *EV Battery Test Procedures Manual: Appendix G - USABC Criteria for Advanced Battery Technologies*, 2006.

8. A. J. Bard and L. R. Faulkner, *Electrochemical Methods: Fundamentals and Applications*, John Wiley & Sons, Inc., New York, 2001.

9. A. Van der Ven and G. Ceder, *Electrochemical and Solid-State Letters*, 2000, **3**, 301-304.

10. K. S. Kang, Y. S. Meng, J. Breger, C. P. Grey and G. Ceder, *Science*, 2006, **311**, 977-980.

11. P. Strobel and B. Lambert-Andron, *Journal of Solid State Chemistry*, 1988, **75**, 90-98.

12. V. Massarotti, M. Bini, D. Capsoni, A. Altomare and A. G. G. Moliterni, *Journal of Applied Crystallography*, 1997, **30**, 123-127.

13. W. D. Kingery, Bowen, H.K. and Uhlmann, D.R., *Introduction to Ceramics*, John Wiley and Sons, New York, 1960.

14. T. Ohzuku, A. Ueda, M. Nagayama, Y. Iwakoshi and H. Komori, *Electrochimica Acta*, 1993, **38**, 1159-1167.

15. Raw Materials Xtra.

16. B. Kang and G. Ceder, *Nature*, 2009, **458**, 190-193.

17. J. Jiang, K. W. Eberman, L. J. Krause and J. R. Dahn, *Journal of the Electrochemical Society*, 2005, **152**, A1879-A1889.

18. Z. Lu, D. D. MacNeil and J. R. Dahn, *Electrochemical and Solid-State Letters*, 2001, **4**, A191-A194.

19. Z. Lu, L. Y. Beaulieu, R. A. Donaberger, C. L. Thomas and J. R. Dahn, *Journal of The Electrochemical Society*, 2002, **149**, A778-A791.

20. M. M. Thackeray, S.-H. Kang, C. S. Johnson, J. T. Vaughey, R. Benedek and S. A. Hackney, *Journal of Materials Chemistry*, 2007, **17**, 3112-3125.

21. Y. S. Meng, G. Ceder, C. P. Grey, W. S. Yoon, M. Jiang, J. Breger and Y. Shao-Horn, *Chem. Mater.*, 2005, **17**, 2386-2394.

22. W. S. Yoon, Y. Paik, X. Q. Yang, M. Balasubramanian, J. McBreen and C. P. Grey, *Electrochemical and Solid State Letters*, 2002, **5**, A263-A266.

23. J. Reed and G. Ceder, *Electrochemical and Solid-State Letters*, 2002, **5**, A145-A148.

24. H. Kobayashi, Y. Arachi, H. Kageyama and K. Tatsumi, *Journal of Materials Chemistry*, 2004, **14**, 40-42.

25. R. D. Shannon and C. T. Prewitt, *Acta Crystallographica*, 1969, **B25**, 925.

26. Z. Lu and J. R. Dahn, *Journal of the Electrochemical Society*, 2002, **149**, A815-A822.

27. J. M. Zheng, X. B. Wu and Y. Yang, *Electrochimica Acta*, 2011, **56**, 3071-3078.

28. C. S. Johnson, N. Li, C. Lefief and M. M. Thackeray, *Electrochemistry Communications*, 2007, **9**, 787-795.

29. A. D. Robertson and P. G. Bruce, *Electrochemical and Solid-State Letters*, 2004, **7**, A294-A298.

30. Y. J. Park, Y.-S. Hong, X. Wu, K. S. Ryu and S. H. Chang, *Journal of Power Sources*, 2004, **129**, 288-295.

31. Y. Wu and A. Manthiram, *Electrochemical and Solid-State Letters*, 2006, **9**, A221-A224.

32. A. R. Armstrong, M. Holzapfel, P. Novak, C. S. Johnson, S. H. Kang, M. M. Thackeray and P. G. Bruce, *J. Am. Chem. Soc.*, 2006, **128**, 8694-8698.

33. N. Yabuuchi, K. Yoshii, S.-T. Myung, I. Nakai and S. Komaba, *Journal of the American Chemical Society*, 2011, **133**, 4404-4419.

34. N. Tran, L. Croguennec, M. Menetrier, F. Weill, P. Biensan, C. Jordy and C. Delmas, *Chemistry of Materials*, 2008, **20**, 4815-4825.

35. J. M. Zheng, Z. R. Zhang, X. B. Wu, Z. X. Dong, Z. Zhu and Y. Yang, *Journal of the Electrochemical Society*, 2008, **155**, A775-A782.

36. Y. Wu, A. V. Murugan and A. Manthiram, *Journal of the Electrochemical Society*, 2008, **155**, A635-A641.

37. Y. Wu and A. Manthiram, *Solid State Ionics*, 2009, **180**, 50-56.

38. S. H. Kang and M. M. Thackeray, *Electrochemistry Communications*, 2009, **11**, 748-751.

39. T. Hahn, ed., *International Tables for Crystallography* Chester, 2006.

40. M. Winter and R. J. Brodd, 2004, vol. 104, pp. 4245-4270.

41. J. Newman and K. E. Thomas-Alyea, *Electrochemical Systems*, 2004.

42. P. Ewald, *Acta Crystallogr. Sect. A*, 1969, **25**, 103-108.

43. J. I. Langford and L. Daniel, *Reports on Progress in Physics*, 1996, **59**, 131.

44. R. J. Gummow, M. M. Thackeray, W. I. F. David and S. Hull, *Materials Research Bulletin*, 1992, **27**, 327-337.

45. G. G. Amatucci, J. M. Tarascon and L. C. Klein, *Journal of the Electrochemical Society*, 1996, **143**, 1114-1123.

46. J. Bréger, M. Jiang, N. Dupré, Y. S. Meng, Y. Shao-Horn, G. Ceder and C. P. Grey, *Journal of Solid State Chemistry*, 2005, **178**, 2575-2585.

47. H. H. Li, N. Yabuuchi, Y. S. Meng, S. Kumar, J. Breger, C. P. Grey and Y. Shao-Horn, *Chemistry of Materials*, 2007, **19**, 2551-2565.

48. M. Guilmard, C. Pouillerie, L. Croguennec and C. Delmas, *Solid State Ionics*, 2003, **160**, 39-50.

49. J. S. Kim, J. T. Vaughey, C. S. Johnson and M. M. Thackeray, *Journal of the Electrochemical Society*, 2003, **150**, A1498-A1502.

50. C. D. Wagner, W. M. Riggs, L. E. Davis, J. F. Moulder and G. E. Mullenberg, *Handbook of X-ray Photoelectron Spectroscopy*, Perkin-Elmer Corp., Eden Prarie, 1979.

51. J. F. Moulder, W. F. Stickle, P. E. Sobol and K. D. Bomben, *Handbook of X-ray Photoelectron Spectroscopy*, Perkin-Elmer Corp., Eden Prarie, 1992.

52. J. F. Watts and J. Wolstenholme, *An Introduction to Surface Analysis by XPS and AES*, Wiley & Sons Ltd., West Sussex, 2003.

53. J. C. Dupin, D. Gonbeau, H. Benqlilou-Moudden, P. Vinatier and A. Levasseur, *Thin Solid Films*, 2001, **384**, 23-32.

54. R. Dedryvère, M. Maccario, L. Croguennec, F. Le Cras, C. Delmas and D. Gonbeau, *Chemistry of Materials*, 2008, **20**, 7164-7170.

55. Q. Y. Wang, J. Liu, A. V. Murugan and A. Manthiram, *Journal of Materials Chemistry*, 2009, **19**, 4965-4972.

56. S. Verdier, L. El Ouatani, R. Dedryvere, F. Bonhomme, P. Biensan and D. Gonbeau, *Journal of the Electrochemical Society*, 2007, **154**, A1088-A1099.

57. Y.-C. Lu, A. N. Mansour, N. Yabuuchi and Y. Shao-Horn, *Chemistry of Materials*, 2009, **21**, 4408-4424.

58. Y. S. Meng, G. Ceder, C. P. Grey, W. S. Yoon and Y. Shao-Horn, *Electrochemical and Solid-State Letters*, 2004, **7**, A155-A158.

59. J. Bareño, M. Balasubramanian, S. H. Kang, J. G. Wen, C. H. Lei, S. V. Pol, I. Petrov and D. P. Abraham, *Chemistry of Materials*, 2011, null-null.

60. C. H. Lei, J. Bareno, J. G. Wen, I. Petrov, S. H. Kang and D. P. Abraham, *Journal of Power Sources*, 2008, **178**, 422-433.

61. J. Bareño, C. H. Lei, J. G. Wen, S. H. Kang, I. Petrov and D. P. Abraham, *Advanced Materials*, 2010, **22**, 1122-1127.

62. D. B. Williams and C. B. Carter, *Transmission Electron Microscopy: A Textbook for Materials Science*, Springer, 1996.

63. R. F. Egerton, *Electron Energy-Loss Spectrosopy in the Electron Microscope*, Plenum Press, New York, 1996.

64. H. Kurata and C. Colliex, *Physical Review B*, 1993, **48**, 2102-2108.

65. T. Riedl, T. Gemming and K. Wetzig, *Ultramicroscopy*, 2006, **106**, 284-291.

66. J. Graetz, C. C. Ahn, R. Yazami and B. Fultz, *The Journal of Physical Chemistry B*, 2003, **107**, 2887-2891.

67. Z. L. Wang, J. S. Yin and Y. D. Jiang, *Micron*, 2000, **31**, 571-580.

68. J. G. Wen, J. Bareño, C. H. Lei, S. H. Kang, M. Balasubramanian, I. Petrov and D. P. Abraham, *Solid State Ionics*, 2011, **182**, 98-107.

69. C. M. Wang, Z. G. Yang, S. Thevuthasan, J. Liu, D. R. Baer, D. Choi, D. H. Wang, J. G. Zhang, L. V. Saraf and Z. M. Nie, *Applied Physics Letters*, 2009, **94**, 233116-233113.

70. J. Graetz, A. Hightower, C. C. Ahn, R. Yazami, P. Rez and B. Fultz, *The Journal of Physical Chemistry B*, 2002, **106**, 1286-1289.

71. C.-M. Wang, W. Xu, J. Liu, J.-G. Zhang, L. V. Saraf, B. W. Arey, D. Choi, Z.-G. Yang, J. Xiao, S. Thevuthasan and D. R. Baer, *Nano Letters*, 2011, **11**, 1874-1880.

72. D. E. Jesson and S. J. Pennycook, *Proceedings of the Royal Society of London. Series A: Mathematical and Physical Sciences*, 1995, **449**, 273-293.

73. D. E. Jesson and S. J. Pennycook, *Proceedings: Mathematical and Physical Sciences*, 1993, **441**, 261-281.

74. S. J. Pennycook, D. E. Jesson, A. J. McGibbon and P. D. Nellist, *Journal of Electron Microscopy*, 1996, **45**, 36-43.

75. N. D. Browning, M. F. Chisholm and S. J. Pennycook, *Nature*, 1993, **366**, 143-146.

76. P. E. Batson, *Nature*, 1993, **366**, 727-728.

77. G. Duscher, N. D. Browning and S. J. Pennycook, *physica status solidi (a)*, 1998, **166**, 327-342.

78. H. Rietveld, *Journal of Applied Crystallography*, 1969, **2**, 65-71.

79. G. Caglioti, A. Paoletti and F. P. Ricci, *Nuclear Instruments and Methods*, 1958, **3**, 223.

80. P. Thompson, D. E. Cox and J. B. Hastings, *Journal of Applied Crystallography*, 1987, **20**, 79-83.

81. R. A. Young, *The Rietveld Method*, Oxford University Press, 1993.

82. L. B. McCusker, R. B. Von Dreele, D. E. Cox, D. Louer and P. Scardi, *Journal of Applied Crystallography*, 1999, **32**, 36-50.

83. G. K. Wertheim, M. A. Butler, K. W. West and D. N. E. Buchanan, *Review of Scientific Instruments*, 1974, **45**, 1369-1371.

84. P. Scherrer, *Göttinger Nachrichten Gesell*, 1918, **2**, 98.

85. A. R. Stokes and A. J. C. Wilson, *Mathematical Proceedings of the Cambridge Philosophical Society*, 1944, **40**, 197.

86. T. Ungar and A. Borbely, *Applied Physics Letters*, 1996, **69**, 3173-3175.

87. M. A. Krivoglaz and K. P. Ryboshapka, *The Physics of Metals and Metallography*, 1963, **15**.

88. I. Groma, T. Ungar and M. Wilkens, *Journal of Applied Crystallography*, 1988, **21**, 47-54.

89. C. R. Fell, K. J. Carroll, M. Chi and Y. S. Meng, *Journal of the Electrochemical Society*, 2010, **157**, A1202-A1211.

90. S. H. Kang and M. M. Thackeray, *Journal of The Electrochemical Society*, 2008, **155**, A269-A275.

91. Z. H. Lu, Z. H. Chen and J. R. Dahn, *Chemistry of Materials*, 2003, **15**, 3214-3220.

92. H. Deng, I. Belharouak, Y.-K. Sun and K. Amine, *Journal of Materials Chemistry*, 2009, **19**, 4510-4516.

93. J. Rodríguez-Carvajal, FullProf: A Program for Rietveld Refinement and Pattern Matching Analysis, Toulouse, France, 1990.

94. J. Breger, M. Jiang, N. Dupre, Y. S. Meng, Y. Shao-Horn, G. Ceder and C. P. Grey, *Journal of Solid State Chemistry*, 2005, **178**, 2575-2585.

95. M. Jiang, B. Key, Y. S. Meng and C. P. Grey, *Chemistry of Materials*, 2009, **21**, 2733-2745.

96. , National Institute of Standards and Technology, Gaithersburg, 2003, vol. Version 3.5.

97. K. Amine, H. Tukamoto, H. Yasuda and Y. Fujita, *J. Electrochem. Soc.*, 1996, **143**, 1607-1613.

98. Y. Chabre and J. Pannetier, *Progress in Solid State Chemistry*, 1995, **23**, 1-130.

99. W. Weppner and R. A. Huggins, *Journal of the Electrochemical Society*, 1977, **124**, 1569-1578.

100. H. Xia, L. Lu and G. Ceder, *Journal of Power Sources*, 2006, **159**, 1422-1427.

101. F. Zhou, X. Zhao, A. van Bommel, A. W. Rowe and J. R. Dahn, *Chemistry of Materials*, 2009, **22**, 1015-1021.

102. M. H. Lee, Y. J. Kang, S. T. Myung and Y. K. Sun, *Electrochimica Acta*, 2004, **50**, 939-948.

103. S. Jouanneau, K. W. Eberman, L. J. Krause and J. R. Dahn, *Journal of the Electrochemical Society*, 2003, **150**, A1637-A1642.

104. Y. J. Kang, J. H. Kim, S. W. Lee and Y. K. Sun, *Electrochimica Acta*, 2005, **50**, 4784-4791.

105. S. H. Kang, C. S. Johnson, J. T. Vaughey, K. Amine and M. M. Thackeray, *Journal of The Electrochemical Society*, 2006, **153**, A1186-A1192.

106. J. Reed and G. Ceder, *Electrochemical and Solid State Letters*, 2002, **5**, A145-A148.

107. W. S. Yoon, S. Iannopollo, C. P. Grey, D. Carlier, J. Gorman, J. Reed and G. Ceder, *Electrochemical and Solid State Letters*, 2004, **7**, A167-A171.

108. T. Ohzuku and Y. Makimura, *Chemistry Letters*, 2001, 744-745.

109. M. Jiang, B. Key, Y. S. Meng and C. P. Grey, *Chemistry of Materials*, 2009, **21**, 2733-2745.

110. Z. Lu and J. R. Dahn, *Journal of the Electrochemical Society*, 2002, **149**, A815-A822.

111. D. D. MacNeil, Z. Lu and J. R. Dahn, *Journal of the Electrochemical Society*, 2002, **149**, A1332-A1336.

112. A. R. Armstrong, M. Holzapfel, P. Novak, C. S. Johnson, S. H. Kang, M. M. Thackeray and P. G. Bruce, *J. Am. Chem. Soc.*, 2006, **128**, 8694-8698.

113. C. R. Fell, K. J. Carroll, M. Chi and Y. S. Meng, *Journal of the Electrochemical Society*, 2010, **157**, A1202-A1211.

114. R. A. Binns, R. J. Davis and S. J. B. Reed, *Nature*, 1969, **221**, 943-944.

115. M. E. Arroyo-de Dompablo, J. M. Gallardo-Amores and U. Amador, *Electrochemical and Solid-State Letters*, 2005, **8**, A564-A569.

116. M. E. Arroyo y de Dompablo, U. Amador, J. M. Gallardo-Amores, E. Morán, H. Ehrenberg, L. Dupont and R. Dominko, *Journal of Power Sources*, 2009, **189**, 638-642.

117. O. García-Moreno, M. Alvarez-Vega, J. García-Jaca, J. M. Gallardo-Amores, M. L. Sanjuán and U. Amador, *Chemistry of Materials*, 2001, **13**, 1570-1576.

118. M. E. Arroyo y de Dompablo, J. M. Gallardo-Amores, U. Amador and E. Morán, *Electrochemistry Communications*, 2007, **9**, 1305-1310.

119. R. Stoyanova, E. Zhecheva, R. Alcantara, J.-L. Tirado, G. Bromiley, F. Bromiley and T. B. Ballaran, *Journal of Materials Chemistry*, 2004, **14**, 366-373.

120. R. Stoyanova, E. Zhecheva, R. Alcántara, J. L. Tirado, G. Bromiley, F. Bromiley and T. Boffa Ballaran, *Solid State Ionics*, 2003, **161**, 197-204.

121. X. Wang, I. Loa, K. Kunc, K. Syassen and M. Amboage, *Physical Review B*, 2005, **72**, 224102.

122. M. Yoncheva, R. Stoyanova, E. Zhecheva, R. Alcantara, G. Ortiz and J. L. Tirado, *Journal of Solid State Chemistry*, 2007, **180**, 1816-1825.

123. G. Kresse and J. Hafner, *Physical Review B*, 1994, **49**, 14251.

124. G. Kresse and J. Furthmüller, *Computational Materials Science*, 1996, **6**, 15-50.

125. G. Kresse and J. Furthmüller, *Physical Review B*, 1996, **54**, 11169.

126. A. Van der Ven and G. Ceder, *Electrochemistry Communications*, 2004, **6**, 1045-1050.

127. B. Xu, C. R. Fell, M. Chi and Y. S. Meng, *Energy & Environmental Science*, 2011, **4**, 2223.

128. F. D. Murnaghan, *Proc. Natl. Acad. Sci. USA 30*, 1944, 244.

129. E. Rossen, C. D. W. Jones and J. R. Dahn, *Solid State Ionics*, 1992, **57**, 311-318.

130. R. Stoyanova, E. Zhecheva and L. Zarkova, *Solid State Ionics*, 1994, **73**, 233-240.

131. J. M. Gallardo-Amores, N. Biskup, U. Amador, K. Persson, G. Ceder, E. Morán and M. E. Arroyo y de Dompablo, *Chemistry of Materials*, 2007, **19**, 5262-5271.

132. D. Santamaría-Pérez, U. Amador, R. Dominko and M. E. Arroyo-de Dompablo, in preparation.

133. U. Amador, J. M. Gallardo-Amores, G. Heymann, H. Huppertz, E. Moran and M. E. Arroyo-de Dompablo, *Solid State Sciences*, 2008, **11**, 343-348.

134. M. P. Pasternak, G. K. Rozenberg, A. P. Milner, M. Amanowicz, T. Zhou, U. Schwarz, K. Syassen, R. Dean Taylor, M. Hanfland and K. Brister, *Phys. Rev. Lett.*, 1997, **79(22)**, 4409-4412.

135. A. D. Robertson and P. G. Bruce, *Chemistry of Materials*, 2003, **15**, 1984-1992.

136. B. Toby, *Journal of Applied Crystallography*, 2001, **34**, 210-213.

137. A. C. Larson and R. B. V. Dreele, *Los Alamos National Laboratory Report LAUR*, 2000, **86**.

138. G. Kresse and D. Joubert, *Phys. Rev. B*, 1999, **59**, 1758-1775.

139. G. Kresse and J. Hafner, *Phys. Rev. B*, 1994, **49**, 14251-14269.

140. J. P. Perdew, K. Burke and Y. Wang, *Physical Review B*, 1996, **54**, 16533-16539.

141. A. I. Liechtenstein, V. I. Anisimov and J. Zaanen, *Physical Review B*, 1995, **52**, R5467-R5470.

142. Y. Hinuma, Y. S. Meng, K. S. Kang and G. Ceder, *Chemistry of Materials*, 2007, **19**, 1790-1800.

143. M. D. Levi, G. Salitra, B. Markovsky, H. Teller, D. Aurbach, U. Heider and L. Heider, *Journal of the Electrochemical Society*, 1999, **146**, 1279-1289.

144. D. Aurbach, M. D. Levi, E. Levi, H. Teller, B. Markovsky, G. Salitra, U. Heider and L. Heider, *Journal of the Electrochemical Society*, 1998, **145**, 3024-3034.

145. S. J. Pennycook, *Ultramicroscopy*, 1989, **30**, 58-69.

146. E. M. James and N. D. Browning, *Ultramicroscopy*, 1999, **78**, 125-139.

147. C. P. Grey, W. S. Yoon, J. Reed and G. Ceder, *Electrochem. Solid State Lett.*, 2004, **7**, A290-A293.

148. M. N. Richard, I. Koetschau and J. R. Dahn, *Journal of The Electrochemical Society*, 1997, **144**, 554-557.

149. M. R. Palacín, F. Le Cras, L. Seguin, M. Anne, Y. Chabre, J. M. Tarascon, G. Amatucci, G. Vaughan and P. Strobel, *Journal of Solid State Chemistry*, 1999, **144**, 361-371.

150. M. Morcrette, Y. Chabre, G. Vaughan, G. Amatucci, J. B. Leriche, S. Patoux, C. Masquelier and J. M. Tarascon, *Electrochimica Acta*, 2002, **47**, 3137-3149.

151. G. K. Williamson and W. H. Hall, *Acta Metallurgica*, 1953, **1**, 22-31.

152. S. Allain, J. P. Chateau, D. Dahmoun and O. Bouaziz, *Materials Science and Engineering: A*, 2004, **387-389**, 272-276.

153. F. La Mantia, F. Rosciano, N. Tran and P. Novák, *Journal of Applied Electrochemistry*, 2008, **38**, 893-896.

154. J. M. Paulsen, C. L. Thomas and J. R. Dahn, *Journal of the Electrochemical Society*, 1999, **146**, 3560-3565.

155. A. D. Robertson, A. R. Armstrong and P. G. Bruce, *Chemistry of Materials*, 2001, **13**, 2380-2386.

156. R. W. Cahn, *Adv. Phys*, 1954, **3**, 363.

157. J. Ying, C. Wan and C. Jiang, *Journal of Power Sources*, 2001, **102**, 162-166.

158. A. Sakuda, H. Kitaura, A. Hayashi, K. Tadanaga and M. Tatsumisago, *Electrochemical and Solid-State Letters*, 2008, **11**, A1-A3.

159. H. Takahara, T. Takeuchi, M. Tabuchi, H. Kageyama, Y. Kobayashi, Y. Kurisu, S. Kondo and R. Kanno, *Journal of the Electrochemical Society*, 2004, **151**, A1539-A1544.

160. M. L. Marcinek, J. W. Wilcox, M. M. Doeff and R. M. Kostecki, *Journal of the Electrochemical Society*, 2009, **156**, A48-A51.

161. S.-T. Myung, K. Izumi, S. Komaba, Y.-K. Sun, H. Yashiro and N. Kumagai, *Chemistry of Materials*, 2005, **17**, 3695-3704.

162. S.-T. Myung, K. Izumi, S. Komaba, H. Yashiro, H. J. Bang, Y.-K. Sun and N. Kumagai, *The Journal of Physical Chemistry C*, 2007, **111**, 4061-4067.

BIOGRAPHICAL SKETCH

Christopher Ryan Fell was born in 1985 in Orlando, Florida. He attended the University of Florida obtaining his B.S. degree in materials science and engineering cum Laude in December of 2007. While studying at the University of Florida, he developed not only as a student but socially and professionally joining several honorary clubs and organizations. He met many great long lasting friends and his to-be wife during his undergraduate career. During his undergraduate studies, he worked as a research assistant under Dr. Susan Sinnott and published two peer-reviewed journal articles. This sparked his fascination with the research fields available at UF. He enjoyed the opportunities that UF presented so much that he decided to continue his education by pursuing his PhD in materials science and engineering. He joined Dr. Ying Shirley Meng's research group in January of 2008. During this time, he travelled across the United States performing advanced research experiments at national laboratories, including Oak Ridge National Laboratory and Argonne National Laboratory, which developed numerous professional connections and contributed to high quality scientific publications. In the second year of his PhD, his advisor transferred to the University of California San Diego; however, it was in his best interest to remain at the University of Florida to prevent delays to his graduation date. Meanwhile, Dr. Shirley Meng still served as the thesis advisor and continued to provide support for completing his thesis work. He joined Dr. Jacob L. Jones' research group in September 2009. Dr. Jones' unique insight into research provided numerous new avenues that led to excellent collaboration and several peer-reviewed publications.

In the final year of his PhD, Chris was awarded the 2011 Electrochemical Society's Battery Division Student Award, which is a prestigious honor given to one student yearly at the international bi-annual meeting. Chris also enjoyed the opportunity to continue his professional development through a summer internship at Johnson Controls in Milwaukee, WI. Numerous professional connections and lasting scientific collaborations were developed. He received his PhD from UF in the spring of 2012 and immediately started as a scientist at Johnson Controls in Milwaukee, WI.

Apart from his interests and fascination in science and technology, Chris enjoys spending time developing new hobbies and skills common to anybody with an engineering mindset. He often travels and explores new activities with his wife, Meredith, and his two pug dogs.

Currently, he has spent 26 years in Florida and is excited to begin the new chapter of his life in Milwaukee.